UNIVERSITÀ DEGLI STUDI DI NAPOLI
FEDERICO II

DOTTORATO DI RICERCA IN FISICA

CICLO XXXII

COORDINATORE: PROF. SALVATORE CAPOZZIELLO

Environmental effects on dynamics and topological features of quantum systems

SETTORE SCIENTIFICO DISCIPLINARE FIS/03

Candidato:
Loris Maria Cangemi

Tutor:
Prof. Vittorio Cataudella
Prof. Giulio De Filippis

Anni 2017/2020

CONTENTS

LIST OF FIGURES

PUBLICATIONS

The thesis is based on the following publications which I co-authored.

Journal Articles

- Cangemi, L. M. and Passarelli, G. and Cataudella, V. and Lucignano, P. and De Filippis, G.: **Beyond the Born-Markov approximation: Dissipative dynamics of a single qubit**. – *Phys. Rev. B*, vol. 98, issue 18, 2018,

  doi = 10.1103/PhysRevB.98.184306,

  url = https://link.aps.org/doi/10.1103/PhysRevB.98.184306.

- Cangemi, L. M. and Cataudella, V. and Sassetti, M. and De Filippis, G.: **Dissipative dynamics of a driven qubit: Interplay between nonadiabatic dynamics and noise effects from the weak to strong coupling regime**. – *Phys. Rev. B*, vol. 100, issue 1, 2019,

  doi = 10.1103/PhysRevB.100.014301,

  url = https://link.aps.org/doi/10.1103/PhysRevB.100.014301

- Cangemi, L. M. and Cataudella, V. and Sassetti, M. and De Filippis, G.: **Violations of TUR in a dissipative periodically driven quantum system beyond weak coupling regime**. – *To be submitted to Phys. Rev. B*

- Cangemi, L. M. and Mishchenko, A. S. and Nagaosa, N. and Cataudella, V. and De Filippis, G.: **Topological Quantum Transition Driven by Charge-Phonon Coupling in the Haldane Chern Insulator**. – *Phys. Rev. Lett.*, vol. 123, issue 4, 2019,

  doi = 10.1103/PhysRevLett.123.046401,

  url = https://link.aps.org/doi/10.1103/PhysRevLett.123.046401

- Cangemi, L. M. and Mishchenko, A. S. and Nagaosa, N. and Cataudella, V. and De Filippis, G.: **Topological phase transition in quantum spin Hall insulator in the presence of charge lattice coupling**. – *arXiv*, 1905.01383, cond-mat.str-el

In the course of the Ph.D. years, I have also taken part to the following publications, which have not been included in the thesis work

- A. de Candia and G. De Filippis and L. M. Cangemi and A. S. Mishchenko and N. Nagaosa and V. Cataudella: **Two-channel model for optical conductivity of high-mobility organic crystals**. – *EPL (Europhysics Letters)*, vol. 125, number 4, 2019,

  doi= 10.1209/0295-5075/125/47002,

  https://doi.org/10.1209

- G. De Filippis and A. de Candia and L. M. Cangemi and M. Sassetti and R. Fazio and V. Cataudella: **Quantum Phase Transitions in the Spin-Boson model: MonteCarlo Method vs Variational Approach a la Feynman**. – *arXiv*, 1912.13448, cond-mat.str-el

INTRODUCTION

The control of dynamical evolution of engineered quantum system is one of the main goals of modern science and technology. The related far-reaching technological applications span from the realization of reliable quantum computing devices, to quantum criptography, metrology and sensing. This field is rapidly evolving, as several tech companies claimed to have succeded in achieving the quantum supremacy, i. e. the experimental demonstration of a computing device that, exploiting the properties of quantum mechanics, could outperform classical computers in solving computational tasks belonging to a given complexity class [1]. Besides offering promising technological applications, in the last three decades the realization of artificial interacting quantum systems has been prompted by fundamental open problems in physics. Following Richard Feynman's seminal paper [2], who first advanced the idea of simulating the properties of complex quantum systems by employing a quantum computer, in the last two decades the field of quantum simulation has seen impressive advances [3]. Different experimental platforms are now available, which have been designed to simulate ground state properties [4], dynamical phase transitions [5], and thermalization [6] of complex many body quantum systems; strongly-correlated quantum systems are special cases of study, because they impose severe limits to classical computer simulations. Topological properties of quantum systems, as well, can also be mimicked by quantum simulators [7, 8], and in principle entirely artificial system Hamiltonians could be simulated by exploiting the properties of these experimental platforms.

In this context, the study of open quantum systems, i. e. the dynamical properties of quantum systems in contact with external environment, has regained momentum, motivated by the need for accurate control of the decoherence effects on systems performing quantum operations. Except for fault-tolerant topological quantum computing devices, whose experimental realization is yet to come [9], quantum gates acting on systems of qubits are unavoidably affected by environmental decoherence, which acts as a source of errors on any quantum operation [10]. Decoherence also severely hinders the entanglement between different qubits, so that it negatively affects the performance of nearly all quantum information devices [11]. These detrimental effects can be limited and taken under control only by employing sophisticated engineering techniques.

Open quantum systems can be conceived as a very special instance of quantum many-body systems, where typically one or few quantum degrees of freedom are in contact with an ensemble of many other

different degrees of freedom, i. e. the environment, which typically can be described by a continuous distribution of energy levels. Although many different models of environment have been devised [12–14], several common features affecting the quantum state of the reduced system can be considered, e. g. decoherence effects, relaxation occurring during dynamics and dissipation. Thanks to its generality, this description finds applications in actual experiments, from solid-state qubits to optical lattices. In the past three decades open quantum systems have also provided an ideal testbed for purely foundational problems in quantum mechanics, e. g. the emergence of classicality the interaction of the quantum system with its environment, quantum to classical transition and quantum Darwinism [15, 16].

The control of artificial quantum degrees of freedom can be achieved by coupling them to external electromagnetic (E.M.) driving fields. Modeling driven quantum systems in the presence of external environment, e. g. thermal or structured baths, is thus of paramount importance to quantum devices. A striking example is given by Adiabatic Quantum Computing (AQC), a field which has attracted great interest during the last two decades as a feasible way to realize Quantum Computation (QC), alternative to standard circuit model [17]. Furthermore, D-Wave quantum machines based on Quantum Annealing (QA) protocols are already available on the market [18]. AQC protocols have been devised to solve optimization problems belonging to NP complexity class [17]: these problems are known to be equivalent to finding the ground state of an interacting, frustrated quantum many body Hamiltonian, i. e. usually called the target Hamiltonian. The main idea thus relies on QA, i. e. on the realization of the adiabatic evolution of a system of qubits described by a time-dependent Hamiltonian that, at the end of the evolution, is equal to the target Hamiltonian. These adiabatic protocols have also been known to be less prone to the environmental decoherence than their circuit models counterparts [19, 20], but a complete understanding of decoherence effects in these devices is still an open problem [21].

Driven quantum systems in the presence of one or more heat baths are at basis of prototypical models of quantum heat engines, i. e. microscopic machines performing heat-to-work conversion while operating in the quantum realm [22–25]. Beyond their potential technological impact, these ideal machines are fundamental in the understanding of the implications of quantum mechanics on heat and work exchange, i. e. thermodynamics at the microscopic level. The so-called field of Quantum Thermodynamics [26], recently linked to quantum information theory [27], encompasses several long-standing open problems.

The basic conceptual framework of open quantum systems finds applications in several problems in condensed matter physics, where a microscopic description of dissipation effects is required[28]. Fermionic

systems interacting with lattice quantum degrees of freedom, i. e.phonons, belong to this class. Various models of electron-phonon (E-PH) interactions, developed sixty years ago, account for the influence of the microscopic environment on the dynamics of charge carriers and give a description of dissipation effects. As an example, Frölich polaron theory describes the charge transport in low dimensional systems in terms of polaronic quasiparticles, i. e. electrons surrounded by the cloud of lattice distortions [29]. E-PH correlations are responsible for a wide range of interesting effects occurring in solids, from conventional superconductivity to instabilities of the Fermi sea in 1-D chains, the latter corresponding to the emergence of ordered ground states of matter, i. e. charge-density waves (CDW) [30]. It has been proven that strong E-PH interactions are among the main mechanisms involved in the formation of many competing ground state phases of high temperature superconductors, like copper-oxides [31]. Nowadays high T_c superconductivity remains a puzzling state of matter, where competing ordered states arising from strong correlation effects manifest themselves, giving rise to an incredibly rich phase diagram. The major paradigm employed to describe these properties is based on Quantum Phase Transitions [32], i. e. phase transitions characterized by quantum fluctuations of the ground-state properties occurring at $T = 0$, in the vicinity of a phase diagram point where nonthermal parameters assume critical values [33]. However, many phenomena in modern condensed matter theory cannot be properly described in the context of conventional QPT.

Topological insulators are short-range entangled topological phases of matter [34], i. e. they cannot be described by means of a conventional Ginzburg-Landau theory [35]. These phases of matter are characterized by insulating properties in the bulk, while on the edges symmetry-protected gapless electronic conduction modes can be measured [36, 37]. The physics of these materials is found to be suitably modeled by means of topological band invariants [38, 39], i. e. integers which describe the global, geometric properties of single-particle band structure. The bulk-boundary correspondence [36] links the values of topological invariants to the number of edge modes flowing at the boundary of these materials. Different topological phases are thus distinguished by the values of these invariants, i. e. the Hamiltonians describing insulators in different topological phases cannot be connected to each other by adiabatic deformation. As a result, the topological phase diagram of these special insulators consists of different regions separated by curves of zero gap. Owing to their short-range entanglement character, these systems are well-described by single-particle band theories.

Quite recently, several efforts have been spent to shed light on the effects of electronic correlations in topological insulators [40]. To avoid confusions, electron-electron correlations can bring about a variety of physical effects, and a clear understanding of the physical scenario

when topological features are involved is yet to come. However, several lines of research have been established in the last decades. The physics of correlated topological insulators has been the subject of great interest in order to test the robustness of topological insulating phases in the presence of interactions. Prototypical models, like Kane-Mele-Hubbard have been put forward [41]. Another set of theoretical proposals have been focused on the possible existence of interaction-induced topological phases. Typical examples belonging to the latter group are topological phases arising by long-range Coulomb interactions [42] and fluctuation-induced topological insulators. However, in an even more exotic context, correlated topological phases without noninteracting analogoues have been proposed, where topological order can play a role. Among them, topological Mott insulators and fractional topological insulators [42, 43]. However, as the interplay between Coulomb interactions and topological insulating phases has been widely discussed, much less attention has been devoted to E-PH interactions effects on prototypical topological insulating phases. The possibility for E-PH interactions to stabilize or destroy existing topological insulating phases and the occurrence of interaction-induced topological phases thus deserves more attention.

This work reports the results of our theoretical study on different quantum systems coupled to external environments. Our analysis extends to very different systems, ranging from dissipative qubits to E-PH correlated topological fermionic systems. We focus on interesting physical regimes where consolidated weak-coupling approximations schemes may fail to give a reliable theoretical description of these systems.

The work is divided in two parts.

The first part of the work deals with the study of dynamics of dissipative two-level systems (TLS) driven by external classical time-dependent control fields. They work as archetypal models of a single qubit in contact with a quantum thermal bath. As we shall see, these models have been widely employed in the theoretical description of superconducting Josephson tunnelling circuits in the low temperature regime, where various sources of quantum noise act to degrade the device perfomances. The actual realizations of the driving field include, but are not limited to, microwave pulses through coplanar waveguides [44]. Although these models are conceptually simple, analytical solutions are available only in special points of the parameter space, after mapping procedures valid under limiting conditions. As a consequence, in order to obtain a reliable description of dynamics in the non-Markovian setting and beyond the weak-coupling approximation, numerical methods have to be employed which can simulate the physics in a sufficiently wide range of parameters.

Chpt. 1 is devoted to a brief introduction to the physics of several prototypical models of quantum dissipative systems which will be

simulated below. We also quickly summarize traditional theoretical approaches employed over the last decades to solve these problems.

In Chpt. 2, we propose a numerical approach based on Short Iterative Lanczos method (SIL) to simulate the dynamics of the dissipative TLS, both in the absence of a fixed bias field and in the presence of a time-dependent linear field. In the latter case, both the bias field and the tunnelling element are driven with fixed rate t_f^{-1}. Similar driving schedules have been extensively used in theoretical simulations of Adiabatic Quantum Computing devices (AQC)[20], where the effects of dissipation are described by means of Markovian quantum master equations (QME). While typical devices comprise many interacting qubits, with nonomogeneous coupling strengths and a driven tunnelling element, here we focus on the effects of the environment on a single qubit. We show that our method can successfully decribe non-Markovian quantum dynamics arising from the coupling with the bath, thus giving a reliable description of the physics against approximated QME predictions. In addition, we compare the results of our simulations with well-known analytical predictions on the dissipative TLS, discussing the main differences and drawing conclusions.

In Chpt. 3, we extend the study carried out in Chpt. 2 of a dissipative TLS, going from intermediate to strong coupling regime; the dynamics in the unbiased case, as well as in the presence of a simple non-linear driving protocol are considered. Quite recently, the time-dependent protocol has been experimentally realized employing superconducting circuits driven by microwave pulses, in order to simulate topological phases of matter. We show that, in the time-independent unbiased case, we are able to simulate the crossover to a completely incoherent tunnelling regime due to the strong qubit-bath correlations, which can be analytically predicted for fixed value of the coupling strength $\alpha = 0.50$ and in the scaling limit. In the driven case, we show that an interplay between nonadiabatic dynamics due to the driving field and dissipation may arise for rapid sweeps, which has not been accurately described in previous works, where Stochastic Schrödinger equation (SSE) has been employed [45].

In Chpt. 4, we study the dynamics of a periodically driven TLS in contact with a thermal bath, where two driving fields of different amplitudes, for fixed frequency and phase difference, modulate the levels asymmetry. This system can be employed as a microscopic model of driven isothermal engine [46], acting as a work to work converter. Similar systems have been studied in the literature as simple instances of microscopic heat engines, i. e. devices performing heat to work conversion while operating at the microscopic scale. These machines have been mainly conceived to test thermodynamic bounds on efficiency at finite power, in order to understand whether they could achieve better performance than macroscopic devices, i. e. finite-time cyclic heat engines operating at Carnot efficiency.

We study the effects of quantum coherence and system-bath quantum correlations on efficiency, output power and power fluctuations of our work-to-work converter, restricting to linear irreversible thermodynamics setting. We show that a recently derived tradeoff relation, the so-called Thermodynamic Uncertainty Relation (TUR), valid for periodically-driven classical Markovian engines, can be violated in the quantum regime, i. e. a work to work converter in the quantum regime may achieve a better performance than its classical analogue, for different ranges of the driving frequency. We also discuss feasible generalizations of our work in the context of non-linear response theory.

In the second part of the thesis, we study topological properties of fermionic systems in contact with a microscopic environment made of lattice quantum vibrations. Our aim is study the stability of topological phases of matter in the presence of strong E-PH correlations, characterizing the possible occurrence of topological quantum phase transitions and the strongly correlated phases which take over as the system turns into a trivial insulator.

Chpt. 5 is aimed at giving general information on the models of noninteracting topological systems we intend to study. In particular, the physics of Chern insulators and Time-Reversal (TR) symmetry-protected topological insulators will be briefly covered.

In Chpt. 6, we study the properties of the first prototype of topological insulator, i. e. the Haldane model of a Chern insulator on a honeycomb lattice, in the presence of lattice vibrations. As a consequence of lattice motion, the electrons modify their energies by interacting with the underlying lattice degrees of freedom. We model the E-PH by means of the Holstein model [47], i. e. electrons couple locally with the lattice displacements, which occours through a phonon mode of fixed frequency. We restrict our description to the case of e-hole symmetry; by employing cluster perturbation theory (CPT) [48], we show that in the limit where the lattice vibrational energy is greater than the hopping parameters, i. e. in the anti-adiabatic limit, the E-PH interaction drives the topological quantum transition of the fermionic system from a topological state to a trivial one. Furthermore, in the particular case of zero mass term, our approach signals the onset of CDW order.

In Chpt. 7, we employ the same approach as in Chpt. 6, to explore the effects of E-PH interactions on a paradigmatic model of topological insulators, i. e. the quantum spin Hall effect (QSH). These system exhibit a $\mathbb{Z}_2$ symmetry-protected topological state, which can be described by means of an integer, known as $\mathbb{Z}_2$ invariant. For simplicity, we consider a QSH system in the absence of Rashba coupling term. The traditional way to obtain this system is to take two different copies of the Haldane model on different honeycomb lattices. We show that the increase of E-PH coupling strength causes the system to leave the

Part I

DISSIPATIVE SYSTEMS

1 MODELS OF DISSIPATIVE SYSTEMS

Quantum systems interacting with their environment exhibit decoherence and dissipation. The pursuit of accurate theoretical description of dissipation in the quantum realm dates back to 1960s, while from the mid-1980s to 1990s several pioneering works have been written, encompassing both analytical and numerical approaches [12, 49–53]. However, in the last two decades, the field has regained popularity, following the impressive advances in the field of quantum technologies. One of the primary goals in this field is the control of devices made of one up to hundreds of quantum degrees of freedom performing unitary evolution to execute a computational task. The building blocks of these devices are superconducting quantum circuits coupled to each other and to microwave photons [54], as well as cold atoms in optical lattices [55, 56]. Depending on the specific experimental platform, the environment can consist of different sources of quantum noise and decoherence, e. g. in solid-state based Cooper Pair Boxes (CPB) qubits renowned noise sources are background charge fluctuators [11].

In Chapters 2,3,4, we will focus on minimal yet nontrivial models of dissipative quantum systems. These models consist of a single quantum degree of freedom, i. e. a two-level system (TLS), linearly coupled to a thermal bath at fixed temperature, which acts as a reservoir. The thermal bath is modeled by a set of quantum harmonic oscillators, with frequencies obeying a fixed spectral distribution. Models of these kind are popularly known as Spin-Boson Models (SBM) and can be employed to describe a wide class of quantum systems, ranging from cold atom impurities in optical lattices [57], to superconducting qubits subject to time-dependent E.M. fields [44] and quantum heat engines [23]. In the following sections, we introduce the general form of the models we intend to study, discussing the main features which can be found in the literature.

1.1 FROM CALDEIRA–LEGGETT MODEL TO SPIN–BOSON MODEL

The Caldeira-Leggett model [12, 28] is the standard theoretical description of dissipation effects on single quantum systems. It describes the evolution of a quantum degree of freedom, e. g. q subject to a

potential $V(q)$, in contact with an ensemble of quantum harmonic oscillators. The Hamiltonian of this model reads

$$H = \frac{p^2}{2m} + V(q) + \sum_{k=1}^{N} \frac{p_k^2}{2m_k} + \sum_{k=1}^{N} \frac{1}{2} m_k \omega_k^2 \left(x_k - \frac{c_k}{m_k \omega_k^2} F(q) \right)^2, \quad (1.1)$$

where m_k, ω_k are respectively the masses and frequencies of the oscillators, while $F(q)$ is a generic function describing the coupling. We intend to restrict to the linear coupling case, i. e. $F(q) = q$, the quantum degree of freedom is linearly coupled to each mode of the bath. From Eq. (1.1), the equations of motion for the variable q and the oscillators can be derived. A classical Langevin equation for q can be written

$$m\ddot{q}(t) + m \int_0^t dt' \gamma(t - t') \dot{q}(t') + V'(q) = \xi(t). \quad (1.2)$$

Here the influence of the bath on the dynamics of the quantum degree of freedom can be described in terms of friction, measured by a damping coefficient $\gamma(t)$, and a stochastic force $\xi(t)$ exerted by the bath oscillators giving rise to fluctuations. Notice that Eq. (1.2) exhibits memory effects, described by the nonlocal in time character of the kernel. In this context, the damping coefficient $\gamma(t)$ is a function of time, which in the case of Eq. (1.1) reads

$$\gamma(t) = \theta(t) \frac{1}{m} \sum_k \frac{c_k^2}{m_k \omega_k^2} \cos(\omega_k t). \quad (1.3)$$

We can usefully introduce the spectral density function of the bath $J(\omega)$ as follows

$$J(\omega) = \frac{\pi}{2} \sum_k \frac{c_k^2}{m_k \omega_k} \delta(\omega - \omega_k). \quad (1.4)$$

This function describes the properties of the thermal bath. Actually, it can be shown by taking the continuous limit of $J(\omega)$, i. e. assuming an infinite number of bath frequencies modes, belonging to a continuous set; then, taking the Fourier transform of Eq. (1.3), it is easily shown that it can be written as follows

$$\gamma(\omega) = \lim_{\varepsilon \to 0} \frac{-2i\omega}{\pi m} \int_0^\infty d\omega' \frac{J(\omega')}{\omega'} \frac{1}{\omega'^2 - \omega^2 - i\omega\varepsilon}. \quad (1.5)$$

The spectral function $J(\omega)$ is thus proportional to the real part of $\gamma(\omega)$, i. e. $J(\omega) = m\omega \, \mathrm{Re}\{\gamma(\omega)\}$. Thus, $J(\omega)$ describes the nature of dissipation. It is conventional to assume a phenomenological model for $J(\omega)$ which takes into account the Ohmic dissipation and the possible deviations from it. Furthermore, it is sensible to assume a frequency cutoff on $J(\omega)$, i. e. in the limit of infinite frequency the spectral distribution must vanish. Though several choices may be

taken for $J(\omega)$ (see Chapters 2 and 3), we will mostly adopt the usual exponential cutoff form

$$J(\omega) = \eta \omega_c^{1-s} \omega^s \exp(-\omega/\omega_c), \tag{1.6}$$

where ω_c is a the cutoff frequency, η has the dimensions of a viscosity, and the parameter s distinguishes among three different kinds of dissipation that have been studied in the recent literature [28, 49, 58]: Ohmic ($s = 1$), sub-Ohmic ($s < 1$) and super-Ohmic case ($s > 1$). Eq. (1.1) can be employed to model a wide range of physical problems, differing from one another with respect to the single quantum degree of freedom involved.

The quantum dynamics in a double-well effective potential $V(q)$, as depicted in Fig.1.1, is of great relevance [28]. Here the quantum

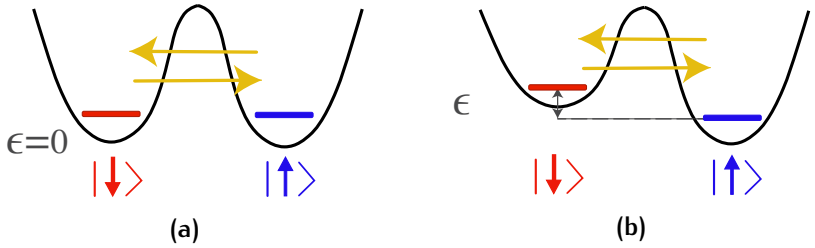

Figure 1.1: Sketch of the double-well system: in a the unbiased, symmetric case; in b a finite bias ε is present.

degree of freedom can tunnel through the potential barrier, with a given tunneling energy splitting $\hbar\Delta$. The height of the barrier, as well as the asymmetry of the two wells mimima $\hbar\varepsilon$, can be controlled by the experiment. The energy difference between the ground state of the well and the first excited state is $\hbar\omega_g$. If the barrier height is greater than $\hbar\omega_g$, and in turn $\omega_g > \varepsilon, \Delta, k_B T/\hbar$, the Hilbert space of the system can be restricted to two-dimensions, i. e. a TLS where the two states coincide with low-lying energy eigenstates of the two wells. Thus, the particle position operator and the tunneling can be conveniently written in terms of pseudospin 1/2 operators $\{\sigma_i\}$. Choosing as a set of basis states the eigenstates of σ_z operator, i. e. $\sigma_z |\hat{z};\pm\rangle = \pm |\hat{z};\pm\rangle$, the position operator can be written as $q = (q_0/2)\sigma_z$, so that the basis states are also position eigenstates, i. e. localised in each of the two wells. From now on, we set $\hbar = 1$. The Hamiltonian of the TLS describing the tunneling between the two minima of the well is thus

$$H_S = -\frac{\varepsilon}{2}\sigma_z - \frac{\Delta}{2}\sigma_x. \tag{1.7}$$

In order to describe the quantum nature of the bath, the formalism of bosonic creation (annihilation) operators $b_k^\dagger (b_k)$ can be adopted, with commutation relations $\left[b_k, b_l^\dagger\right] = \delta_{kl}$. The Hamiltonian of the free bath H_B can thus be written as follows

$$H_B = \sum_k \omega_k b_k^\dagger b_k. \tag{1.8}$$

Within this framework, the fluctuating force acting on the system can be modeled as a dipole-field interaction, where the single quantum degree of freedom couples linearly to the bath coordinates, in a similar fashion to Eq. (1.1). The interaction Hamiltonian H_{SB} can thus be written as

$$H_{SB} = \frac{1}{2}\sigma_z \sum_k \lambda_k (b_k^\dagger + b_k). \tag{1.9}$$

The coupling elements λ_k are proportional to those of Eq. (1.1), i. e. $\lambda_k = q_0 c_k$. The spectral density of the bath changes accordingly and can be written as

$$J(\omega) = \sum_k \lambda_k^2 \delta(\omega - \omega_k) = 2\alpha \frac{\omega^s}{\omega_c^{s-1}} e^{-\frac{\omega}{\omega_c}}, \tag{1.10}$$

where the adimensional parameter α is a measure of the strength of the dissipation. Collecting the terms in eqs. (1.7) to (1.9) we obtain the SBM Hamiltonian

$$H_{SBM} = -\frac{\varepsilon}{2}\sigma_z - \frac{\Delta}{2}\sigma_x + \sum_k \omega_k b_k^\dagger b_k + \frac{1}{2}\sigma_z \sum_k \lambda_k (b_k^\dagger + b_k). \tag{1.11}$$

Eq. (1.11) is the simplest, minimal model describing decoherence and dissipation effects on a TLS. Dynamical and thermodynamical properties of Hamiltonians of the form in Eq. (1.11) have been extensively studied, due to their connection to Macroscopic Quantum Tunneling (MQT) experiments [49].

The solid state experimental platforms where SBM has found many applications are superconducting Josephson tunneling junctions. The actual quantum degrees of freedom experiencing tunneling depend on the considered device. The two archetypal devices (see Fig. 1.2) are Cooper Pair Box (CPB), i. e. the first example of charge qubit, and flux qubits. In the simplest CPB, at sufficiently low temperatures (of the order of mK) a superconducting island is connected to a superconducting reservoir by means of a Josephson junction. The island is contacted with a biasing gate in series with a capacitor. The charge in the island is measured with respect to a reference value. Superconducting Cooper pairs experience tunneling from the reservoir to the island across the Josephson junction. If the device works in the charge configuration, the two different quantum states of the TLS can be represented by the states of charge in the island, i. e. $|n\rangle, |n+1\rangle$ which are those with n and $n+1$ Cooper pairs respectively. CPB was historically the first device where superposition of charge states $|n\rangle, |n+1\rangle$ was observed [59, 60]. On the other hand, flux qubits consist of a superconducting ring interrupted by one to three Josephson tunneling junctions. The magnetic flux through the superconducting ring tunnels between two different states, encoded by the clockwise and anticlockwise circulating supercurrents respectively [60]. Due to the macroscopic nature of these devices, in the last twenty years they have been found to be prone to decoherence. For instance, in

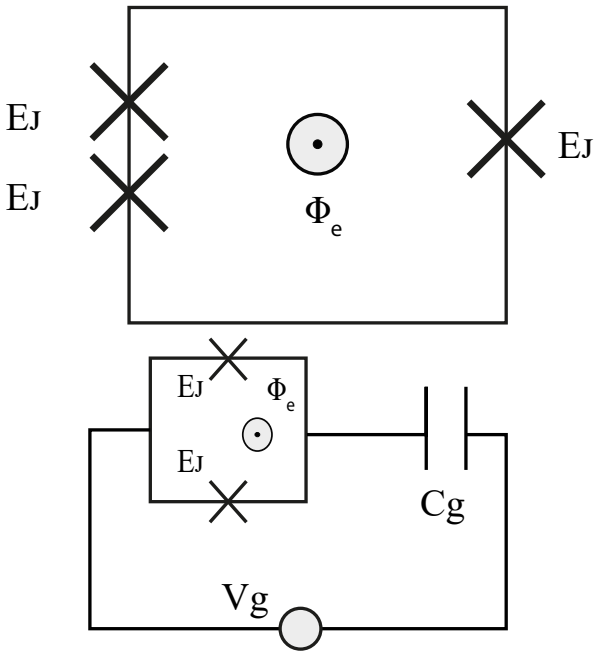

Figure 1.2: Schematic circuit diagrams of superconducting Josephson qubits. Equivalent circuit scheme for flux and charge qubits respectively; E_J is the Josephson coupling energy, E_C is the electrostatic Coulomb energy. Adapted from [54].

the case of charge qubits, $1/f$ noise arising from background charge fluctuators [61, 62] and voltage fluctuations, have been studied as possible sources of decoherence. However, these devices have now been replaced by Transmon and Xmon qubits architectures, allowing much longer coherence times ($T_1 \simeq 140\mu s$) with respect to the early devices [63]. In modern experimental and computing platforms made of hundreds of qubits the problem of decoherence and dissipation can be reduced yet not completely eliminated [64].

1.2 PHASE DIAGRAM OF SBM

The minimal model in Eq. (1.11), despite its conceptual simplicity, has a fairly rich phase diagram, which we report in Fig. 1.3. The physical properties of the SBM phase diagram depend on the nature of dissipation, i.e. on the parameter s. Ohmic dissipation ($s = 1$) represents a rather special case. In the absence of bias ($\varepsilon = 0$), at fixed temperature $T = 0$, a critical value of the adimensional coupling strength α_c exists for which the system exhibit a Quantum Phase Transition (QPT) [32, 33] from delocalized to localized phase, arising from the ground state quantum fluctuations. Namely, at $\alpha = \alpha_c = 1$ the tunneling element Δ is renormalized to zero, and the spin gets trapped in one of the two wells, depending on the initial conditions. The equilibrium magnetization $\langle \sigma_z \rangle$ at $T = 0$ shows a quick drop

exactly at the critical point, while $\langle \sigma_x \rangle$ is a monotonic decreasing function of α. For finite bias $\varepsilon \neq 0$, a crossover from delocalized to localized phase has been predicted by the use of analytical approaches [65]. The nature of this phase transition has been understood by mapping the Eq. (1.11) in the anisotropic Kondo model [66], which describes the exchange interactions of a a single magnetic impurity immersed in a fermionic bath. In the following, we briefly report the main steps, while the details of the calculation can be found in [49, 67]. The anisotropic Kondo Hamiltonian reads

$$H_{\mathrm{K}} = \sum_{k,\sigma} \varepsilon(k) c^{\dagger}_{\boldsymbol{k},\sigma} c_{\boldsymbol{k},\sigma} + J_{\parallel} S_z s_z(0) + J_{\perp}(S_x s_x(0) + S_y s_y(0)) \tag{1.12}$$

where S, s describe the spin of the impurity and the band fermions respectively. The low-temperature excitations of the fermionic bath in Eq. (1.12) around the Fermi energy can be described by means of bosonic degrees of freedom. Employing standard bosonization

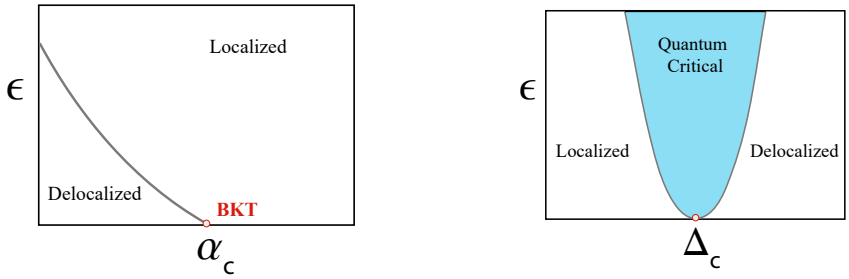

(a) Ohmic phase diagram

(b) Sub-Ohmic phase diagram

Figure 1.3: Sketch of the phase diagram of SBM at $T = 0$, adapted from [65]: in panel a, the phase diagram in the Ohmic case is plotted, which exhibit a QPT of BKT kind at $\varepsilon = 0$ and $\alpha_c = 1$, signaling the transition from delocalized to localized phase. At finite bias ε the transition is replaced by a crossover between the two phases. In panel b, the sub-Ohmic case is plotted.

techniques [49, 65, 67, 68], a set of bosonic operators (a_k, b_k) can be employed to describe charge and spin excitations around the Fermi surface as follows

$$b_k = \left(\frac{\pi}{kL}\right)^{\frac{1}{2}} \rho(-k), \; a_k = \left(\frac{\pi}{kL}\right)^{\frac{1}{2}} \sigma(-k) \tag{1.13}$$

where $\rho(k) = \sum_{p,\sigma} c^{\dagger}_{p+k,\sigma} c_{p,\sigma}$ and $\sigma(k) = \sum_{p,\sigma} \sigma c^{\dagger}_{p+k,\sigma} c_{p,\sigma}$ are respectively the charge and spin density operators. Assuming linear dispersion of the Fermionic band around Fermi energy, i. e.$\varepsilon(k) = \varepsilon_{\mathrm{F}} + v_{\mathrm{F}}(|k| - k_{\mathrm{F}})$, where v_{F} is the Fermi velocity, it can be easily shown that the free fermionic contribution in Eq. (1.12) can be written in terms of two separate bosonic fields, i. e. $H_0^B = v_{\mathrm{F}} \sum_{k>0} k(a^{\dagger}_k a_k + b^{\dagger}_k b_k)$, due to charge and spin excitations respectively. While the longitudinal interaction term can be easily rewritten in terms of a linear combination of

$a_k^\dagger(a_k)$, the transverse coupling terms are proportional to products of fermionic operators of the kind $c_\uparrow^\dagger c_\downarrow (c_\downarrow^\dagger c_\uparrow)$. Following a non-rigorous bosonization approach [69], new bosonic fields can be introduced

$$j_\sigma(x) = \sum_{k>0} \exp(-ak/2) \left(\frac{2\pi}{kL}\right)^{1/2} \left(\tilde{b}_{k,\sigma} \exp(i\sigma kx) - \tilde{b}_{k,\sigma}^\dagger \exp(-i\sigma kx)\right), \tag{1.14}$$

where $\tilde{b}_{k,\sigma} = (b_k + \sigma a_k)/\sqrt{2}$ and a cutoff on the electronic momenta has been introduced, so that $a = k_F^{-1}$. In addition, new operators defined by means of the exponential of operators in Eq. (1.14) can be introduced, i. e. $\psi_\sigma(x) = (2\pi a)^{-1/2} \exp\{j_\sigma(x)\}$. It can be easily shown that, evaluating products of the previous operators on the ground state of the bosonic noninteracting system, e. g. $\langle \psi_\sigma^\dagger(x)\psi_\sigma(y))\rangle$, they behave as real fermionic operators when evaluated on the noninteracting Fermi sea. Though not rigorous, this procedure allows to write a bosonized version of Eq. (1.12), with decoupled bosonic fields, which reads

$$H_K^B = v_F \sum_{k>0} k a_k^\dagger a_k + \frac{J_\parallel}{4}\sigma_z \sum_{k>0} \left(\frac{k}{\pi L}\right)^{1/2} \exp(-ak/2)(a_k^\dagger + a_k) + \\ + \frac{J_\perp}{4\pi a}(\sigma_+ \exp(\xi) + \sigma_- \exp(-\xi)) \tag{1.15}$$

where $\xi = \sum_{k>0} \exp(-ak/2)(4\pi/kL)^{1/2}(a_k - a_k^\dagger)$. This form allows, after a straightforward canonical transformation, to rewrite the Hamiltonian in Eq. (1.15) in terms of an unbiased SBM Hamiltonian.

By rewriting Eq. (1.15) in terms of the adimensional coupling strength ρJ, where $\rho = (2\pi v_F)^{-1}$, it can be shown that Eq. (1.15) is thus equivalent to an unbiased SBM where:

$$\frac{\Delta}{\omega_c} = \rho J_\perp, \alpha = \left(1 - \frac{1}{2}\rho J_\parallel\right)^2 \tag{1.16}$$

From Eq. (1.16), it can be seen that the coupling strength $\alpha_c = 1$ separates the two phases of the Kondo problem, i. e. the antiferromagnetic coupling phase ($\rho J_\parallel > 0$) from the ferromagnetic case ($\rho J_\parallel < 0$). In turn, in a famous Anderson's paper [70], the phase transition in the Kondo model has been analytically mapped into that of a long-ranged classical Ising model. The transition occurring in the latter system has been later recognized to be due to topological defects by Kosterlitz and Thouless [71], so that it is known as Berezinskii-Kosterlitz-Thouless (BKT) transition. In order to better understand the correspondence between the critical behavior of the Ohmic SBM and that of the long-ranged Ising model, the problem has been studied by employing quantum to classical mapping: here the quantum SBM model can be mapped in a $d+1$-dimensional classical system evolving in the imaginary time τ and described by the action

$$S_{cl} = \int_0^\beta d\tau \int_0^\beta d\tau' \sigma_z(\tau') K(\tau - \tau') \sigma_z(\tau), \tag{1.17}$$

where $K(\tau) \propto 1/\tau^{1+s}$. Then, for $s = 1$, the critical properties of SBM are found to be described by a classical long-range ($\propto \tau^{-2}$) Ising model in the imaginary time, which shows BKT phase transition. However, in the last twenty years, the BKT nature of the transition in the ohmic SBM has been confirmed with NRG calculations [65, 72], and more recently, by means of variational approaches [73], while the sub-Ohmic regime has been investigated using Numerical Renormalization Group (NRG) and Quantum Monte Carlo (QMC) techniques [58, 74].

In the delocalized phase, where tunneling is present, starting from the mapping procedure it can be shown that the tunneling element Δ gets increasingly renormalized as follows

$$\Delta_r = \Delta(\Delta/\omega_c)^{\alpha/(1-\alpha)} \tag{1.18}$$

With increasing α, it becomes increasingly small, and in the limit $\omega_c \to \infty$ it tends to zero at the transition. This behavior has several consequences on the dynamics of the TLS, as we will show in the subsequent sections.

1.3 DYNAMICS

The dynamics of SBM has been investigated by the use of different theoretical approaches. Despite all the efforts, a reliable analytical description of the bath influence on the TLS dynamics has not been found. The dynamics of the model in Eq. (1.11) can be studied following the general approach of open quantum systems [28, 75]. As with any bipartite system, the Hilbert space of the TLS and the bath can be written as

$$\mathcal{H} = \mathcal{H}_S \otimes \mathcal{H}_B \tag{1.19}$$

where $\mathcal{H}_S$ and $\mathcal{H}_B$ indicate the Hilbert space of the TLS and the bath respectively. The Hamiltonian in Eq. (1.11) acting in the total Hilbert space can be written as customary

$$H = H_S + H_B + H_{SB}. \tag{1.20}$$

The density matrix of the whole system $\rho(t)$ evolves obeying to Von Neumann equation of motion with Hamiltonian H

$$\frac{d}{dt}\rho(t) = -i[H, \rho]. \tag{1.21}$$

From the total density matrix, the state evolution of any subsytem belonging to the bipartition can be computed tracing over the degrees of freedom of the other subsystem. The reduced density matrix of the TLS can thus be written as

$$\rho_S(t) = \mathrm{tr}_B\, \rho(t), \tag{1.22}$$

where the partial trace is taken over the bath degrees of freedom. The evolution of the reduced density matrix in Eq. (1.22) allows us to compute the expectation values of the observables of the TLS. Several approximate analytical treatments have been devised in order to compute the behavior of correlators as functions of time, namely the magnetization along the $\hat{z}$ axis $\langle\sigma_z(t)\rangle$, or the two-time correlation functions $\langle\sigma_z(t)\sigma_z(t')\rangle$ which are directly related to experiments.

In the unbiased case ($\varepsilon = 0$), with Ohmic dissipation ($s = 1$), theoretical approaches based on Conformal Field Theory (CFT) [65] predict that $\langle\sigma_z(t)\rangle$ exhibits underdamped oscillations in time, for fixed values of the coupling strength $0 \leq \alpha < 1/2$, which is a signature of coherence loss. However, the detailed expressions of the oscillation frequency and the damping rate depend on the approximation scheme adopted [76].

In the following, we will briefly introduce the main consolidated approaches to study dynamics of SBM, which will serve as starting points for the original contributions reported in the subsequent chapters.

1.3.1 Quantum Master Equations

Quantum master equations (QME) approach to open systems aims at describing the dynamics of the reduced density matrix in Eq.(1.22) by means of a first-order differential equation. This problem has been formulated by means of projection theory, a well-known approach in nonequilibrium classical statistical mechanics [77]. The main idea is interpret the trace over the bath as the result of the application of a given projection operator, acting on the space of density matrices of the total system. Thus, for the projected, i. e. the relevant part, a formally exact integro-differential equation of motion can be derived, which in principle describes all non-Markovian, i. e. time-retardation effects arising from the system-bath interaction. While the influence of non-Markovianity in quantum mechanics is still a challenging open problem [78], the most common description of open quantum systems oriented towards a broad range of applications [79, 80], relies on Markovian Master Equations (MME). MME equations are linked to the definition of dynamical maps [81]. At initial time t_0, the state of the system is assumed to be factorized,

$$\rho(t_0) = \rho_S(t_0) \otimes \rho_B. \tag{1.23}$$

A dynamical map [78] is a linear operator which maps physical states at time t_0 into physical states at any time t

$$\rho_S(t) = \Phi(t, t_0)\rho_S(t_0) = \mathrm{tr}_B\, U(t, t_0)\rho_S(t_0) \otimes \rho_B U^\dagger(t, t_0). \tag{1.24}$$

It preserves Hermiticity, the trace of operators, and is also a Completely Positive (CP) map. The requirement of complete positivity is crucial for many application in quantum information science [82].

However, considering a two-parameter family of maps $\Phi(t_1, t_2) = \Phi(t_1, t_0)\Phi^{-1}(t_2, t_0)$, $t_1 > t_2 > t_0$, if the inverse exists for each of the positive maps, the maps is said to be divisible. There is no assurance that $\Phi(t_1, t_2)$ is also CP. The subset of CP maps that are also divisible is the relevant subset of maps for MME [78]. It is clear that, if there exists an operator $\mathcal{L}$ such that:

$$\Phi(t) = \exp(\mathcal{L}t) \tag{1.25}$$

the map is CP divisible. In this case, the map belongs to a one-parameter group called dynamical semigroup, the superoperator $\mathcal{L}$ being the generator of the semigroup, and the reduced density matrix evolution obeys to the following equation

$$\frac{d}{dt}\rho_S(t) = \mathcal{L}\rho_S(t). \tag{1.26}$$

In this special case, it can be proven that $\mathcal{L}$ assumes the Lindblad form [83], and the Eq. (1.26) reads

$$\frac{d}{dt}\rho_S(t) = -i[H, \rho_S(t)] + \mathcal{D}(\rho_S(t)) \tag{1.27}$$

where we have introduced the dissipator $\mathcal{D}$, which is a superoperator acting on the reduced density matrix that reads

$$\mathcal{D}(\rho_S) = \sum_k \gamma_k \left(A_k \rho_S A_k^\dagger - \frac{1}{2}\left\{ A_k^\dagger A_k, \rho_S \right\} \right). \tag{1.28}$$

It can be expressed in terms of fixed Lindblad operators A_k, one for each mode of the bath, acting in the reduced Hilbert space $\mathcal{H}_S$, which are linked to the orthonormal basis of operators chosen to characterize the map[75].

Eq. (1.27) is the MME in the Lindblad form. In Eq. (1.27), the first contribution describes the unitary part of dynamics, while the dissipator accounts for the effects of irreversibility, namely decoherence, dissipation, and entropy production. The parameters γ_k are nonnegative and describe relaxation rates : it is actually a necessary condition for achieving CP [84]. The dynamical semigroup structure requires that H_S, as well as the Lindblad operators A_k and the γ_k are time-independent. However, the notion of CP divisibility allows to generalize Eq. (1.27) to the case where the generator depends on time. It is found that a time dependent MME in the Lindblad form is CP positive if and only if the time dependent rates are nonnegative, i. e. $\gamma_i(t) \geq 0$. On the other hand, the conditions for which CP holds for the general time-dependent Lindblad equation is still an open problem [78].

The MME in the Lindblad form in Eq. (1.27) can be derived from the unitary dynamics of the total system in Eq. (1.21) only if a given set of approximations is adopted, also known as Born-Markov approximations. In the first place, a general form for the interaction Hamiltonian

is assumed, i. e. $H_{SB} = \sum_k A_k \otimes B_k$, where A_k, B_k are operators of the system and the bath respectively. In the case of Eq. (1.11), it is clear that $A_k = \sigma_z$, $B_k = \lambda_k(a_k^\dagger + a_k)$. By rewriting Eq. (1.21) in the interaction representation and tracing over the bath degrees of freedom, all the contribution of order higher than two with respect to the interaction Hamiltonian are disregarded. Further, the density matrix of the total system is forced to be a product state, i. e. $\rho(t) \simeq \rho_S(t) \otimes \rho_B$ at every time t, hence the system-bath correlations are disregarded. This approximation can hold only in the limit of weak coupling between system and bath. Furthermore, the Markov approximation disregards all the memory effects in the dynamics, and the important assumption is done that the bath correlations decay on times which are much smaller than the relaxation time of the reduced system. Eventually, an additional rotating wave approximation, which disregards the non-secular terms of dynamics, assures that the MME is of Lindblad form. The actual expression of the final equation is quite different from Eq. (1.27), as it describes also the renormalization of the bare model energies due to Lamb-type contribution. In the Schrödinger picture [75], it reads

$$\frac{d}{dt}\rho_S(t) = -i[Hs + H_{LS}, \rho_S(t)] + \mathcal{D}(\rho_S(t)) \tag{1.29}$$

where the Lamb-shift Hamiltonian and the dissipator can be rewritten in terms of the Lindblad operators as follows

$$\mathcal{D}(\rho_S(t)) = \sum_\omega \sum_{k,k'} \gamma_{k,k'} \left(A_{k'}(\omega)\rho_S A_k^\dagger(\omega) - \frac{1}{2}\left\{ A_k^\dagger(\omega)A_{k'}(\omega), \rho_S \right\} \right) \tag{1.30}$$

$$H_{LS} = \sum_\omega \sum_{k,k'} S_{k,k'}(\omega) A_k^\dagger(\omega) A_{k'}(\omega) \tag{1.31}$$

Here the operators $A(\omega)$ are known as eigenoperators of H_S; both the decay rates $\gamma_{k,k'}(\omega)$ and the Lamb-Shift $S_{k,k'}(\omega)$ depend on the equilibrium correlation function of the bath, and can be written as

$$\gamma_{k,k'}(\omega) = \int_{-\infty}^{+\infty} \exp(i\omega\tau) \langle B_k(\tau) B_{k'}(0) \rangle \tag{1.32}$$

$$S_{k,k'}(\omega) = \int_{-\infty}^{+\infty} \frac{d\omega'}{2\pi} \gamma_{k,k'}(\omega) P\left(\frac{1}{\omega - \omega'} \right) \tag{1.33}$$

In the case of SBM Hamiltonian in Eq. (1.11), as a consequence of the time-independent nature of the TLS Hamiltonian, Eq. (1.29) has a simple closed-form analytical solution, reported in App. a, which we will further discuss in the subsequent chapters.

1.3.2 Influence functional method

In the previous subsection, a time-local QME for the reduced density matrix of the TLS has been introduced. It can be easily expected

that, for increasing system-bath coupling strength, the Markovian QME in Eq. (1.29) fails to describe the correct physical behavior of the reduced density matrix in Eq. (1.22). The main reason is that the state of the system + bath cannot be described with such a simple factorized product form as in Eq. (1.23), i. e. system-bath quantum correlations become relevant. Moreover, in the low temperature regime, the assumptions of Markovianity are questionable, as memory effects due to the quantum fluctuations have to be considered.

The formally exact expression for the reduced density matrix can be written by employing real-time path integral formalism [49, 85]. A given element of the reduced density matrix is the probability for the TLS to go from a fixed initial point x_i to a final point x_f in the space of real-time trajectories. For a general system-bath linear interaction, indicating the paths of the system and the bath with $(x(t), X(t))$ respectively, the reduced density matrix reads

$$\rho(x_\mathrm{f}, t) = \int \mathcal{D}x(\tau)\mathcal{D}y(\tau') \exp i(S[x(\tau)] - S[y(\tau')])\mathcal{F}[x(\tau), y(\tau')], \tag{1.34}$$

where the sum is over all the TLS paths $x(\tau')(y(\tau'))$ connecting the initial and final points $x_\mathrm{i}, x_\mathrm{f}$, i. e. $x(t_\mathrm{o}) = y(t_\mathrm{o}) = x_\mathrm{i}$, $x(t) = y(t) = x_\mathrm{f}$ and $\mathcal{F}$ is a functional of the TLS coordinates only that can be computed by summing over all paths $X(t), Y(t)$ as follows

$$\begin{aligned}\mathcal{F}[x(\tau), y(\tau')] = \sum_{X(t_\mathrm{f})} \int \mathcal{D}X(\tau'')\mathcal{D}Y(\tau''') \exp i\big(S_\mathrm{o}[X(\tau'')] - S_\mathrm{o}[Y(\tau''')] \\ + S_\mathrm{int}[x(\tau), X(\tau'')] - S_\mathrm{int}[y(\tau'), Y(\tau''')]\big).\end{aligned} \tag{1.35}$$

Here the sum is over all the possible final times configurations of the bath, and $S_\mathrm{o}, S_\mathrm{int}$ are the free and the interaction contribution to the total action S of the system, respectively. Notice that, by adopting this formalism, both the populations and the coherences of the TLS density matrix can be treated on equal footing. The functional $\mathcal{F}$, the so-called influence functional, includes all the effects arising from system-bath interactions without any limitation. Furthermore, due to the easy structure of the interaction Hamiltonian in Eq. (1.1), the sums over paths $X(t), Y(t)$ of the bath can be straightforwardly worked out, and the final result can be written in the form [49]

$$\begin{aligned}\mathcal{F}[x(\tau), y(\tau')] = \exp \frac{1}{\pi} \int_{t_0}^{t} d\tilde{\tau} \int_{t_0}^{t} d\tilde{s}(iL_1(\tilde{\tau} - \tilde{s})[x(\tilde{\tau}) - y(\tilde{\tau})] \\ \cdot [x(\tilde{s}) + y(\tilde{s})] - L_2(\tilde{\tau} - \tilde{s})[x(\tilde{\tau}) - y(\tilde{\tau})][x(\tilde{s}) - y(\tilde{s})]),\end{aligned} \tag{1.36}$$

where

$$\begin{aligned}L_1(t) &= \int_0^\infty d\omega J(\omega) \sin \omega t \\ L_2(t) &= \int_0^\infty d\omega J(\omega) \coth(\beta\omega/2) \cos \omega t.\end{aligned} \tag{1.37}$$

By direct examination of Eq. 1.34 and 1.35, it is evident that the bath correlation functions cannot be factorized as in Sec. 1.3.1, and the effects of bath on the density matrix are non-local in time. It is also clear that the influence functional can account for decoherence of the TLS dynamics, as the contributions to the functional coming from paths which resides in the off-diagonal states, i. e. $x(\tau) - y(\tau) \neq 0$ contribute to reduce the coherence. The double paths in Eq. (1.35) can be seen as a single real-time path through the 4 possible configurations : $\{+,+\},\{+,-\},\{-,+\},\{--\}$, where direct transitions between couples of mutual diagonal and off-diagonal states are forbidden. These paths can be discretized by the values of symmetric and antisymmetric coordinates [28], i. e. $\xi(s) = (1/q_0)(x(s) - y(s))$, $\chi(s) = (1/q_0)(x(s) + y(s))$. As Eq. (1.35) depends on the free action of the TLS, the paths giving nonzero contributions are only those that visit states linked by spin flips. These considerations are sufficient to parametrize the path integral in Eq. (1.34) in terms of "blips" and "sojourns" variables at each time t. Except for values of the coupling strength $\alpha = 1/2 - r$, $r \to 0$, the resulting expression for the elements of the reduced density matrices is analytically intractable, due to terms involving interblip correlations at different times and sojourn-blips correlations [49]. Several analytical approximations have thus been devised, which hold only in limited ranges of parameters values [86].

One of the most popular approximation is the non-Interacting Blip Approximation (NIBA) [49, 87]: this approach is based on neglecting all the inter-blip correlations at any time t, and restricting the range of blip-sojourns correlations as explained in [28]. The main idea is that, during its dynamics, the system spend, on average, much more time in the diagonal states than in the off-diagonal ones. Limiting the analysis to the Ohmic case, it is found to be true only in the absence of bias, in the weak coupling regime or in the case of strong damping or high temperature. According to NIBA scheme, for $0 < \alpha < 1/2$ and $T = 0$ the magnetization $\langle \sigma_z(t) \rangle$ show underdamped oscillations in time and can be described in terms of analytic functions of the rescaled time $\Delta_{\text{eff}} t$, with the effective tunneling energy Δ_{eff} reading

$$\Delta_{\text{eff}} = [\Gamma(1-2\alpha)\cos\pi\alpha]^{\frac{1}{2(1-\alpha)}} \Delta_{\text{r}} \ , \ \Delta_{\text{r}} = \Delta \left(\frac{\Delta}{\omega_{\text{c}}}\right)^{\frac{\alpha}{1-\alpha}} . \tag{1.38}$$

Here Δ_{r} is the renormalized gap as in Eq. (1.18). The form of the solution is given as a Mittag-Leffler function [88]

$$\langle \sigma_z(t) \rangle = \sum_{m=0}^{+\infty} \frac{(-1)^m}{\Gamma[1-2(1-\alpha)]} (\Delta_{\text{eff}} t)^{2(1-\alpha)m}. \tag{1.39}$$

While the resulting expression for the oscillation frequency is expected not to be valid [89], this analytical treatment provides the correct result for the quality factor of the damped oscillation, i. e.

$$Q = \frac{\Omega}{\gamma} = \cot\left(\frac{\pi\alpha}{2(1-\alpha)}\right), \tag{1.40}$$

(see Chap. 2.2 for details), which is a monotonic decreasing function of α.

Further, for $\alpha = 1/2$ Eq. (1.39) reduces to an exponentially decresing function of time, i. e. $\langle \sigma_z \rangle = \exp\left(-\pi\Delta^2/2\omega_c\right)$. It is knwon as Toulouse limit. Here a crossover from coherent to incoherent dynamics takes place: at zero bias, the oscillation frequency tends to vanish, as well as the quality factor Q, and the tunneling is totally incoherent.

Although the NIBA approach successfully describes the main features of the system in the unbiased case, in the presence of an external bias field ε, it fails in describing the long-time limit of $\langle \sigma_z(t) \rangle$ (see 2.2). However, several exact analytical treatments based on perturbation theory are known which, in the weak coupling limit, give the correct results for the qubit observables, taking into account the fully-quantum correlations with the bath degrees of freedom (see Chap.3.2.2). These theories have been recently employed to derive analytical results for the dynamics of heat exchange between the qubit and the reservoir [90].

The Toulouse point $\alpha = 1/2$ is special, as here the path integral expression for $\langle \sigma_z \rangle (t)$ can be summed analitically. If $\langle \sigma_z(0) \rangle = 1$, in the limit of small Δ/ω_c, i. e. $\omega_c \to \infty$ (scaling limit) the magnetization dynamics takes the form

$$\langle \sigma_z(t) \rangle = e^{-\gamma t} + 2\int_0^t d\tau \frac{\sin(\varepsilon\tau)}{\beta \sinh\left(\frac{\pi\tau}{\beta}\right)} \left(e^{-\gamma\frac{\tau}{2}} - e^{-\gamma t} e^{\gamma\frac{\tau}{2}}\right) \tag{1.41}$$

where $\beta = 1/T$ ($k_B = 1$) and the damping rate is proportional to the renormalized gap at $\alpha = 1/2$, i. e. $\gamma = \pi\Delta^2/2\omega_c$. In the absence of external bias, $\langle \sigma_z(t) \rangle$ takes the exponential form which is also recovered in the NIBA approximation.

Interestingly, the analytical solution in Eq. (1.41) can be found by mapping the SBM into a Resonant Level Model (RLM), describing a single localized impurity in contact with a bath of spinless fermions at the Fermi level; in addition, Coulomb interactions between the impurity and the fermionic bath are present [49, 65, 91], and the resulting coupling strength is a function of α. For $\alpha = 1/2$, Coulomb interactions vanish and the model can be exactly solved: by preparing the qubit in the state $|\hat{z}; +\rangle$, it is possible to derive Eq.1.41.

1.4 DISSIPATIVE DRIVEN SYSTEMS

Models of driven quantum system contacted with thermal bath are of great importance in many technological applications, ranging from semiconducting devices to superconducting quantum circuits [44]. In particular, driven quantum tunneling has been extensively studied in the past three decades [87].

Prototypical models are quantum degrees of freedom subject to time-dependent potentials and contacted with one or more thermal baths. Driven SBM are among the most studied models thanks to their wide range of applications reported in 1.1. In the following, we will focus on the dynamics of driven dissipative TLS, where in place of the TLS Hamiltonians in Eq. (1.7) we take

$$H_S(t) = -\frac{\Delta(t)}{2}\sigma_x - \frac{\varepsilon(t)}{2}\sigma_z, \tag{1.42}$$

Here both the tunneling element and the bias field of the TLS are externally driven in time, following different schedules. In actual experiments, the simplest device is a superconducting flux qubit, and the driving is obtained by means of E. M. fields, like microwave pulses sent via circuit waveguides [44]. Depending on the form of the driving fields, different nonequilibrium dynamical effects have to be expected. Below, we introduce two main theoretical models known as famous instances of driven TLS, namely the dissipative Landau-Majorana-Stückelberg-Zener (LMSZ) model and the periodically driven TLS model.

1.4.1 Dissipative LMSZ model

Dissipative LMSZ model describes a TLS system subject to a linearly driven magnetic field, experiencing tunneling between the two levels. The LMSZ Hamiltonian is

$$H_{\text{LMSZ}} = \frac{\Delta}{2}\sigma_x + \frac{vt}{2}\sigma_z + H_B + H_{SB}, \tag{1.43}$$

where v is the velocity of the LMSZ sweep, H_B is the Hamiltonian of the free bath as in Eq. (1.8), and the system-bath Hamiltonian assumes a more general form with respect to Eq. (1.9)

$$H_{\text{SB}} = \frac{1}{2}\sum_k \lambda_k(\cos\theta_k\sigma_z + \sin\theta_k\sigma_x)(b_k^\dagger + b_k). \tag{1.44}$$

In the absence of dissipation, the LMSZ Hamiltonian describes the dynamics of a TLS during a sweep with fixed velocity v through an avoided level crossing, as depicted in Fig. 1.4. In this condition, the dynamics starts at time $t \to -\infty$, when the TLS is assumed to be in the ground state, i. e. $|\uparrow\rangle$. As it is driven at later times t through the avoided level crossing, i. e. the time of minimum gap, transitions from the instantaneous ground state to the excited eigenstate can occur. As a consequence, there is a finite probability, i. e. $P_{\uparrow\to\uparrow}(t)$, of finding the TLS in the excited diabatic state. It clearly depends on time, on the tunneling element and on the sweep velocity v. In its asymptotic form, it reads [92]

$$P_{\uparrow\to\uparrow}(t\to\infty) = \exp\left(-\frac{\pi\Delta^2}{2v}\right). \tag{1.45}$$

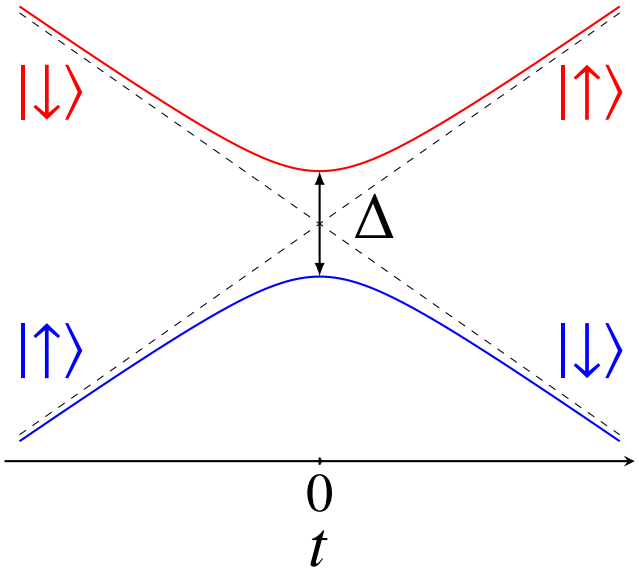

Figure 1.4: Scheme of the LMSZ avoided level crossing. In solid blue (red) lines the instantaneous energy eigenstates of the non interacting LSMZ Hamiltonian. Diabatic states at $t \to \pm\infty$ are also depicted.

Eq. (1.46) is popularly known as LMSZ formula. Several works [93–96] have studied the possible modifications of the excitation probability in Eq.(1.46) occurring when the TLS interacts with a thermal bath. Indeed, an exact result holds at $T = 0$, which is based on direct computation of time-ordered expansion of the survival probability of the state $|\uparrow\rangle$, i. e. $P_{\uparrow\to\uparrow}(t \to \infty) = \langle\uparrow, \mathbf{0}| U(-\infty, \infty) |\uparrow, \mathbf{0}\rangle$ [96]. Here the Hamiltonian in Eq.(1.43) can be written as $H(t) = H_0(t) + H_I$, the first containing H_B and all the operators proportional to σ_z, while the remaining one H_I, which is proportional to σ_x, is considered as a perturbation. The operator $H_0(t)$ can be diagonalized exactly after the application of a polaronic transformation. $|\uparrow, \mathbf{0}\rangle$ is thus the ground state of the shifted-oscillators Hamiltonian, while the time-evolution operator is computed in the interaction representation starting from $H_I(t)$. The following result holds for the modified LMSZ formula

$$P_{\uparrow\to\uparrow}(t \to \infty) = \exp\left(-\frac{\pi \mathcal{W}^2}{2v}\right), \tag{1.46}$$

where a new parameter $\mathcal{W}$ appears in place of the bare tunneling element, which can be written in a closed form as follows

$$\mathcal{W}^2 = \left(\Delta - \sum_{k=1}^{M} \lambda_k^2 \frac{\sin\theta_k \cos\theta_k}{\omega_k}\right)^2 + \sum_{k=1}^{M} \lambda_k^2 \sin^2\theta_k. \tag{1.47}$$

Several features of this results are interesting: the asymptotic excitation probability retains the same form as Eq. 1.46. Furthermore, by

fixing all the angles $\theta_k = 0$, i. e. in the longitudinal coupling case, the parameter $\mathcal{W}$ is equal to the bare tunneling element Δ, so that the excitation probability is left unchanged. On the other hand, adding a transverse coupling component to the bath can alter the excitation probability, by inducing spin flips during the course of the sweep. This result is independent on the nature of the dissipation, i. e. the bath spectral distribution in Eq. (1.4). It has different implications in the field of AQC, where the paradigm of LMSZ sweeps has been frequently employed in order to give a description of the annealing procedure, involving systems of interacting qubits [18, 97, 98]. In this context, the annealing procedure is designed to find solution to a computational NP-hard problem by means of adiabatic quantum evolution of a system of coupled qubits. The target Hamiltonian, i. e. the system Hamiltonian at final time encodes the solution to the problem in its ground state [17]. As claimed in several works on AQC [19, 20, 98, 99], the effects of dissipation are not necessarily detrimental to the success of the annealing procedure. However, the beneficial influence of the external bath at finite temperature T has not been yet completely understood [21], and possible explanations addressing the nature of the qubit-bath coupling have been recently proposed [100].

1.4.2 Periodically driven dissipative systems

Periodically driven TLS in the presence of dissipation belongs to an interesting class of driven quantum systems. Referring to our TLS in Eq. (1.42), here the bias field $\varepsilon(t)$ is periodically modulated in time. Beside its established widespread applications in driven tunneling systems [87], periodic modulation has been recently proven to be of fundamental importance for achieving high-fidelity control of engineered qubits in the presence of noise [101, 102]. The periodic nature of the TLS Hamiltonian, i. e.

$$H(t) = H(t + \mathcal{T}), \tag{1.48}$$

has several consequences on the nature of the eigenstates. By using Floquet theory, it can be proven that the solutions of Schrödinger equations have peculiar properties

$$|\psi(t)\rangle = \exp(-i\varepsilon_j t)\,|\phi_j(t)\rangle\,,\ |\phi_j(t+\mathcal{T})\rangle = |\phi_j(t)\rangle\,, \tag{1.49}$$

where $|\phi_j(t)\rangle$ are known as Floquet modes, and the real-valued ε_j are the quasi-energies of the system. Floquet modes form a complete set of states in the Hilbert space. Another fundamental property linked to Eq.(1.48) is that the evolution operator $U(t_0 + n\mathcal{T}, t_0)$ can be written as

$$U(t_0 + n\mathcal{T}, t_0) = [U(t_0 + \mathcal{T}, t_0)]^n\,. \tag{1.50}$$

It follows that the knowledge of the evolution operator in a single period $\mathcal{T}$ is sufficient to compute the time evolution operator at any

later time $t_0 + n\mathcal{T}$. For the very special case of TLS subject to harmonic drive in the absence of dissipation, these properties can be proven to bring about interesting phenomena, entirely due to the periodic nature of the drive. Perhaps a strikingly important example, in the case of single monochromatic driving field, is the existence of relations between the fields amplitude and frequency bringing to Coherent Destruction of Tunneling (CDT) [103]. However, in the case of periodically driven dissipative TLS, approximate analytical treatments have been developed, properly working only in limited ranges of model parameters. Widespread analytical methods are Floquet Born-Markov approaches [87] and Floquet expansions [104, 105] i. e. consisting of QME written in the basis of Floquet states, which can also include non Markovian effects. Numerical approaches have also received considerable attention in the last decades: the Quasi Adiabatic Path Integral Method (QUAPI) [52, 106], which is based on iterative calculation of the influence functional is a consolidated tool; more recent, non perturbative approaches include Stochastic Schrödinger Equation methods [76], and Tensor Product States related techinques [107]. However, despite all the efforts, only few, numerical methods have been developed which can give access to a reliable physical description of quantum systems in the presence of strong coupling with the bath and without significative restrictions on the driving field strengths and frequencies. On the other hand, the regime of strong system-bath coupling has seen a growing interest in the last years, prompted by the need to understand the implication of quantum mechanics on thermodynamics of microscopic heat engines, entropy production, energy conversion. In the following chapters, we propose a study of models of driven TLS in the presence of dissipation, adopting an entirely numerical approach which differs from those proposed in the literature. We focus on dynamics of these systems, which can be relevant in the field of control of noisy qubits (Chpt. 2, 3) and in the simulation of simple instances of microscopic work-to-work converters 4, which in turn offer an ideal testbed to probe thermodynamics relations.

2 DISSIPATIVE DYNAMICS BEYOND BORN-MARKOV APPROXIMATION.

In this chapter, we present part of our results based on original contributions published in [108].

In the last years, there has been a growing effort to describe decoherence effects in adiabatic quantum computation (AQC) and quantum annealing (QA) protocols [109, 110]. This field regained momentum since the first experimental demonstration of the D-Wave machine [18], and the subsequent launch on the market of the first devices.

As anticipated in Sec. 1.3.1, QME are a consolidated tool for studying the dynamics of open quantum systems. They have been extensively used in the modeling of AQC and QA protocols [19, 111, 112]. The Lindblad equation relies on several assumptions on the system dynamics: in particular, on the Born approximation (disregarding qubit-bath correlations at any times during the dynamics provided that their coupling energy is weak enough) and on the Markov approximation (which ensures that the dissipation mechanism involves no memory effects). Moreover, its extensions to time-dependent dynamics depend on the considered protocol. In the field of AQC, adiabatic QME [79] have been frequently employed, which are strictly valid when the rotating wave approximation (RWA) holds.

Recent works [97–100, 109, 110] show that AQC of a qubit ensemble with intermediate coupling to its bath may have shorter annealing time than a closed system. This speed-up is predicted at very low temperatures and intermediate couplings to the environment: a regime where non-Markovian effects and multiple-excitation processes may be relevant [113–116].

In this work, we discuss an alternative technique to account for decoherence and dissipation in open quantum systems, which could in principle overcome the limitations of the Lindblad equation, allowing us to avoid the set of Born-Markov approximations. This approach combines: a discretization of the bath in Eq. (1.9) and (1.10) [117], which is described in terms of a finite number of independent harmonic oscillators; a smart truncation scheme of the bosonic Hilbert space; short-iterative Lanczos (SIL) method [118–121]. Our technique is not affected by the limitations of standard perturbative approaches, as it guarantees the trace preservation and positivity of the density operator. Due to its stability and reduced computational effort, this method allows us to include multiple-excitation processes, not accounted by the Lindblad theory [122, 123]. Moreover, as we do not

trace over the bath degrees of freedom, we have access to the full wave function, and we can compute all the properties of either the reduced system and the bath. By means of our technique, we will focus on two different models describing the dynamics of a TLS interacting with its environment. These models obey to the general form described in Sec. 1.1 and 1.4.

This chapter is organized as follows: in Sec. 2.1, we discuss the main features of our numerical method; in Sections 2.2 and 2.3, we introduce the particular TLS Hamiltonians to be studied and present our results, comparing them with known approximations schemes. Eventually, we discuss further possible extensions of this work in Sec. 2.4.

2.1 SHORT-ITERATIVE LANCZOS METHOD

Here we present our numerical approach devised to simulate the dynamics of models ruled by Hamiltonian operators $H(t)$ as in Eq. Eq. (1.20). Although in the following sections $H_S(t)$ will be restricted to the case of a single TLS as in Eq. (1.42), the method can find application to the case of single as well as multiple interacting degrees of freedom. The bath degrees of freedom are of the form in Eq. (1.8), while the system-bath interaction can in principle assume the general form in Eq.(1.44). For the sake of simplicity, at the initial time t_0, we assume the density matrix of the qubit and bath to be factorized:

$$\rho(t_0) = \rho_S(t_0) \otimes \rho_B, \tag{2.1}$$

where $\rho_S(t_0)$ is the density operator of the reduced system at the initial time and ρ_B is the bath density operator at thermodynamic equilibrium at temperature $T = 1/\beta$ ($k_B = 1$ here and in the following). Given the time evolution operator

$$U(t, t_0) = \hat{\mathcal{T}} \exp\left(-\mathrm{i} \int_{t_0}^{t} H(\tau)\, \mathrm{d}\tau\right), \tag{2.2}$$

where $H(t)$ is the total interacting Hamiltonian of the system and the bath, $\hat{\mathcal{T}}$ is the time-ordering operator, then the density operator at any time t can be computed as

$$\rho(t) = U(t, t_0)\rho(t_0)U^\dagger(t, t_0). \tag{2.3}$$

Eventually, the density operator of the reduced system at time t is readily found by tracing out the bath degrees of freedom,

$$\rho_S(t) = \mathrm{tr}_B\, \rho(t), \tag{2.4}$$

thus allowing for the evaluation of any observable of the reduced system.

A useful numerical approach to calculate $U(t, t_0)$ is the short-iterative Lanczos method (SIL) [118, 119], which can be employed

to propagate the full system-bath quantum state $|\Psi(t)\rangle$ at time t, once the starting state $|\Psi(t_0)\rangle$ is known. This technique combines a projection scheme of the full Hamiltonian $H(t)$ to a truncated state space and exact diagonalization methods. While conventional approaches describe the influence of the bath degrees of freedom on the reduced systems in terms of an analytically exact effective interaction potential, here the main difficulty resides in finding a suitable truncation scheme of the bath Hilbert space, which could successfully describe the dynamics of $\rho_S(t)$, at least in a range of model parameters.

To pursue this goal, we start by discretizing the bosonic spectrum by considering M equally spaced modes, having frequencies

$$\omega_k = \frac{\omega_c}{M}\, k, \qquad k = 1, \dots, M. \tag{2.5}$$

The bath space state is spanned by the basis $\{\, |n_1, n_2, \dots, n_M\rangle \,\}$, where $n_k = 0, \dots, N_{\max}$ is the number of excitations in mode k, up to a cut-off $N_{\max}$. We integrate the spectral density function in Eq. (1.10) around each mode, and extract the couplings λ_k which are able to reproduce the correct spectral density of the bath up to some desired level of accuracy, controlled by M. For sufficiently large M, the integral can be approximated by the mean value theorem as

$$\lambda_k^2 \approx 2\alpha \frac{\omega_k^s}{\omega_c^{s-1}}\, \delta\omega \equiv 2\alpha\omega_c^2 \frac{k^s}{M^{s+1}}, \tag{2.6}$$

where $\delta\omega = \omega_c/M$. This uniform sampling is the simplest choice, and allows us to reach convergence in all the investigated regimes, as we will show in the next section. Different samplings have also been proposed in the literature [58, 117, 124, 125].

Further, the truncation scheme to be performed on the set of bath states clearly depends on the value of the coupling strength α. As evident from Eq. (1.44), the creation or annihilation of a boson in a certain state k leads to a variation in the occupation number n_k with respect to its thermal equilibrium value n_k^{eq}, fixed by the Boltzmann distribution. In the following, we will denote as N_{ph} the absolute maximum number of bosonic excitations, with respect to the thermal equilibrium. Performing the truncation of the Hilbert space to those states with $\Delta n_k = n_k - n_k^{\mathrm{eq}} = \{\, 0, \pm 1, \pm 2, \dots, \pm N_{\mathrm{ph}} \,\}$, with $\sum_k |\Delta n_k| \leq N_{\mathrm{ph}}$, a numerically exact description of the system-bath dynamics can be obtained up to terms proportional to $\alpha^{N_{\mathrm{ph}}}$. In the weak coupling regime (WC), we find that a correct description can be obtained by choosing $N_{\mathrm{ph}} = 1$; we emphasize that, at WC, our approach recovers the Lindblad results in the limit of extremely weak coupling strengths. For increasing values of α, we can fine-tune our results by progressively adding more states to the bath Hilbert space, corresponding to multiple excitations from the equilibrium state; the computational resources needed to simulate the system dynamics at these couplings are necessarily heavier, but calculations remain

affordable in the intermediate coupling (IC) regime, where $N_{\mathrm{ph}} = 3$ is enough to get a good quantitative description of the dynamics. As a consequence, this approach is well-suited to describe the correct physical behavior of the system in a parameter range going from weak to intermediate coupling.

Once the final set of basis states has been fixed, an iterative calculation of the state $|\Psi(t_{\mathrm{f}})\rangle$ can be set up for any final time t_{f} in the following way. First, we divide the entire time interval in subintervals of fixed duration $\mathrm{d}t$. Then, for every fixed time interval $[t, t+\mathrm{d}t]$, we evaluate the Hamiltonian at midpoint and project it onto the subspace $\mathcal{K} = \{\, |\Psi(t)\rangle, H\,|\Psi(t)\rangle, \ldots, H^n\,|\Psi(t)\rangle \,\}$, where $|\Psi(t)\rangle$ is the full system state at time t and n is the minimum number of vectors needed to achieve convergence. An orthonormal basis of vectors in $\mathcal{K}$ is given by the set of Krylov vectors $\{\, |\Phi_k\rangle \,\}_{k=1}^{n}$, obtained by recursive Gram-Schmidt orthogonalization techniques. The reduced Hamiltonian $\tilde{H}$ in the n-dimensional Krylov subspace can thus be obtained as

$$\tilde{H} = \mathcal{P} H \mathcal{P}^{\dagger}, \tag{2.7}$$

where $\mathcal{P}$ is the projector operator into the Krylov subspace at time t; following the chosen time discretization, the evolution operator $\tilde{U}(t+\mathrm{d}t\,, t)$ can be recast as follows:

$$\tilde{U}(t+\mathrm{d}t\,, t) \simeq \exp\big[-\mathrm{i}\,\tilde{H}(t+\mathrm{d}t\,/2)\,\mathrm{d}t\big]. \tag{2.8}$$

The minimum dimension n to achieve convergence depends on $\mathrm{d}t$; its typical values are of the order of 20 to 100, thus allowing the numerical evaluation of Eq. (2.8) by means of direct diagonalization of the matrix $\tilde{H}(t+\mathrm{d}t\,/2)$. Eventually, expanding the state $|\Psi(t)\rangle$ in terms of the eigenvectors of $\tilde{H}(t+\mathrm{d}t\,/2)$, the full state of the system at time $t+\mathrm{d}t$ can be evaluated by straightforward matrix products. This procedure turns out to be particularly useful if the matrix H is Hermitian, because in that case the reduced matrix $\tilde{H}(t+\mathrm{d}t\,/2)$ has tridiagonal form and thus can be easily diagonalized.

One intrinsic limitation of this approach is that it is valid only up to a specific upper time scale. The minimum frequency ω_1 determines the Poincaré recurrence time $t_{\mathrm{p}} = 2\pi/\omega_1$, which is an upper limit for the total evolution time that can be studied with this method. After t_{p}, the collection of harmonic oscillators ceases to be a good approximation of an ergodic thermal bath. Hence, realistically, this numerical approach is not feasible to study very long time (adiabatic) dynamics, except in the WC regime, where the Hilbert space scales linearly with M, allowing to simulate a large number of modes (up to 10^6) and, consequently, moderately long times.

On the other hand, short time dynamics is well-described even with a limited number of modes, both in WC and IC. That is where our method proves its usefulness. This allows us to study memory effects, which are considered of great interest in real, experimentally

controllable, baths [113, 114]. Nonetheless, our method provides the whole system + bath wave function. With a change of perspective, this could be useful to test the influence of the reduced system over the environment, and this is potentially interesting for studying structured environments with a limited number of degrees of freedom.

2.2 SPIN-BOSON MODEL

In what follows, we analyze the dynamics of SBM with longitudinal coupling to the bath as in Eq. (1.11) by means of the SIL technique described in Sec. 2.1. Then, we compare our numerical results with their analytical closed-form counterparts which can be obtained from the Lindblad equation in Eq. (1.29).

Below, we slightly change our notation, by rewriting the tunneling element Δ and the coupling element λ_k in Eq. (1.11) such that $\Delta/2 \to \Gamma$, $\lambda_k \to 2g_k$. It is equivalent to rewriting the Hamiltonian Eq. (1.11) as follows

$$H = -\varepsilon\sigma_z - \Gamma\sigma_x + \sum_k \omega_k b_k^\dagger b_k + \sigma_z \sum_k g_k (b_k^\dagger + b_k). \tag{2.9}$$

We call η the new adimensional coupling strength, so that $\alpha = 2\eta$. Furthermore, we adopt a different cutoff function, so that the bath spectral density function takes the form

$$J(\omega) = \sum_k g_k^2 \delta(\omega - \omega_k) = \eta \frac{\omega^s}{\omega_c^{s-1}} \Theta(\omega_c - \omega). \tag{2.10}$$

This change of notation is adopted only in this Chapter, as we want to describe the properties of quantum annealing in the next section.

We first restrict to the unbiased case $\varepsilon = 0$, i. e., $H_S = -\Gamma\sigma_x$, and we take the temperature $T = 0$. We choose a cut-off frequency $\omega_c = 10\Gamma$, take the coupling parameter η in the range $\eta = 5 \cdot 10^{-4}$ to $1 \cdot 10^{-1}$, and assume $s = \{1/2, 1, 2\}$; in addition, following this choice of parameters, we perform the basis truncation including up to three excitations per mode ($N_{\text{ph}} = 3$). We prepare the system at time $t = 0$ in a linear combination of the basis states at fixed starting values $\langle\sigma_x(0)\rangle = \langle\sigma_z(0)\rangle = 1/2$, i. e., $|\psi(0)\rangle = \cos(\xi/2)\,|\hat{z};+\rangle + \sin(\xi/2)\exp(i\phi)\,|\hat{z};-\rangle$, with $\xi = \pi/3$ and $\phi = \operatorname{acos}(1/\sqrt{3})$. Then, we compute the time-evolved mean values $\langle\sigma_x(t)\rangle$ and $\langle\sigma_z(t)\rangle$, extracted from the reduced density matrix $\rho_S(t)$, and eventually compare them with the corresponding results based on the Lindblad equation.

In Fig. 2.1, we show the results for $\langle\sigma_z(t)\rangle$ in the IC regime, in the case of Ohmic dissipation, for different values of the maximum number of excitations per mode N_{ph}, compared with the result predicted by the Lindblad equation in Eq. (1.29). Choosing a minimum value of $N_{\text{ph}} = 2$, the time evolution of $\langle\sigma_z(t)\rangle$ converges to the right physical

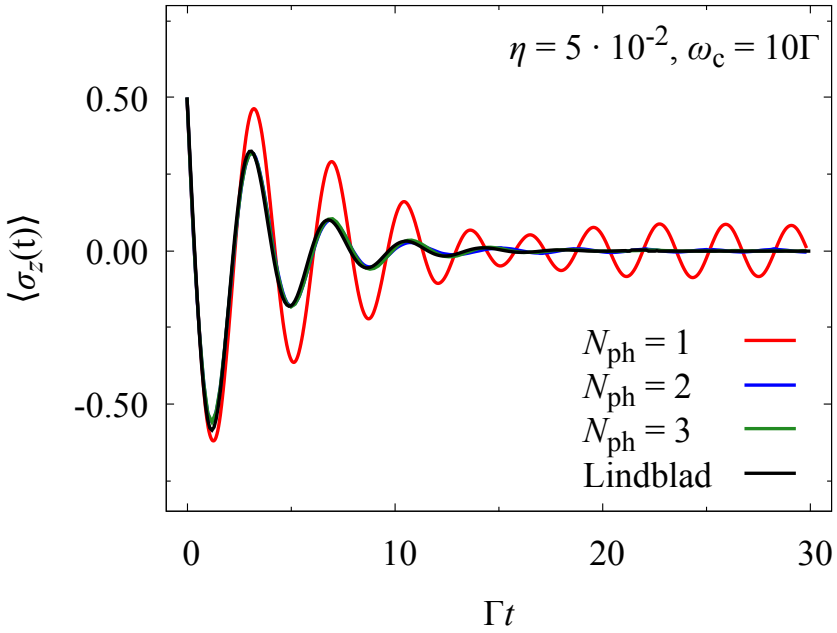

Figure 2.1: Time evolution of $\langle\sigma_z(t)\rangle$ for an unbiased qubit in an Ohmic bath ($s = 1$), having chosen $\eta = 5 \cdot 10^{-2}$, $\omega_c = 10\Gamma$ and $T = 0$. We fixed $M = \{1000, 500, 300\}$, for $N_{ph} = \{1, 2, 3\}$, respectively. SIL results are plotted against the Lindblad curve (solid black curve), from Eq. (a.13).

behavior, which shows underdamped oscillations due to decoherence and dissipation effects. It follows that at long times the equilibrium value $\langle\sigma_z^{eq}\rangle = 0$ is reached and the populations of the two levels assume their stationary value.

Notice that, as expected, these features do not depend on the starting condition. In the main plot of Fig. 2.2, we support this statement by comparing the dynamics for our choice of the initial state with the more traditional $|\psi(0)\rangle = |\hat{z}; +\rangle$. Here it can be clearly seen that both the decay rate and the oscillation frequency are preserved; in order to emphasize this, we shifted one of the curves to make them in phase. Simulation parameters are the same as Fig. 2.1 and we chose $N_{ph} = 2$. The exact functional form of $\langle\sigma_z(t)\rangle$ is not known. However, as anticipated in 1.2, several theoretical arguments [49] show that the interaction with the environment is responsible for a renormalization of the tunneling amplitude (and, correspondingly, of the spectral gap of the qubit system), depending on the coupling strength, of the form

$$\Gamma_r = \Gamma \left(\frac{2\Gamma}{\omega_c}\right)^{\frac{2\eta}{1-2\eta}}. \tag{2.11}$$

Furthermore, the properties of the underdamped oscillations of the magnetization $\langle\sigma_z(t)\rangle$ can be described by means of the quality factor Ω/γ, where the frequency Ω and the damping factor γ are related

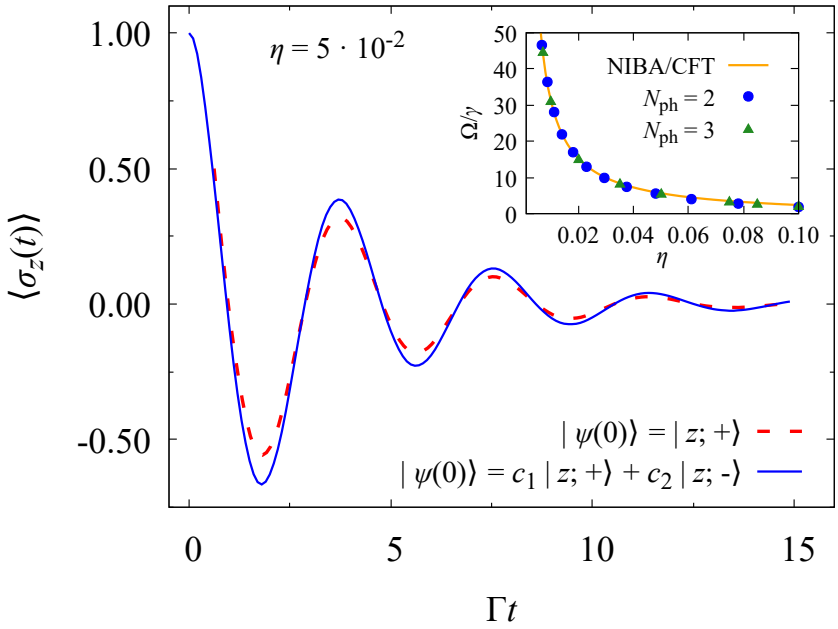

Figure 2.2: Time evolution of $\langle\sigma_z(t)\rangle$ for an unbiased qubit in an Ohmic bath ($s = 1$), with $\eta = 5 \cdot 10^{-2}$, $\omega_c = 10\Gamma$ and $T = 0$, and two different starting conditions: the traditional $|\hat{z};+\rangle$ and the state $c_1|\hat{z};+\rangle + c_2|\hat{z};-\rangle$, with $c_1 = \cos\xi$ and $c_2 = \exp(i\phi)\sin\xi$ (see the main text for their definition). In the inset, SIL results for the quality factor as a function of the coupling parameter, compared with conformal field theory and NIBA (solid orange line) [76]; in the IC regime, increasing the phonon number is necessary to improve the accuracy.

to the tunneling amplitude. As anticipated in Chpt.1,] despite its limitations, NIBA [49] yields correct predictions for the quality factor, which are also in agreement with conformal field theory [76]. It reads

$$\frac{\Omega}{\gamma} = \cot\frac{2\pi\eta}{2(1-2\eta)}. \tag{2.12}$$

Assuming a simple functional form for the underadamped oscillations, i. e. $\langle\sigma_z(t)\rangle = A\cos(\Omega t + \mu)\exp(-\gamma t)$, we can extract from our numerical simulations good estimates for the parameters of interest as function of the the dissipation strength η. In the inset of Fig. 2.2, we show that the SIL method succesfully recovers the behavior of the quality factor in the entire range of investigated coupling strengths.

On the other hand, in Fig. 2.3 we analyze the numerical results for the time evolution of $\langle\sigma_x(t)\rangle$ obtained by means of SIL technique, plotted against the result predicted by the Lindblad equation reported in Eq. (1.29) and (a.13); our results exhibit a non-monotonic behavior at short times, while a prominent saturation behavior at long times can be observed, for every value of N_{ph}. Analogous properties hold for the time evolution of this observable in the sub-Ohmic and super-Ohmic

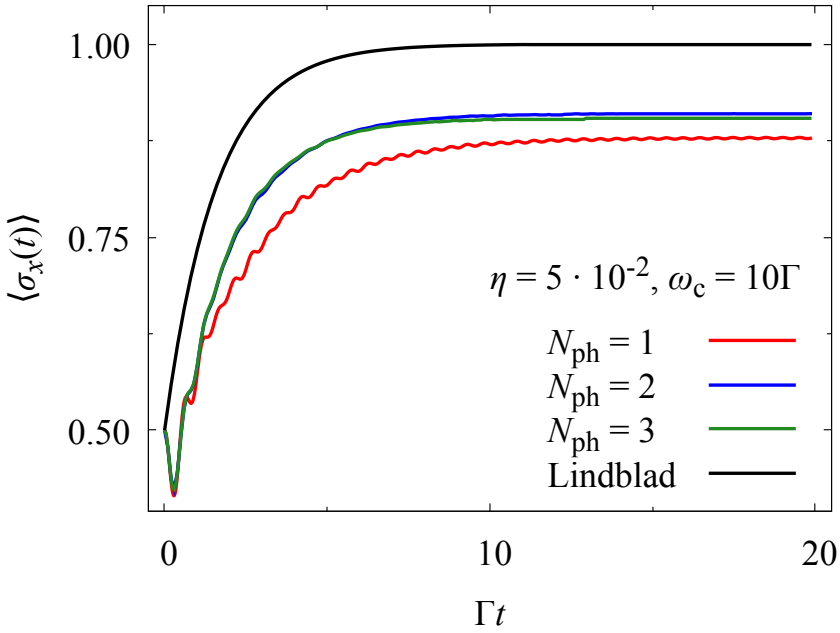

Figure 2.3: Time evolution of $\langle\sigma_x(t)\rangle$ for the same parameter values as in Fig. 2.1. The non-monotonic region occurs at short times $0 < \Gamma t < 2.5$ while at long times the curve saturates to a well-defined equilibrium value.

cases (see Fig. 2.4), provided that the analysis is restricted to WC and IC regimes. As shown in Fig. 2.4, the three saturation curves, in the same parameter region as in Fig. 2.1, clearly differ in the equilibration times as well as in the equilibrium values σ_x^{eq}.

As can be inferred from Fig. 2.3, our results remarkably differ from the Lindblad one, because the latter predicts as the long-time stationary value the one corresponding to the ground state of the qubit Hamiltonian disentangled from the bath. Instead, our calculations show that the stationary value is related to the ground state of the qubit-bath system: at long times, qubit and bath remain entangled, as expected at equilibrium.

While such a striking difference can be observed in the equilibrium values of $\langle\sigma_x(t)\rangle$ obtained by using SIL and the Lindblad equation, the relaxation rates are very similar in the two approaches. As a deeper analysis of Figs. 2.1 and 2.3 shows, the Lindblad result for $\langle\sigma_z(t)\rangle$ qualitatively agrees with the SIL result, correctly predicting the underdamped oscillating behavior, which takes place in a time T_2 depending on the energy gap 2Γ, temperature and the damping parameter η (see Eqs. (a.13)).

Note also that the time dependence obtained by the SIL method with $N_{ph} = 1$ fails to recover the correct physical behavior suggesting that, as expected, the Lindblad solution includes multiple uncorrelated scattering processes. On the other hand, as previously discussed, the

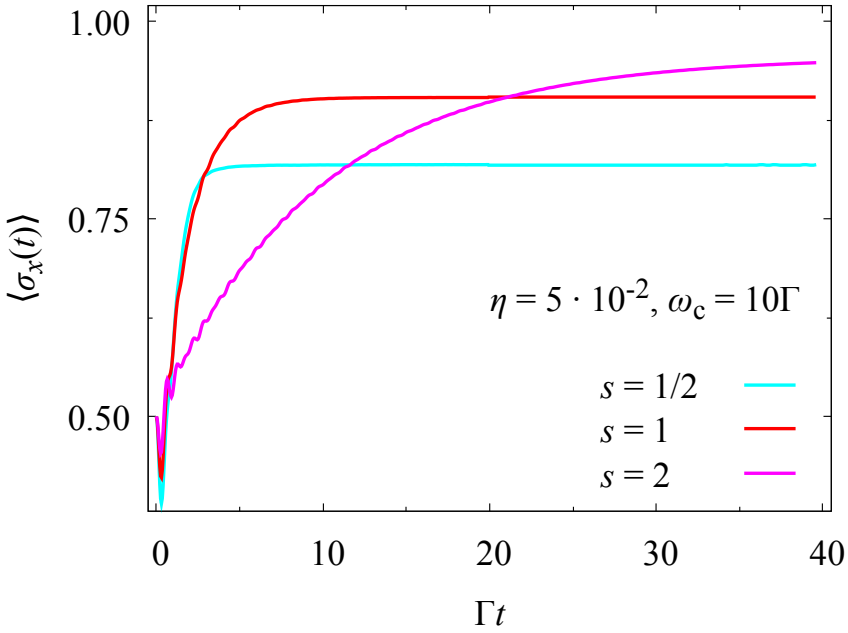

Figure 2.4: Time evolution of $\langle\sigma_x(t)\rangle$ for the same parameter values as in Fig. 2.1, for three different dissipations considered $s = \{1/2, 1, 2\}$. Both the equilibration times and saturation values depend on s.

Lindblad result for $\langle\sigma_x(t)\rangle$—equal to the difference in populations of states $|\hat{x};\pm\rangle$—saturates towards the wrong asymptotic value after a time $T_1 = T_2/2$ (see App. a). In this case, correlations among multiple scattering processes, correctly included by our approach, play a relevant role.

In addition, while the relaxation times are correctly reproduced, we note that the Lindblad approximation in Eq. (a.13) does not take into account the non-monotonic behavior of $\langle\sigma_x(t)\rangle$ at very short times, as shown in Fig. 2.3. This behavior can be understood by carrying out a detailed analysis of the time evolution of each contribution to the expectation value of the total Hamiltonian in Eq. (2.9). As shown in Fig. 2.5, at short times the absolute value of the system-bath interaction energy $\langle H_{SB}(t)\rangle$ rapidly grows up to an absolute maximum and, as a consequence, both the reduced system and the bath undergo an excitation from their initial states, while the total energy remains constant in time. After this brief transient time, depending on the chosen initial condition, the expectation value of the reduced system energy $\langle H_S(t)\rangle$, as well as $\langle H_B(t)\rangle$ and $\langle H_{SB}(t)\rangle$, saturates towards its equilibrium value.

The previous results suggest that, moving from WC to IC, a physical description of the dynamics of the SBM entirely based on the Lindblad equation can suffer from severe limitations, in agreement with theoretical [75] and experimental findings [113, 114]. On the other hand, the

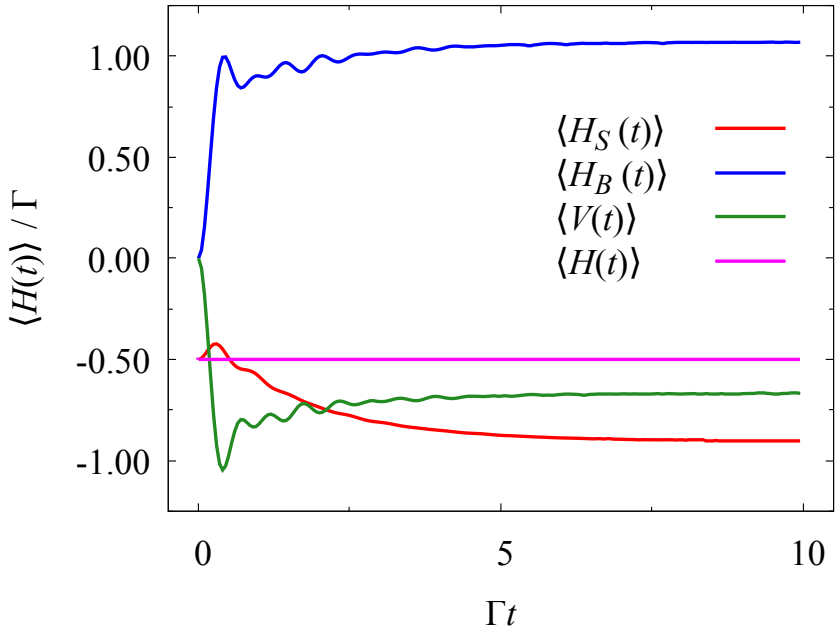

Figure 2.5: Time evolution of $\langle H_S(t)\rangle$, $\langle H_B(t)\rangle$, $\langle H_{\rm SB}(t)\rangle$, and $\langle H(t)\rangle$, in units of Γ, for an Ohmic bath with $M = 300$, $N_{\rm ph} = 3$, $\eta = 5 \cdot 10^{-2}$ and $\omega_{\rm c} = 10\Gamma$.

SIL approach can successfully reproduce the correct physical scenario in this parameter region. In order to provide further evidence for it, we study the equilibrium values $\sigma_x^{\rm eq}$ as a function of the coupling parameter η for the three different kinds of dissipation mentioned before, choosing the maximum number of excitations per mode up to $N_{\rm ph} = 3$.

In order to obtain reliable values of $\sigma_x^{\rm eq}$, we performed an exponential fit of the numerical results $\langle\sigma_x(t)\rangle$ and extracted the best estimates of the saturation values. In Figs. 2.6, 2.7 and 2.8, we show the fitted equilibrium values $\sigma_x^{\rm eq}$ as a function of the coupling parameter η compared with the Lindblad result. We also plot the equilibrium values calculated using a Monte Carlo approach at thermal equilibrium (orange filled diamonds), with the purpose of further testing the reliability of our calculations. We note that, as the coupling factor becomes larger than 10^{-3}, the Born-Markov approach misses the correct physical behavior for every bath spectral distribution considered. It follows that, at long times, the unavoidable system-bath entanglement effects start to play a role, noticeably reducing the value of $\sigma_x^{\rm eq}$. This effect becomes particularly evident in the case of sub-Ohmic dissipation, which shows a rapid decrease of the $\langle\sigma_x(t)\rangle$ as η reaches 10^{-2}. This is due to the fact that, in this case, the critical coupling strength at which the quantum phase transition of the SBM [49] occurs is smaller than in the Ohmic case [58, 124], explaining the observed quantitative difference between Monte Carlo data and SIL predictions. On the other

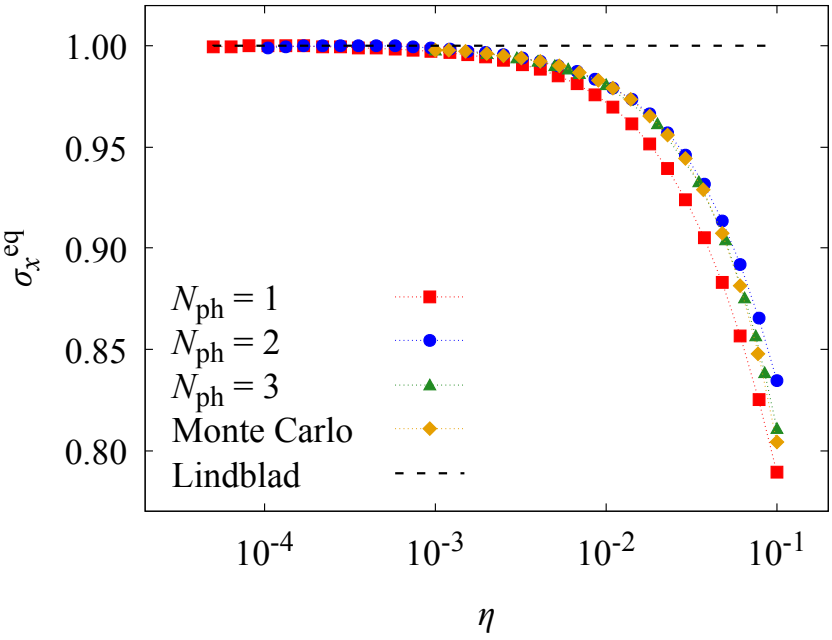

Figure 2.6: Semi-logarithmic plot of the saturation value σ_x^{eq}, extrapolated with exponential fits, as a function of the dimensionless coupling η, at $T = 0$, for an Ohmic bath ($s = 1$). The simulated data of the numerical diagonalization, up to $N_{ph} = 3$ bosonic excitations from the vacuum state, are compared to Lindblad and Monte Carlo predictions at equilibrium. The ranges of parameters where the physics is ruled either by single or multiple-phonon processes are easily distinguishable by those values of η where the curve at different N_{ph} separate.

hand, in the Ohmic and super-Ohmic case a good physical description can be achieved by truncating the phonon bases to three excitations per mode, as long as the coupling factor is weaker than 10^{-1}.

Following these results, we can apply the SIL technique to perform an analogous analysis for the biased case ($\varepsilon \neq 0$). Here, the gap between the qubits states changes to a constant value equal to $E_g = 2\sqrt{\varepsilon^2 + \Gamma^2}$, the eigenstates being linear superpositions of the computational basis states. The biased case is of particular interest for us, since it has been shown that the NIBA, predicting the qubit localization in the state $|\hat{z}; -\rangle$ at long times, fails to describe the correct physical behavior [49, 86]. We can therefore further test the predictions of our numerical technique by analyzing the asymptotic behavior of $\langle \sigma_z(t) \rangle$. By turning back to the $|\hat{z}; \pm\rangle$ basis, we prepare the qubit at initial time in the state $|\hat{z}; +\rangle$ and simulate the time evolution of the biased system in WC, by fixing the values $\varepsilon = -\Gamma$, $\eta = 5 \cdot 10^{-3}$ and $T = \{ 0, 0.1 \}$ in units Γ.

As shown in Fig. 2.9, the numerical results for $\langle \sigma_z(t) \rangle$ clearly indicate an asymptotic value that, while differing from the NIBA ($\langle \sigma_z(\infty) \rangle_{NIBA} = \tanh(\beta\varepsilon/2)$) [49], is consistent with that obtained by means of WIBA

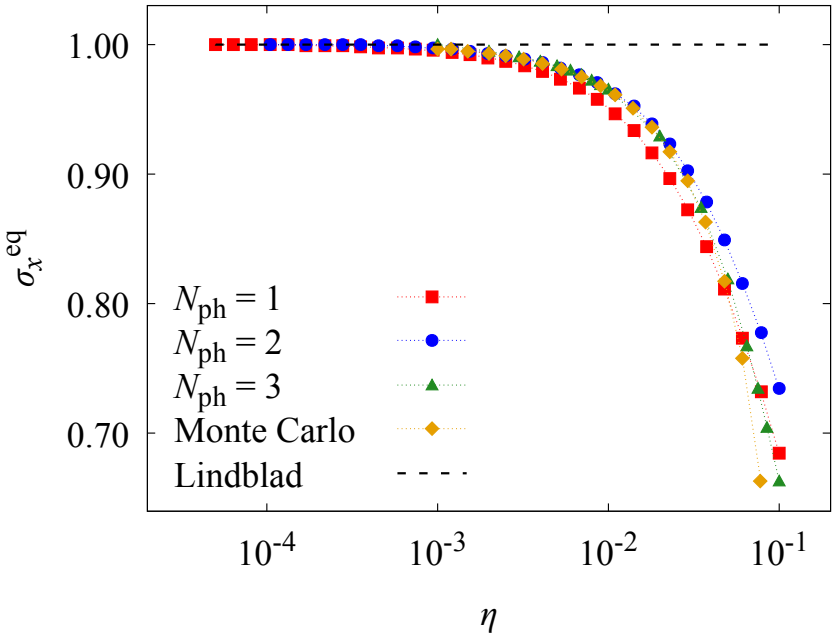

Figure 2.7: Same as Fig. 2.6, but for a sub-Ohmic bath ($s = 1/2$).

approach [86]. It follows that our method can provide an accurate description of correlation effects, and it can be fruitfully used to describe the physics of these system even in the IC regime. In addition, a more detailed numerical analysis may be pursued in order to measure in a systematic way the differences between our result and the WIBA predictions.

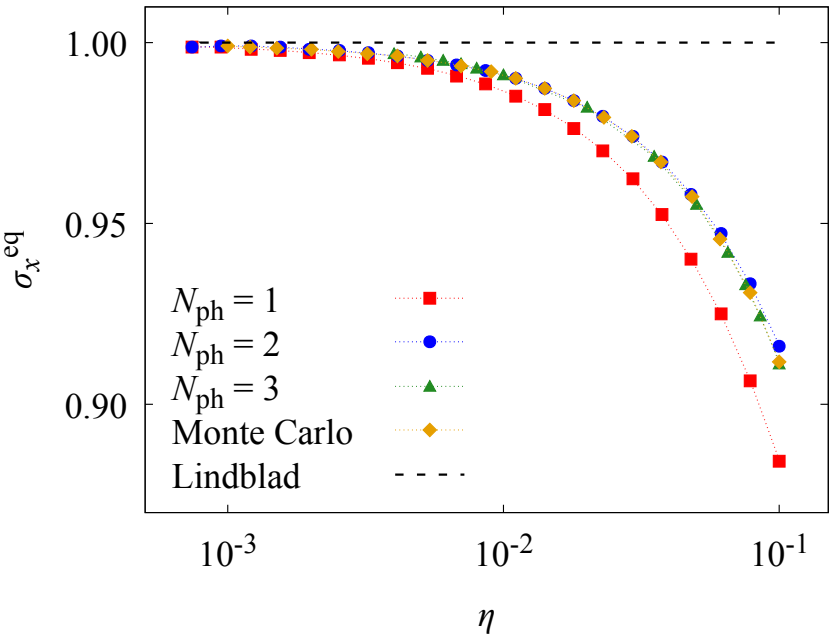

Figure 2.8: Same as Fig. 2.6, but for a super-Ohmic bath ($s = 2$). In presence of a super-Ohmic bath, because of the reduced number of low-energy bosons, equilibrium is reached more slowly and it is difficult to extrapolate σ_x^{eq} at WC.

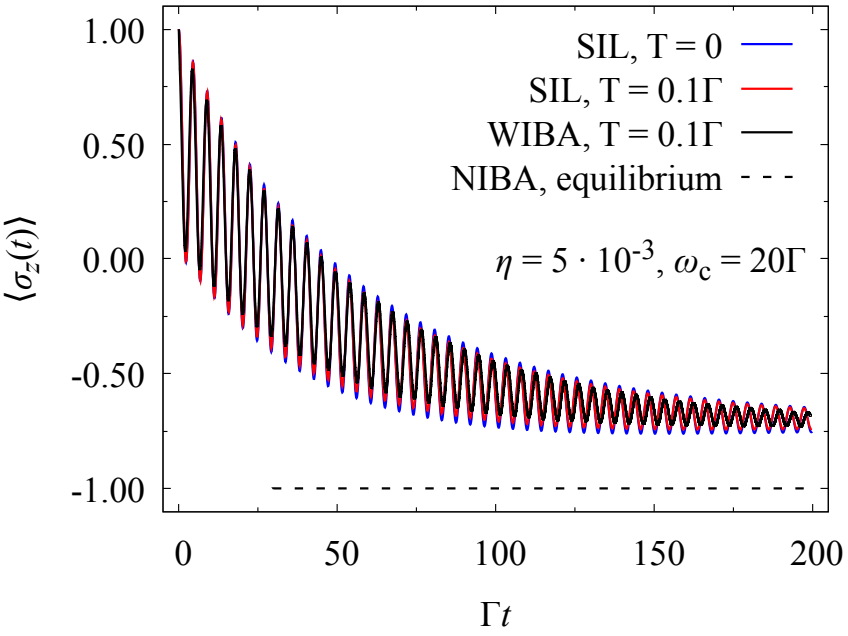

Figure 2.9: Time evolution of $\langle\sigma_z(t)\rangle$ for the biased case and Ohmic dissipation, obtained by choosing $\varepsilon = -\Gamma$, $\eta = 5 \cdot 10^{-3}$, $\omega_c = 20\Gamma$, $N_{ph} = 2$, and $T = \{0, 0.1\}$ in units Γ (red and blue solid curves). The asymptotic value, while differing from that predicted by NIBA, fairly agrees with WIBA results (solid black curve), extracted from Ref. [86].

2.3 QUANTUM ANNEALING

Here we focus on a typical quantum annealing problem, where we choose a time dependent TLS Hamiltonian as in Eq. (1.42). We study the dynamics of a TLS where both the tunnelling element and the bias field change in time following a linear interpolating schedule. This driving is typical in AQC setting [20, 97], where in place of the single TLS more complex models of interacting Hamiltonian are employed.

Below, we slightly change our notation, by rewriting the time-dependent field as $\Delta(t)/2 \to \Gamma(t) = (1 - t/t_f)\Gamma$ and $\varepsilon(t)/2 \to \varepsilon t/t_f$, where t_f is the final annealing time,so that the TLS Hamiltonian reads

$$H_S(\theta) = -(1-\theta)\Gamma\sigma_x - \theta\varepsilon\sigma_z. \tag{2.13}$$

Here $\theta = t/t_f \in [0,1]$ is a dimensionless time. We choose the transverse field Γ as our reference energy scale and fix $\varepsilon = \Gamma$. As prescribed by AQC, we start by preparing the reduced system at $\theta = 0$ in the instantaneous eigenstate of $H_S(0)$, i. e., a fully displaced state having maximum kinetic energy, and we let it evolve towards the localized ground state of $H_S(1)$. The environment is initialized in its thermal equilibrium state, and, in order to keep the discussion simple, we restrict to the case $T = 0$.

With our SIL method, we are able to simulate both short and long time dynamics, while the usually employed tools for simulating AQC algorithms strictly require long annealing times ($t_f \to \infty$) in order to provide reliable results. Among these tools, the Lindblad equation (1.29) for the reduced ground state occupation probability can be solved analytically in the adiabatic limit [20], and provides the solution, in the instantaneous eigenbasis of $H_S(\theta)$,

$$\rho_{--}(\theta) = \frac{1}{G(\theta)}\left[\rho_{--}(0) + \int_0^\theta F(\theta')G(\theta')\,\mathrm{d}\theta'\right], \tag{2.14}$$

where, at zero temperature,

$$G(\theta) = \exp\int_0^\theta F(\theta')\,\mathrm{d}\theta', \tag{2.15}$$

$$F(\theta) = t_f\,\xi^2(\theta)\gamma\big(E_g(\theta)\big), \tag{2.16}$$

$$\xi(\theta) = 2\Gamma\frac{1-\theta}{E_g(\theta)}, \tag{2.17}$$

and $E_g(\theta)$ is the instantaneous reduced spectral gap. Eq. (2.14) predicts that, at long t_f, the fidelity saturates to $\rho_{--} = 1$ independently of the system-bath coupling strength η, which only affects the characteristic relaxation time, proportional to η^{-1}. This reflects the Born-Markov approximation: the bath state is uncorrelated with the reduced system state, hence, in this picture, the only effect of the zero-temperature reservoir is to drive the TLS towards its ground state. However, as discussed in Sec. 2.2, in IC this picture is misleading as entangled

system-bath states may arise, significantly modifying the occupations of the qubit eigenstates.

In order to catch the correct physics in this interesting regime, we coupled this system to $M = 200$ modes, each possibly occupied by maximum $N_{\rm ph} = 3$ phonons. At $\theta = 1$, we compute the excess energy $\varepsilon_{\rm res}$ with respect to the reduced ground state energy $\varepsilon_{\rm gs} = -\varepsilon$. For a TLS, $\varepsilon_{\rm res}$ is proportional to the ground state error $1 - \rho_{--}$, i. e.,

$$\varepsilon_{\rm res} \equiv {\rm tr}[H_S(1)\rho_S(1)] - \varepsilon_{\rm gs} = 2\varepsilon[1 - \rho_{--}(1)]. \tag{2.18}$$

In Fig. 2.10, we compare the excess energy, in units Γ, as a function of the final annealing time (in units $1/\Gamma$) of several TLSs, coupled with different strengths η to an Ohmic environment. Similar curves, obtained by numerical integration of the Lindblad equation using a fourth-order Runge-Kutta routine, are shown in Fig. 2.11. By comparing the curves, it is evident that system-bath correlations, disregarded by the Lindblad QME, modify quantitatively and also qualitatively the behavior of the solution in the analyzed time range, hence a Born-Markov dynamics is not able to reproduce the correct behavior.

In fact, in the Lindblad picture of Fig. 2.11, the only noticeable effect of progressively increasing system-bath coupling strength is a very small damping of the amplitude of short-time oscillations in the ground state occupation, while both the function profile at short times and the long times power-law tail are preserved in the presence of a dissipative environment. By contrast, what we found with SIL method (Fig. 2.10) is that, while the description at short times is in agreement with Lindblad results, at intermediate times system-bath correlations tend to increase the value of the excess energy with respect to the isolated case $\eta = 0$, and this feature is not present in the QME solution. In fact, at intermediate times we observe a transient plateau, anticipating a further decrease in the excess energy towards the solution of the isolated case. As the exhaustion time of the plateau inversely depends on η, we observe a non-monotonic behavior of the excess energy as a function of η in the time window where this decrease takes place. The oscillations in the excess energy of the closed system are well-known and due to the finite annealing time of the chosen schedule. The effect of the environment is to suppress these oscillations in the open system case. Moreover, the excess energy of the open system can become smaller than its closed system counterpart, but this effect can only occur at some particular values of the final annealing times. It is evident in the inset of Fig. 2.10, showing that eventually, at longer annealing times, the curve corresponding to $\eta = 10^{-2}$ approximately tends to the mean value of the closed system oscillating pattern. Whether or not this feature survives also at low but finite temperature is currently under investigation.

As for the analysis at the end of Sec. 2.2, concerning the oscillation frequency of $\langle\sigma_z(t)\rangle$, it may be tempting to explain the influence of

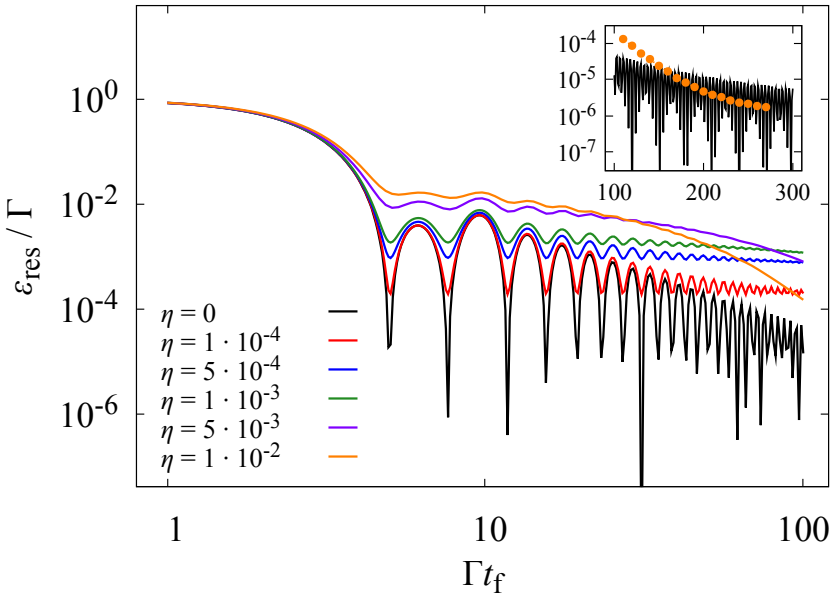

Figure 2.10: Excess energy, in units Γ, as a function of the final annealing time, in units $1/\Gamma$, for coupling strengths η going from zero to 10^{-2}. Simulations involve $M = 200$ bosonic modes at $T = 0$, with $\omega_c = 10\Gamma$ and $N_{ph} = 3$ (Ohmic bath). At short times, the environment does not have the time to act and the system always stays close to the isolated solution. At intermediate times, the residual energy shows a plateau. At longer times, a further decrease of ε_{res} brings the solution again towards the isolated case. At these time scales, this effect is visible only at IC. The inset focuses on longer annealing times (reached using $M = 450$ modes) and follows the same color scheme as the main plot. Here, we show that at long times the effect of the bath may be beneficial for the annealing.

the environment on the quantum annealing in terms of a renormalization of the spectral gap of the reduced system. According to this argument, however, we should always expect a decrease of quantum annealing performances due to the gap reduction in the presence of the bath. Moreover, we should observe a progressive worsening of the annealing performances with increasing η due to this effect (see Eq. (2.11)). This argument reduces the full system to an effective TLS with renormalized spectral gap, which is a completely satisfactory description of time-independent problems as the SBM in Sec. 2.2, but cannot rigorously reproduce the dynamical behavior of a system with time-dependent Hamiltonian.

To show that the previous picture might be misleading, recall that the physical description of a quantum annealing process can be un-

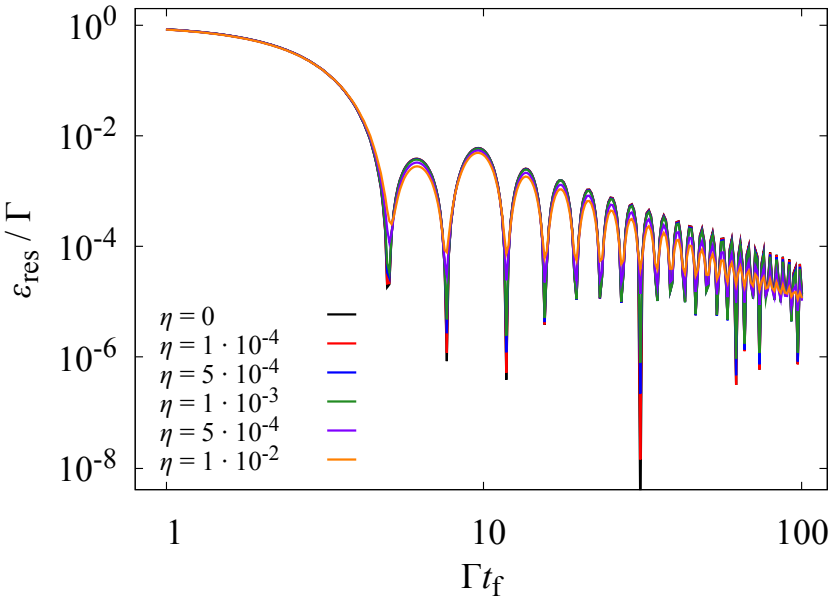

Figure 2.11: Excess energy, in units Γ, as a function of the final annealing time, in units $1/\Gamma$, for coupling strengths η going from zero to 10^{-2}, simulated using the Lindblad master equation at $T = 0$ and a cut-off frequency $\omega_c = 10\Gamma$ (Ohmic bath). The only noticeable effect of increasing η is the progressive damping of short time oscillations in the ground state occupation, but the plateau and the following decrease of $\varepsilon_{\mathrm{res}}$ observed in Fig. 2.10 are not recovered.

derstood in terms of the Landau-Zener (LZ) model [126, 127]. The LZ Hamiltonian reads

$$H_{\mathrm{LZ}}(t) = -\frac{vt}{2}\sigma_z - \frac{\Delta}{2}\sigma_x, \tag{2.19}$$

it has a minimum spectral gap Δ at $t = 0$ and in this case the TLS system evolves from $t = -\infty$ to $t = +\infty$ with sweep velocity v. The adiabatic limit holds when $v \to 0$. It has been shown in many works [96, 128, 129] (see also Sec. 1.4.1) that a zero-temperature thermal bath longitudinally coupled (i. e., via σ_z) to the LZ system cannot provide any thermal speed-up with respect to the isolated dynamics for any sweep velocity v, i. e., the probability of finding the system in its ground state at $t = +\infty$ coincides with that of the closed system and is η-independent. This exact result holds exclusively for an evolution from $t = -\infty$ to $t = +\infty$ and proves that, even though a renormalization of the minimal gap occurs, this does not necessarily lead to a decrease in the annealing performances.

Our Hamiltonian (2.13) inherently differs from the LZ model (2.19), thus the aforementioned theorem does not apply here. The LZ sweep velocity is inversely proportional to our final annealing time t_f, which

is always finite: $v \propto 1/t_f$. The excess energy in LZ is computed at $t = +\infty$, while we always compute it at $t = t_f < \infty$. The finiteness of t_f, experimentally more realistic than the limit $t_f \to \infty$, is responsible for the oscillations of the residual energy in the isolated case; as a consequence, the excess energy in the open quantum annealing of the system Hamiltonian (2.13) can be inside these oscillations at long times, causing a "partial speed-up" (i. e., occurring only at specific final annealing times t_f) of the annealing procedure due to the environment.

2.4 CONCLUSIONS

In this chapter, we showed that a numerical technique based on the iterative application of the time evolution operator, obtained by an appropriate reduction of the problem in the Krylov subspace, is well-suited for describing decoherence and dissipation effects in systems where a qubit interacts with an external bath. Tuning the number of bosonic modes and the corresponding maximum occupations of single-particle basis states, this technique allows the perturbative inclusion of relevant phononic processes in the dynamics of the reduced system, and enables to correctly describe time-correlation effects owing to the bath influence, ranging from weak to intermediate couplings. We emphasize that, within the proposed approach, both the full and the reduced density operator are not affected by any limitation as in standard perturbative methods, as non-positivity or non-preserved trace.

The conceptual simplicity or our method and the ease of its numerical implementation allow a fine control on the limitations and possible sources of errors during the numerical simulations. Further, our technique, yielding the entire wave function of the system + bath, allows the calculation of all the observables related to either one of the two subsystems, or to both of them, for all kinds of dissipations. Quite recently, there has been a renewed interest in understanding the physics of structured baths and thermal reservoirs in general [130–132]. Thus, our technique might be a valid tool to provide some insights on this class of phenomena. In addition, it allows to study general many-body and time-dependent problems without modifying the structure of our code and with no loss of precision.

With our method, we tested the limits of a description entirely based on Born-Markov hypotheses and recovered known results, providing some insights on the reliability of known analytical approximations. We claim that this technique can be useful for studying simple open quantum systems and for simulating adiabatic quantum processors, perhaps in combination with other numerical tools such as NRG when the complexity grows. Moreover, it can be easily extended to the study of non-equilibrium behavior of many physical systems, e. g., qubits in

presence of structured baths, externally driven qubits, small clusters of spatially-correlated qubits immersed in external environments, or many-body Ising systems restricted to symmetry subspaces. In the following chapters, we will extensively employ this technique to simulate nonequilibrium behavior of TLS system under particular driving fields.

3 TOWARDS THE STRONG COUPLING REGIME.

In this chapter, we present part of our original contributions published in [133].

The prototypical SBM in Eq. (1.11) has been widely employed in the study of energy exchange in dissipative driven systems [134] from weak to strong coupling regimes. Further, the effect of a thermal environment on the ground state topology of SBM has been considered in recent works [45], showing that only local geometric properties are noticeably affected, while global properties remain unchanged as long as the system is in the delocalized phase, i. e. the coupling to the bath degrees of freedom does not exceed the critical value ($\alpha < \alpha_c = 1$).

In addition, the bath-induced non-adiabaticity in models of driven TLS subject to a sweep in the Bloch sphere has been addressed [45], and in the strong coupling regime the crossover from quasi-adiabatic to non-adiabatic dynamics due to the environment has been studied. While this picture holds true in the quasi-adiabatic regime, it is not a priori clear how the environment affects the dynamics of the TLS at not-so-low sweep velocities; furthermore, different forms of the coupling could lead to changes in this scenario, as stressed in several works [100, 128, 129] addressing the dissipative dynamics of Landau-Majorana-Stückelberg-Zener (LMSZ) model [126, 127, 135].

In this chapter, we extend the numerical study of the dissipative dynamics of SBM, begun in Chpt. 2, going from weak to strong coupling regime. By employing the numerical approach described in section 2.1, we first address the static field case, focusing on the biased SBM in contact with an Ohmic bath. Then, we consider a time-dependent protocol, which has been recently implemented in solid-state devices in order to realize dynamical measurements of topological phase transitions [136, 137].

We show that in the case of unbiased SBM our approach is successful in describing the crossover from coherent to incoherent behavior of magnetization dynamics, occurring at the Toulouse point at $\alpha = 1/2$ (see Sec. 1.3). In addition, taking advantage of our technique we find the dynamical evolution of the mean population of the bath modes as a function of time, and we observe a change from non-resonant to resonant response at fixed coupling strengths. Furthermore, in the case of the time-dependent protocol, we show a non-monotonic behavior of the fidelity at fixed final times as a function of the dissipation strength: this behavior, which is found to depend on the detailed form

of interaction with the environment, signals the complex interplay between non-adiabatic effects due to the external time-dependent driving force and dissipation.

The chapter is organized as follows: in Sec. 3.1, we briefly describe our model with reference to SBM. In Sec. 3.2, we extend the study of the dynamics of SBM in Eq. (1.11), begun in the previous chapter, from intermediate to strong coupling regimes, comparing our predictions with renowned theoretical approximations. In Sec. 3.3, we study the time-dependent protocol in the presence of dissipation and we discuss possible physical intepretations of our numerical results. Eventually, in 3.4 we discuss viable extensions of this work along with future perspectives.

3.1 MODEL HAMILTONIAN

Here we consider as a model Hamiltonian that of a TLS, i. e. a qubit, subject to time-dependent external fields and interacting with its surrounding, following the general form of Eq. (1.20). Similar to Chpt. 2, the time-dependent Hamiltonian $H_S(t)$ reads

$$H_S(t) = -\frac{1}{2}\boldsymbol{h}(t)\cdot\boldsymbol{\sigma}, \tag{3.1}$$

where we make use of the spin 1/2 Pauli matrices $\boldsymbol{\sigma} = (\sigma_x, \sigma_y, \sigma_z)$. We take as $\boldsymbol{h}$ a time-dependent magnetic field vector which at fixed time t points in a given direction of the three-dimensional coordinate space. We conventionally adopt as a basis for the qubit states, i. e. the computational basis, the set of eigenstates of σ_z operator, namely $\sigma_z|\hat{z};\pm\rangle = \pm|\hat{z};\pm\rangle$: as a consequence, the component of $\boldsymbol{h}$ along the $\hat{z}$ axis acts as a bias on the energy levels of the two states, while linear combinations of $\sigma_\pm$ operators give rise to tunnelling between these two states.

We model our bath as in Eq.(1.8), while for the time-independent interaction term coupling the qubit to the bath, we assume the following expression

$$H_I = \frac{1}{2}\boldsymbol{\sigma}\cdot\hat{\boldsymbol{n}}\sum_k \lambda_k(b_k^\dagger + b_k). \tag{3.2}$$

In Eq. (3.2), λ_k is the usual parameter describing the coupling with the k-th oscillator, while $\hat{n}$ is a general coupling direction in the Cartesian coordinate space.

Eq. (3.2) is rather general: it has been recently proposed to study the effect of a thermal environment on qubits subject to different time-dependent protocols, including the widely studied LMSZ sweeps [100, 129, 138]; in the latter case, it has been argued that the introduction of a "transverse" coupling direction, i. e. orthogonal to the time-dependent bias field, could provide a simple theoretical expla-

nation of the experimental findings regarding D-Wave Rainier's chip [98].

In the following we extend our analysis to a qubit coupled to a thermal bath along different spatial directions. As a first example, we turn back to SBM model, in order to simulate its behavior in the strong coupling regime. As a second example, we analyze a time-dependent protocol where the qubit is subject to a rotating magnetic field $\boldsymbol{h}(t)$ performing a sweep in a fixed plane, and the dissipation can take place along two particular directions in the plane of rotation.

3.2 SBM IN THE STRONG COUPLING REGIME

Taking a static tunnelling element along $\hat{x}$ axis, i. e. $h_x = \Delta$, the bias field along $\hat{z}$ axis, $h_z = h_0$, $h_y = 0$, and restricting to the case of Ohmic dissipation ($s = 1$), with $\hat{\boldsymbol{n}} = \hat{z}$, the interacting qubit-bath model with Eq. (3.1) and (3.2) reduces to the biased Ohmic SBM.

Following the same route as in Chpt. 2, we start by preparing the system and the bath at initial time t_o in a factorized state:

$$\rho(t_o) = \rho_S(t_o) \otimes \frac{e^{-\beta H_B}}{Z_B} \tag{3.3}$$

where $\rho_S(t)$ is the reduced density matrix of the qubit that can be computed by tracing out the bath degrees of freedom, i. e. $\rho_S(t) = \mathrm{tr}_B\, \rho(t)$. We choose $|\hat{z}; +\rangle$ as the initial state of the qubit, while the bath state is taken as the equilibrium state at $T = 0$. We model our bath with a collection of $M = 50$ bosonic modes, choosing the absolute maximum number of excitations up to $N_{ph} = 6$ (see Sec.2.1 for details) and we fix the cutoff frequency of the bath to $\omega_c = 5\Delta$.

3.2.1 The unbiased case

In the following, we restrict to the unbiased case ($h_0 = 0$). We simulate the dynamics of the system for different values of the coupling strength α, ranging from $1 \cdot 10^{-1}$ to $5 \cdot 10^{-1}$. In Fig. 3.1, we plot the qubit magnetization $\langle \sigma_z(t) \rangle$ as a function of the rescaled time $\Delta_r t$: we show that the magnetization dynamics experiences a crossover from a regime of underdamped oscillations in time to an incoherent regime where the oscillation frequency tends to vanish, as long as the coupling strength approaches the expected crossover value $\alpha = 0.50$.

The crossover from coherent to incoherent behavior can be interpreted in terms of the growth of the entanglement between the qubit and its bath [65], a mechanism which can be found in several bipartite systems [139]. Indeed, starting from the initial condition in Eq. (3.3), where the state of the system is factorized into a product of states of the two subsystem, the state of the qubit thermalizes towards the

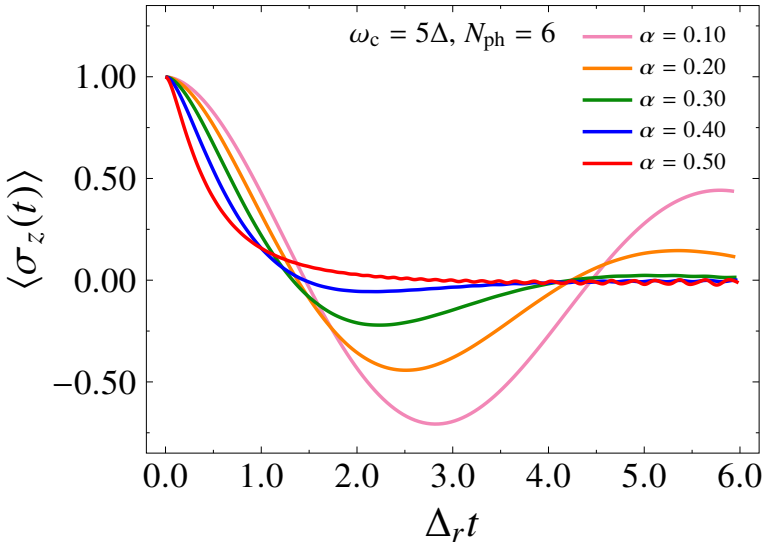

Figure 3.1: Magnetization $\langle \sigma_z(t) \rangle$ as a function of the rescaled time $\Delta_r t$, in the case of Ohmic bath ($s = 1$), $T = 0$, $h_0 = 0$, for different values of the coupling strengths α in the range $1 \cdot 10^{-1}$ to $5 \cdot 10^{-1}$. The number of bath modes is $M = 50$, the cutoff frequency $\omega_c = 5\Delta$ and the maximum number of excitations is $N_{ph} = 6$.

equilibrium state of the whole interacting Hamiltonian in Eq. (1.20) at $T = 0$, showing entanglement with the bath degrees of freedom. Each numerical curve reported in Fig. 3.1 describes the correct dissipative behavior of the qubit, as it can be shown by a direct comparison with the theoretical results for the quality factor as a function of the coupling strength α, reported in Fig. 3.2b. Our results are also in good agreement with recent findings obtained through novel numerical approaches based on non-perturbative stochastic techniques [76]. A detailed comparison with the analytical prediction in the case $\alpha = 1/2$ (see Eq. (1.41)), reported in Fig. 3.2a, shows also good agreement with theory at long times, while at shorter times small deviations start to appear. These discrepancies can be due the small value of the frequency cutoff chosen $\omega_c = 5\Delta$, which cannot meet the parameters conditions ensuring the validity of Eq. (1.41); we argue that this limit is also responsible for the residual coherent behavior of the magnetization at $\alpha = 1/2$ observed in Fig. 3.1 for long times. A similar analysis of the magnetization dynamics can be performed in the biased case, considering both the well-known limits of weak coupling and Toulouse point: we shift the discussion to the subsquent section.

Additional insights on the dynamics of SBM can be derived from the analysis of the expectation values of the difference of number operators from their initial equilibrium values, i.e. $\langle \Delta n_k(t) \rangle = \langle n_k(t) \rangle - n_k^o$, computed for each bosonic mode at fixed time intervals in the range $[t_o, t_f]$, as shown in Fig. 3.3a; it can be inferred that at short times the bath response extends over the whole frequency spectrum, high-

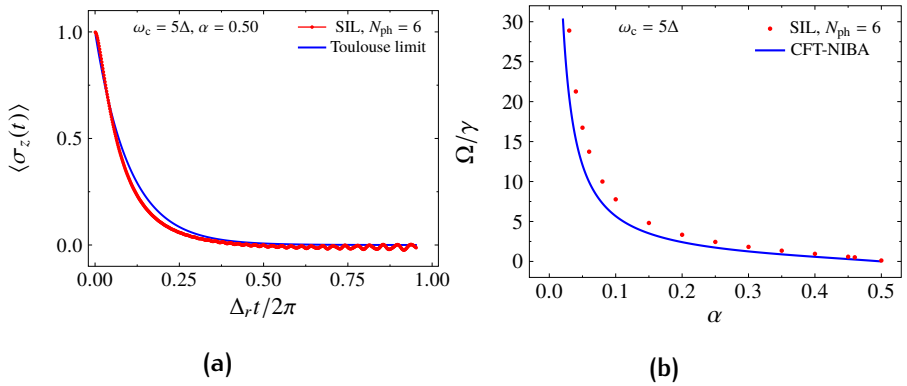

Figure 3.2: Panel a: Magnetization $\langle \sigma_z(t) \rangle$ as a function of the rescaled time, computed at the Toulouse point ($\alpha = 1/2$), for $h_0 = 0$ (unbiased case), at $T = 0$; we plot of the numerical SIL result (red curve), compared with the theoretical curve in Eq. (1.41) (solid blue curve), which is valid in the limit $\omega_c \to \infty$. As in the main text, $M = 50$, $\omega_c = 5\Delta$, $N_{ph} = 6$. Panel b: Plot of the quality factor Q against the coupling strength α at $T = 0$: numerical estimates derived from a fit of the simulated curves shown in Fig. 3.1 (red points), compared with the theoretical result in Eq. (2.12) known from CFT and NIBA predictions (blue curve).

frequency modes showing slightly greater occupation than the slower ones, even if the occupation is quite small. At intermediate times, a set of peaks start to come into play, due to multiple scattering processes of the qubit with the bath modes. Hence, the bath response shows a first order peak which signals the onset of a resonant behavior, its position shifting towards lower frequencies with increasing time. As expected, the behavior of each curve at intermediate times, as well as at longer times shows a clear dependence on the value of the coupling strength α. In Fig. 3.3b, we plot $\langle \Delta n_k(t) \rangle$, computed at sufficiently long time t_{sat} for different coupling strengths α: the results show that the position of the first-order peak shifts towards lower energies for increasing coupling strengths, and the characteristic energy of the system is proportional to the effective tunnelling energy Δ_{eff}. Moreover, the curves of bosonic excitations exhibit oscillations in ω_k/ω_c that tend to disappear as the coupling strength approaches the crossover value: this effect can be seen as a consequence of the increasingly incoherent behavior of the system. These features confirm that, for coupling strengths in the range $0 \leq \alpha \leq 0.5$ the dynamical evolution of the whole system reaches an equilibrium state that can be interpreted in terms of a single qubit whose tunnelling energy is renormalized proportionally to Δ_r, experiencing incoherent tunnelling between localized states.

The exchanged energy with the bath can also be studied for different values of the coupling strengths α: from Fig. 3.4, it can be shown that all the curves tend to a saturation value, which in our simulation is

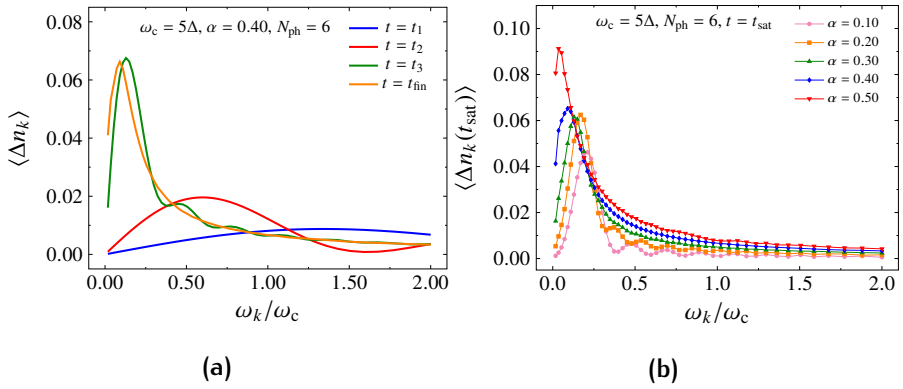

Figure 3.3: Panel a: Expectation values of $\Delta n_k(t)$ computed for each bath mode k at different times $\{t_1, t_2, t_3, t_f\} = \{0.03, 0.06, 1.14, 6.00\}$ (in units of Δ_r^{-1}), for fixed coupling strength $\alpha = 0.40$, $\omega_c = 5\Delta$, $T = 0$, $h_0 = 0$, $M = 50$ and $N_{ph} = 6$. Panel b: Expectation values of $\langle \Delta n_k \rangle$ computed for each bath mode k at rescaled time $t_{sat} = 4.85$ (in units of Δ_r^{-1}), for different coupling strengths α in the range $1 \cdot 10^{-1}$ to $4 \cdot 10^{-1}$, $\omega_c = 5\Delta$, $T = 0$, $h_0 = 0$, $M = 50$ and $N_{ph} = 6$.

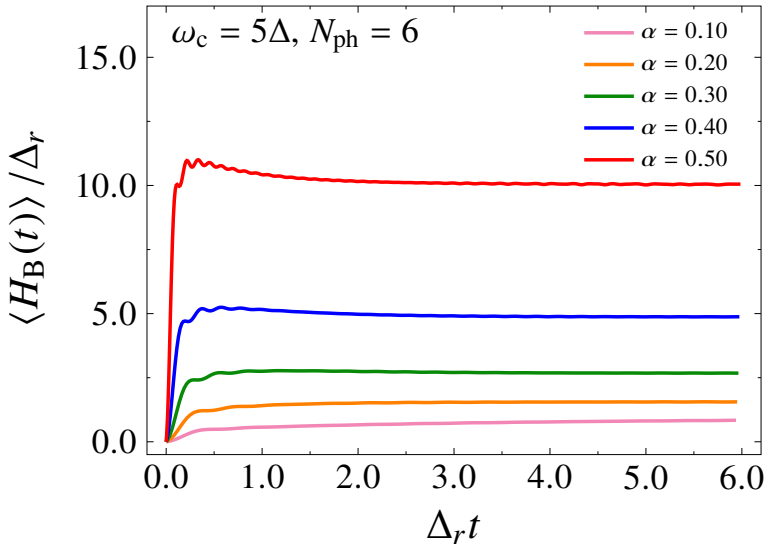

Figure 3.4: Expectation values of $\langle H_B(t) \rangle$ (in units of Δ_r) computed as a function of the rescaled time $\Delta_r t$, for different coupling strengths α in the range $1 \cdot 10^{-1}$ to $5 \cdot 10^{-1}$, $\omega_c = 5\Delta$, $T = 0$, $h_0 = 0$, $M = 50$ and $N_{ph} = 6$.

fixed by the energy conservation: as shown in [108], at every time t the energy of the non-equilibrium initial state of the qubit is equal to the sum of the expectation values of the different operators in Eq. (1.20). It can also be noticed that the saturation value of $\langle H_B(t) \rangle$ strongly depends on the coupling strength α. Moreover, for increasing coupling strengths, it can be observed that the bath energy exhibits an oscillatory behavior at short times, and a moderately prononunced

peak which tends to be greater than its long-time value. This feature is due to the increasing importance of the qubit-bath correlations which, in the strong coupling regime, can modify the mechanism of energy exchange.

3.2.2 The biased case from weak to strong coupling

Below, we report a comparison of our numerical results for the dynamics of the qubit magnetization in the biased SBM ($h_0 \neq 0$), with analytical curves derived by means of a first order expansion in the model parameters reported in [90]. In the limit of weak coupling regime ($\alpha \ll 1$), and taking $T = 0$, the qubit magnetizations along $\hat{x}$, $\hat{z}$ axes read

$$\begin{aligned} \langle \sigma_z(t) \rangle &= \frac{h_0}{\Omega}(1 - e^{-\gamma_r t}) + \frac{h_0^2}{\Omega^2} e^{-\gamma_r t} + \frac{\Delta_r^2}{\Omega^2} \cos(\Omega t) e^{-\tilde{\gamma}_r t} \\ \langle \sigma_x(t) \rangle &= \frac{\Delta_r^2}{\Delta\Omega}(1 - e^{-\gamma_r t}) + \frac{h_0 \Delta_r^2}{\Delta\Omega^2}(e^{-\gamma_r t} - \cos(\Omega t) e^{-\tilde{\gamma}_r t}) \end{aligned} \tag{3.4}$$

where $\Omega = \sqrt{\Delta_r^2 + h_0^2}$, and the damping rates are $\gamma_r = \pi \alpha \Delta_r^2 / \Omega$, $\tilde{\gamma}_r = \gamma_r / 2$.

For non-zero temperatures T of the reservoir, these results slightly change [90]. Eq. (3.4) include the quantum non-Markovian effects due to the interaction of the qubit with the bath. In Fig. 3.5, we compare numerical SIL results with analytical curves in Eq. (3.4), having fixed the bias field $h_0 = 0.5\Delta$ and the coupling strength $\alpha = 1 \cdot 10^{-3}$. As expected, SIL results show an excellent agreement with the curves in Eq.(3.4). It could be shown that small quantitative differences may appear as we compare the numerical results for the energy exchanged with the reservoir with the analytical expression reported in [90]. However, by means of our technique the qualitative features of the energy exchange, from intermediate to long times, can be correctly described, and we argue that the observed differences are mainly due to the choice of the small cutoff frequency ω_c.

Moving to stronger coupling strength α, we compare our numerical findings for the SBM with analytical prediction in (1.41). As it is evident from Fig. 3.6, while the numerical curve correctly describe the qualitative behavior of the function in Eq. (1.41), which is strictly valid for $\omega_c \to \infty$ as leading order, several quantitative differences can be observed, e. g. the long-time value of $\langle \sigma_z(t) \rangle$ slightly differs from that expected from Eq. (1.41) at $T = 0$, i. e. $\langle \sigma_z(\infty) \rangle = \frac{2}{\pi} \arctan\left(\frac{4 h_0 \omega_c}{\pi \Delta^2}\right)$. As anticipated in the previous section, these results are mainly due to the small value of the frequency cutoff ω_c chosen: we expect these small numerical differences to vanish with increasing the frequency cutoff, as well as the number of the bath oscillators M.

However, it should be noted that from Sec.2.1, as the dimension of the truncated Hilbert space considered rapidly grows with the

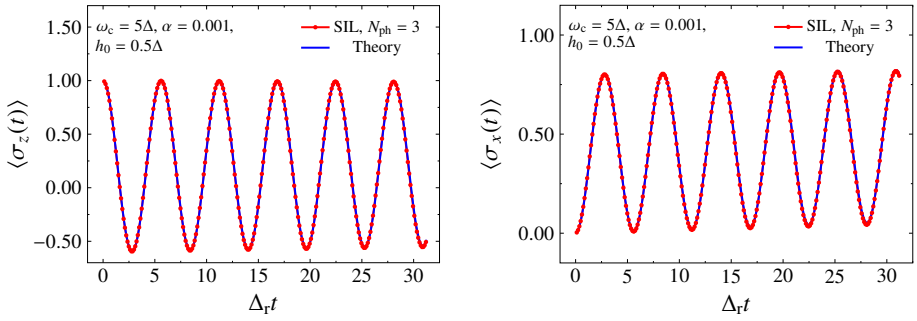

Figure 3.5: Plot of $\langle\sigma_x(t)\rangle$ as a function of time t for the biased SBM, having fixed $\omega_c = 5\Delta$, $\alpha = 0.001$, $h_0 = 0.5\Delta$, $T = 0$ and $N_{ph} = 3$. SIL results (red points) compared with theoretical curve from Eq. (3.4) (solid blue curve).

absolute maximum number of excitations N_{ph} and the number of modes M, the inclusion of additional modes in the strong coupling regime can become prohibitively costly. These findings point towards the need for an optimized basis of states for the implementation of SIL method, which could hopefully reduce its computational cost.

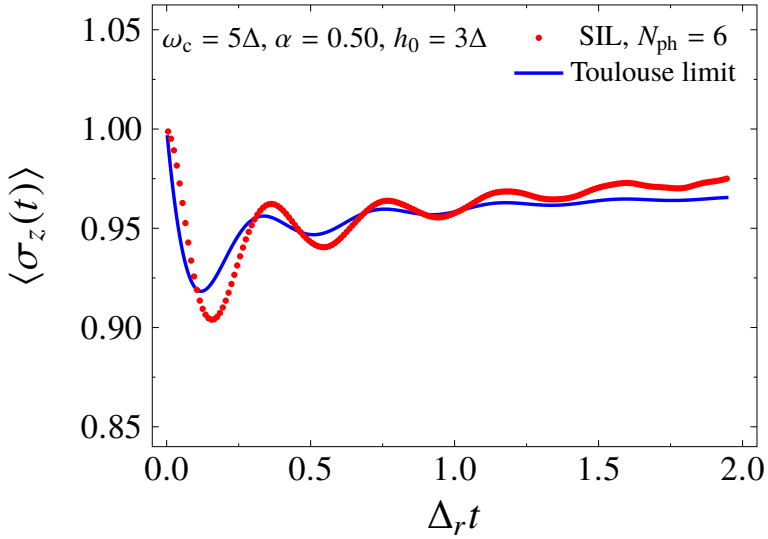

Figure 3.6: Magnetization $\langle\sigma_z(t)\rangle$ as a function of the rescaled time, computed at the Toulouse point ($\alpha = 1/2$), with fixed bias $h_0 = 3\Delta$, and $T = 0$; we plot the numerical SIL result (red points), compared with the theoretical curve in Eq. (1.41) (solid blue curve). As in the main text, $M = 50$, $\omega_c = 5\Delta$,$N_{ph} = 6$.

3.3 TIME DEPENDENT PROTOCOL

In this section, we study the effect of decoherence and dissipation on a two level system subject to a rotating magnetic field. We take the qubit Hamiltonian as in Eq. (3.1), where h is the magnitude of the applied magnetic field; we adopt a system of polar coordinates (θ, ϕ), i. e. $\boldsymbol{h} = (h\sin\theta\cos\phi, h\sin\theta\sin\phi, h\cos\theta)$. We also introduce an additional static magnetic field along the positive $\hat{z}$ direction, i. e. $h_0\hat{z}$. We restrict the rotating magnetic field $\boldsymbol{h}$ in the $\hat{x}$-$\hat{z}$ plane by fixing $\phi = 0$. The qubit Hamiltonian thus reads

$$H_S(t) = -\frac{1}{2}(h_0 + h\cos\theta(t))\sigma_z - \frac{h}{2}\sin\theta(t)\sigma_x \tag{3.5}$$

The magnetic field $\boldsymbol{h}$ evolves performing a sweep in $\hat{x}$-$\hat{z}$ plane in a total time t_f, i. e. the polar angle changes according to $\theta(t) = \pi(t - t_0)/t_f$, from $\theta(t_0) = 0$ to $\theta(t_f) = \pi(1 - t_0/t_f)$.

This protocol, widely studied in the field of Nuclear Magnetic Resonance (NMR), has regained attention following recent theoretical and experimental works [136, 137]. It has been shown that physical implementations of Hamiltonians of the form of Eq. (3.5) can be achieved with high level of control employing superconducting circuits; moreover, a simple mapping exists from Eq. (3.5) to the Haldane model at half filling on a honeycomb lattice [140], which is a prototypical model of a Chern insulator. Following this mapping, every qubit state

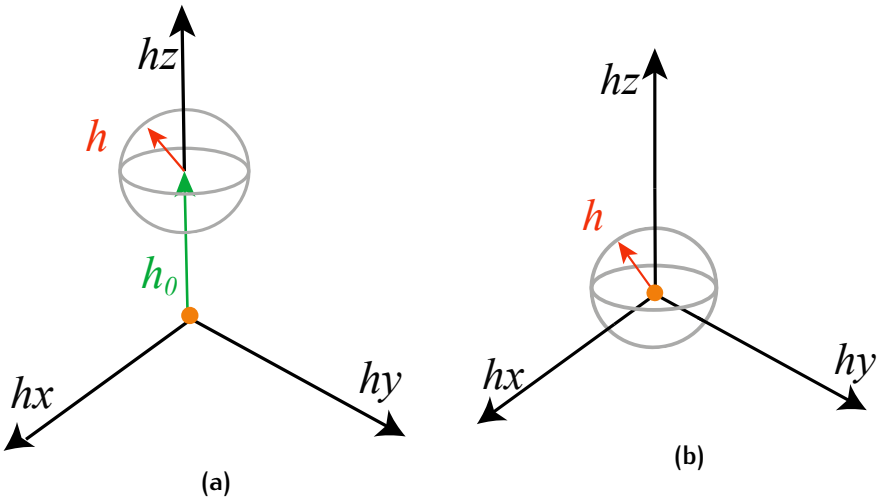

Figure 3.7: Picture of two characteristic field configurations $h_0, h(t)$. In panel a, $h_0 > h$ so that during the sweep of the magnetic field $\boldsymbol{h}$ along the fixed circle no degeneracy of the energy levels is present, i. e. the integral of the Berry curvature over the sphere gives always zero, as the monopole (orange dot) is outside the sphere. In panel b, the situation is reversed, and the qubit can simulate the topological phase of the Haldane model.

on the Bloch sphere at fixed coordinates (θ, ϕ) can be mapped onto

a single quasi-momentum state (k_x, k_y) around the high-symmetry points of the first Brillouin zone of the honeycomb lattice. As a consequence, it allows for a dynamical measurement of the topological properties of the Haldane model by making use of a superconducting qubit, e. g. the first Chern number can be probed. It follows that, by tuning the ratio of the field amplitudes h_o/h and performing quantum state tomography at different times t during the sweep, topological transitions can be measured with high level of accuracy.

In the following, we analyze the dissipative dynamics of a qubit described by Eq. (3.5) at weak and strong coupling strengths, both for long and short sweep times t_f as compared with the time scale $1/h$, i. e. we consider both adiabatic and anti-adiabatic regimes. The qubit is coupled to the environment along a direction which lies in the plane of rotation of the magnetic field, and we focus on the two particular cases $\hat{\boldsymbol{n}} = \hat{z}, \hat{x}$. We compute the excess energy of the qubit at the end of the sweep, i. e. the difference between the mean value of the reduced system energy and the ground state energy $\varepsilon_{gs}(t_f)$ of the non-interacting qubit Hamiltonian in Eq. (3.5), computed at final time t_f

$$\varepsilon_{res} = \mathrm{Tr}[\rho(t_f) H_S(t_f)] - \varepsilon_{gs}(t_f) \tag{3.6}$$

Due to the simple form of Eq. (3.5), the excess energy can also be linked to the fidelity $\mathcal{F}(t_f)$ at the end of the sweep

$$\varepsilon_{res} = |h - h_o|(1 - \mathcal{F}(t_f)) \tag{3.7}$$

where $\mathcal{F}(t_f) = \langle \psi_{gs}(t_f)| \rho_S(t_f) |\psi_{gs}(t_f)\rangle$ and $|\psi_{gs}(t_f)\rangle$ is the ground state of qubit Hamiltonian in Eq. (3.5) at $t = t_f$. In addition, we compute the expectation values of qubit operators as functions of time $\langle \boldsymbol{\sigma} \rangle = (\langle \sigma_x(t) \rangle, \langle \sigma_y(t) \rangle, \langle \sigma_z(t) \rangle)$, i. e. the dynamical evolution of the Bloch vector, at fixed final times t_f and for different values of the coupling strength.

We first consider the qubit system in the absence of dissipation, taking the static bias field $h_o = 0$: at initial time $t_0 = 0$, the magnetic field is aligned along the positive $\hat{z}$ direction and the qubit is prepared in its ground state, i. e. $|\psi(t_o)\rangle = |\hat{z}, +\rangle$. For $t > 0$, the field $\boldsymbol{h}$ rotates around the $\hat{y}$ axis. The qubit dynamics can be straightforwardly solved in the counter-rotating frame around the $\hat{y}$ axis (see App. b): due to its simple form, the Hamiltonian in Eq. (3.5) in the rotating frame is time-independent, and it follows that the excess energy of the closed system reads

$$\varepsilon_{res} = \frac{h\dot{\theta}^2}{2} \frac{1 - \cos\left(\pi \sqrt{h^2 + \dot{\theta}^2}/\dot{\theta}\right)}{h^2 + \dot{\theta}^2} \tag{3.8}$$

where we put for brevity $\dot{\theta} = \pi/t_f$. The qubit dynamics is described by a cycloid on the Bloch sphere, i. e. the Bloch vector periodically points out of the $\hat{x}$-$\hat{z}$ plane. This trajectory is due to the oscillations in time of the magnetization along the $\hat{y}$ axis: therefore, $\langle \sigma_y(t) \rangle$ can

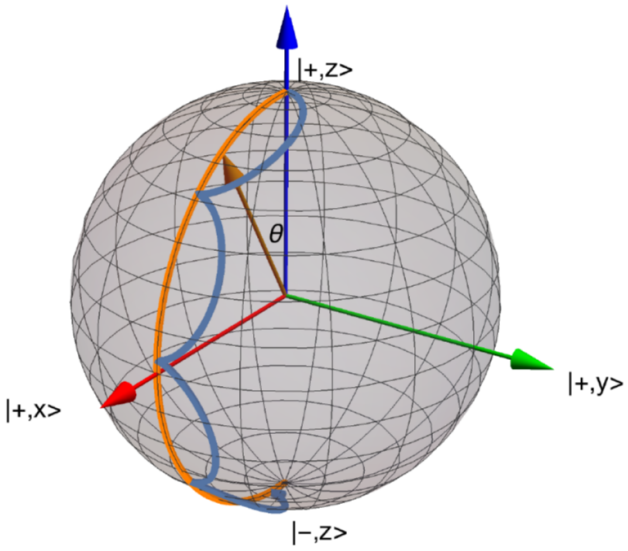

Figure 3.8: Bloch-sphere pictorial representation of the evolution of the TLS during the sweep of the magnetic field from the north ($\theta = 0$) to the south pole ($\theta = \pi$). The orange line follows the adiabatic path, while the finite-t_f path is a cycloid (blue solid line).

serve as a measure of deviation from the adiabatic path, which is a circle in the $\hat{x}$-$\hat{z}$ plane. The non-adiabatic response of the Bloch vector is thus proportional to $\langle \sigma_y(t) \rangle$ [136]; furthermore, using perturbation theory it has been shown that at first order in $\dot{\theta}/h$ the non-adiabatic response can be linked to the curvature of the ground state manifold of the Hamiltonian in Eq. (3.5), i. e. to the Berry phase of the qubit. As a consequence, the measure of $\langle \sigma_y(t) \rangle$ at each time t allows to achieve the fidelity at final time t_f that, in the quasi-adiabatic limit, can be used to compute the first Chern number of the system [137]. The deviation from the adiabatic path can also be seen from the excess energy in Eq. (3.8), which is plotted in Fig. 3.9 (black curve): notice that it exhibits several maxima corresponding to different final times t_f owing to the fact that, in the non-adiabatic regime, the qubit dynamics cannot follow the evolution of the externally driven magnetic field, and the state vector of the qubit at the end of the sweep differs from the corresponding ground state. However, the amplitude of these maxima is decreasing as long as the time t_f is increased, i. e. the dynamics can be considered truly adiabatic only in the limit $t_\mathrm{f} \gg 1/h$.

This scenario undergoes several changes if the interaction with the external bath is considered.

3.3.1 Coupling along z direction

We first analyze the case of interaction along $\hat{z}$ axis. In Fig. 3.9, we plot the excess energy curve of the qubit interacting with a bath at

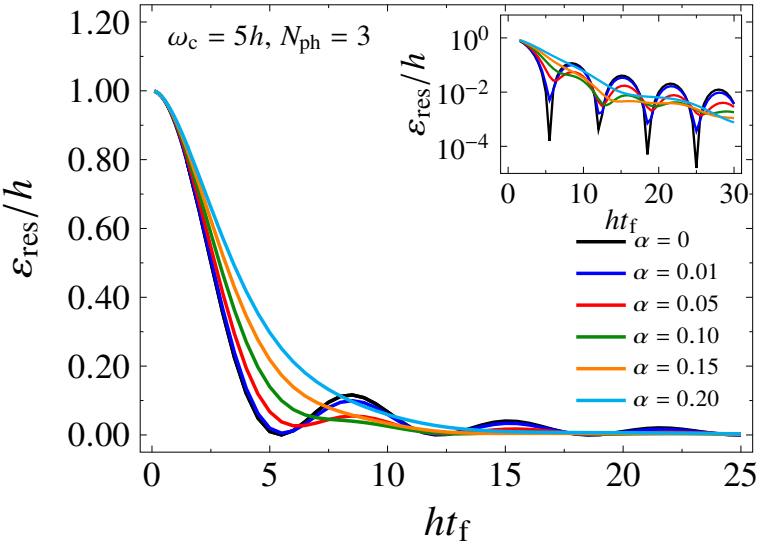

Figure 3.9: Excess energy plotted as a function of the final time t_f (in units of h^{-1}), for different coupling strengths ranging from $1 \cdot 10^{-2}$ to $2 \cdot 10^{-1}$, in the case $\hat{\boldsymbol{n}} = \hat{z}$. The number of modes has been fixed to $M = 80$, the cutoff frequency $\omega_c = 5h$, $N_{ph} = 3$ and $T = 0$. Inset: semi-logarithmic plot of the same curves as in the main plot.

$T = 0$, for different values of the coupling strength α ranging from 0 to $2 \cdot 10^{-1}$. As it can be noticed, the interaction with the external bath acts to reduce the coherence of the system dynamics. The effect of decoherence results in a smoothing of the excess energy curve with respect to the closed case. However, the difference between the closed and the open system curve depends on the final time t_f: at short final times t_f, the interaction with the environment generally leads to an increase of the excess energy, resulting in a non-adiabatic behavior of qubit dynamics; conversely, at intermediate times t_f, the effect of the bath can lead to a decrease of the local maxima of the excess energy as compared with the closed case, i. e. the state of the qubit at $\theta(t_f)$ is closer to the corresponding state on the adiabatic path. It follows that, at weak coupling regime the effect of friction counteracts the non-adiabaticity of the system induced by the fast external drive, thus resulting in a reduction of the excess energy. This scenario changes in the intermediate coupling regime: for coupling strengths $\alpha > 0.1$, it can be noticed that the excess energy starts to increase, and the system definitely misses the adiabatic path. The resulting non-monotonic behavior of the excess energy can be clearly observed for final times t_f where the closed system curve shows secondary maxima of excitation, while for values of t_f corresponding to minima the interaction with the bath leads to monotonic non-adiabaticity. It should also be noticed that, as depicted in the inset of Fig. 3.9, for very slow sweeps the open system curves at weak coupling strengths tend to coincide, and

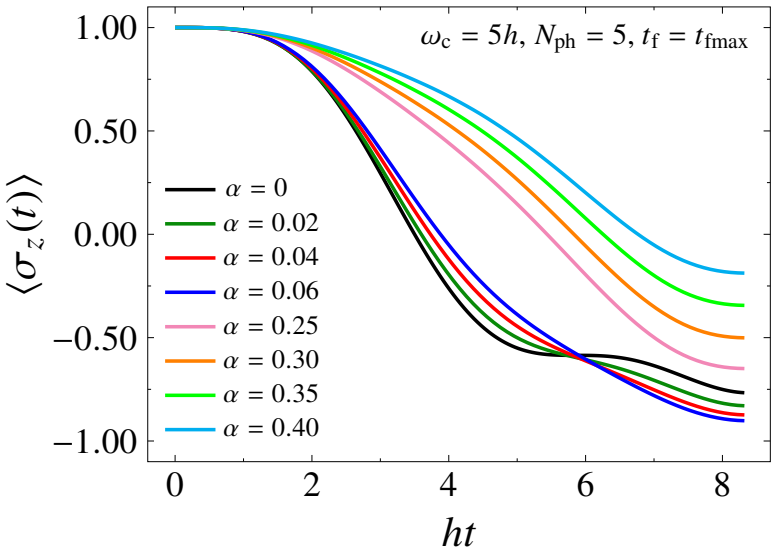

Figure 3.10: Plot of $\langle \sigma_z(t) \rangle$ as a function of time t for the protocol in Eq. (3.5), with fixed final time $t_f = t_{fmax} = 8.42/h$. The qubit couples to an Ohmic bath ($s = 1$) along $\hat{\boldsymbol{n}} = \hat{z}$, for different coupling strengths ranging from 0 to $4 \cdot 10^{-1}$. The number of modes has been fixed to $M = 70$, the cutoff frequency $\omega_c = 5h$, $N_{ph} = 5$ and $T = 0$.

they are consistent with the closed system result. Interestingly, the monotonic non-adiabaticity at strong coupling regime was recently observed in [45], where the dynamical behavior of the Chern number in a dissipative environment was studied and a description of the bath-induced non-adiabaticity was achieved using non-perturbative Stochastic Schrödinger equation.

Further information on the dynamics of the open system at intermediate final times t_f can be derived from the analysis of the expectation values $\langle \sigma_x(t) \rangle$, $\langle \sigma_y(t) \rangle$, $\langle \sigma_z(t) \rangle$: in Figures 3.10, 3.11 and 3.12, we plot the expectation values of the spin operators as a function of time t, from weak to strong coupling regime and for fixed final time $t_f = t_{fmax} = 8.42/h$, corresponding to the first second-order maximum of Eq. (3.8). It can be noticed that, following the Heisenberg equations which link the time derivative of $\langle \sigma_z(t) \rangle$ to $\langle \sigma_y(t) \rangle$, the decrease in the excess energy occurring for $t_f = t_{fmax} = 8.42/h$ observed at weak coupling can be traced back to the progressive change of $\langle \sigma_y(t) \rangle$. Hence, for increasing coupling strengths α it can be noticed that the magnetization along $\hat{y}$ loses the oscillatory behavior with frequency $\sqrt{\dot{\theta}^2 + h^2}$ (see App. b), which is a characteristic feature of dynamics in the absence of dissipation: actually, as it can be inferred from Fig. 3.11 the second local minimum turns into a local maximum, its position drifts towards higher times t, causing the inflection point of $\langle \sigma_z(t) \rangle$ in Fig. 3.10 to change accordingly; eventually, at the end of the sweep the magnetization along $\hat{z}$ tends to the adiabatic value, and the state of the

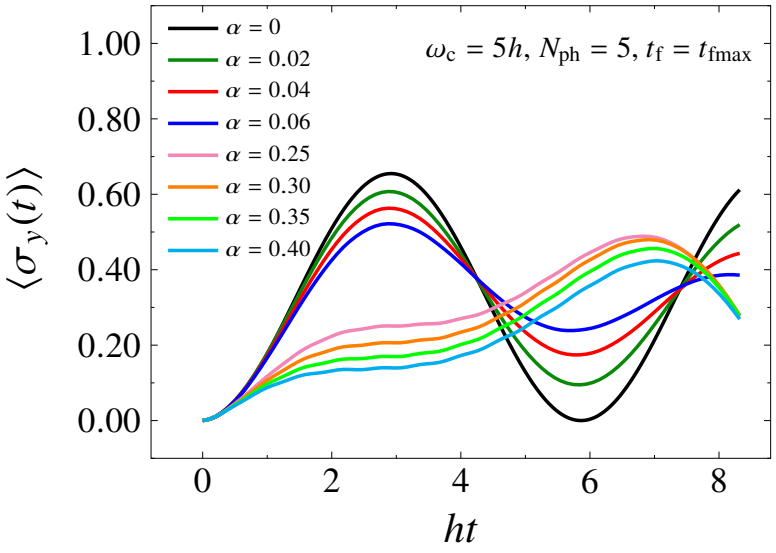

Figure 3.11: Plot of $\langle \sigma_y(t) \rangle$ as a function of time t for the protocol in Eq. (3.5), with fixed final time $t_f = t_{fmax} = 8.42/h$. The qubit couples to an Ohmic bath ($s = 1$) along $\hat{\boldsymbol{n}} = \hat{z}$, for different coupling strengths ranging from 0 to $4 \cdot 10^{-1}$. The number of modes has been fixed to $M = 70$, the cutoff frequency $\omega_c = 5h$, $N_{ph} = 5$ and $T = 0$.

qubit in the open dynamics at final time t_f is closer to the ground state $|\psi_{gs}(t_f)\rangle$. While the previous description holds true also when the closed-system excess energy in Eq. (3.8) shows local minimum values, e. g. $t_f = t_{fmin} = 12.7/h$, it can be observed that at weak coupling strengths the interaction with the bath cannot noticeably change the excess energy.

More information on the physics at strong coupling regime can be drawn: as shown in Fig. 3.10, for $\alpha > 0.10$ $\langle \sigma_z(t_f) \rangle$ starts to increase. This behavior clearly depends on the final time t_f, i. e. on the slope of the external drive: for faster sweeps, the non-adiabatic behavior due to the interaction with the environment occurs at lower coupling strengths as compared to slower evolutions; as a consequence, the coupling strength directly influences the adiabaticity condition. This feature can be inferred from Fig. 3.13, where we plot the behavior of fidelity $\mathcal{F}(t_f)$ at the end of the sweep, computed for two different fixed final times $t_f = \{ t_{fmax}, t_{fmin} \} = \{ 8.42/h, 12.17/h \}$, corresponding to the first second-order maximum and the second minimum of Eq. (3.8) (see Fig. 3.9, black curve), for different coupling strengths α taken in the range $1.0 \cdot 10^{-1}$ to $4.5 \cdot 10^{-1}$. At final time $t_f = t_{fmax}$, where the closed system excess energy exhibits a local maximum, fidelity shows a small non-monotonic behavior, due to the previously described effect; conversely, at $t_f = t_{fmin}$ a flat behavior at weak coupling, followed by monotonic decrease occurring at higher values of α can be observed.

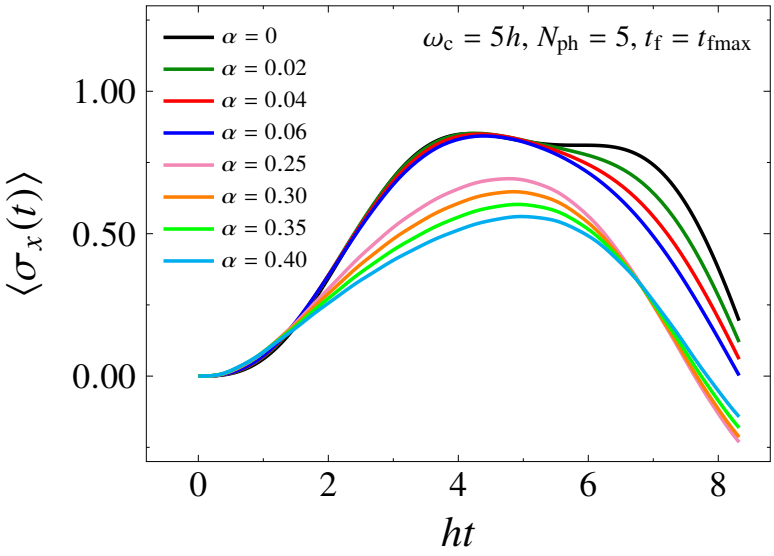

Figure 3.12: Plot of $\langle \sigma_x(t) \rangle$ as a function of time t for the protocol in Eq. (3.5), with fixed final time $t_f = t_{fmax} = 8.42/h$. The qubit couples to an Ohmic bath ($s = 1$) along $\hat{\boldsymbol{n}} = \hat{z}$, for different coupling strengths ranging from 0 to $4 \cdot 10^{-1}$. The number of modes has been fixed to $M = 70$, the cutoff frequency $\omega_c = 5h$, $N_{ph} = 5$ and $T = 0$.

As shown in [45], an adiabaticity criterion for the protocol in Eq. (3.5) has been proposed which links the velocity of the sweep $\dot{\theta}$ to the renormalized field Δ_r along $\hat{x}$ direction (with $\Delta = h$), i. e. $\dot{\theta} \ll \Delta_r$, provided that $\dot{\theta} \ll h$. Further, for fixed values of $\dot{\theta}$ well below h, at strong coupling a crossover from quasi-adiabatic to non-adiabatic behavior occurs at $\dot{\theta} \simeq \Delta_r$. We find that our numerical results at strong coupling generally agree with this scenario, while in the weak coupling regime several intervals of final times t_f exist where the bath can act to improve the adiabaticity. It follows that, at weak coupling strengths the dynamical measure of the topological properties shows robustness to the external noise.

3.3.2 Coupling along x

Qualitatively different results can be found if the qubit couples with the bath along $\hat{x}$ axis. Here we restrict to weak coupling regime and simulate the dissipative dynamics at $T = 0$ of the time-dependent protocol in Eq. (3.5) with $\hat{\boldsymbol{n}} = \hat{x}$ and $h_o = 0$. In Fig. 3.14, we plot the excess energy as a function of the final time t_f for different coupling strengths, taken in the same range as in Fig. 3.9.

It can be shown that, for very fast sweeps the excess energy can be lower than the closed system result: the actual numerical results at short final times t_f depend on the coupling strength α at fixed cutoff

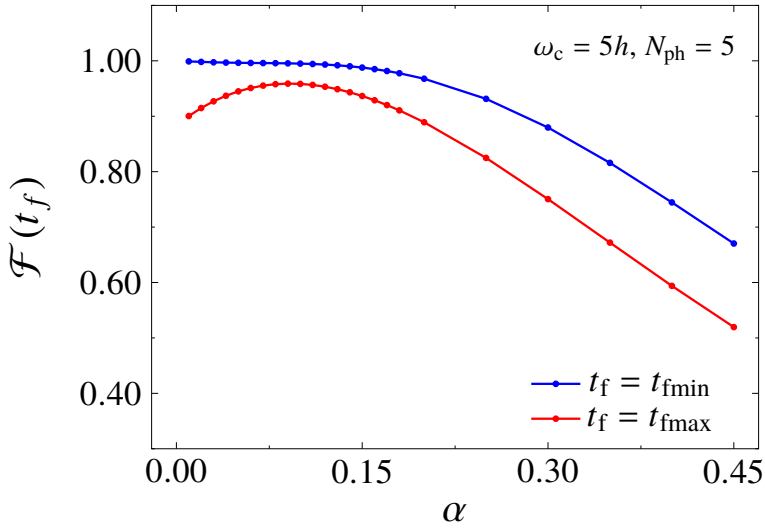

Figure 3.13: Fidelity at final time t_f $\mathcal{F}(t_f)$, plotted against the coupling strength α in the range $1.0 \cdot 10^{-2}$ to $4.5 \cdot 10^{-1}$, for two fixed final times $t_f = \{ t_{fmax}, t_{fmin} \} = \{ 8.42/h, 12.17/h \}$ corresponding to the first second order maximum and the second minimum of Eq. (3.8). The number of modes has been fixed to $M = 70$, the cutoff frequency $\omega_c = 5h$, $N_{ph} = 5$ and $T = 0$.

frequency ω_c. As shown in Fig. 3.15, by increasing the cutoff frequency ω_c, the short final time limit of the excess energy curve decreases, as a result of the reduced reaction time of the bath. However, the choice of different cutoff frequencies ω_c does not qualitatively change the physics at long times t_f. The decrease in the excess energy at short t_f is due to the peculiar form of the coupling to the external environment, which causes the qubit to flip at a fixed rate proportional to the coupling strength. This effect can provide a slight advantage to the success of the protocol, as long as the final time t_f is sufficiently short. However, for longer final times t_f the open system excess energy tends to be greater than the closed curve: this effect leads to an increasingly non-adiabatic dynamics, even at weak coupling strengths, as opposed to the case studied in 3.3.1 where, as long as the closed system dynamics is quasi-adiabatic, the dynamics is unaffected by the environment. This result shows several analogies with a recent study of the finite-time LMSZ protocol [141], showing that the effect of a transverse coupling to the bath at long final times t_f can lead to a fidelity $\mathcal{F}(t_f)$ lower than 1, as opposed to the exact result proposed in [96]. In addition, here the effect of time-periodic driving can be clearly observed, noticing the persistence of a structure made of several secondary maxima in the excess energy. These findings point towards an increasingly non-adiabatic behavior due to the bath, as long as the coupling strengths increases, occurring at intermediate up to long final times t_f.

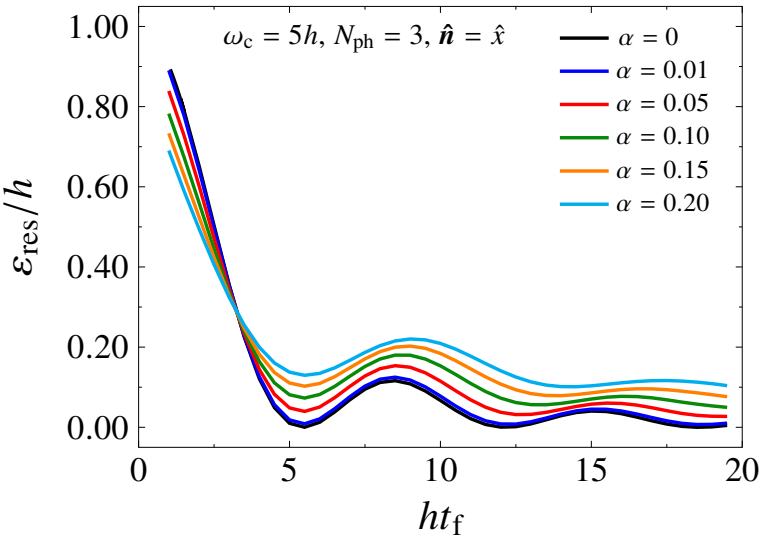

Figure 3.14: Excess energy plotted as a function of the final time t_f (in units of h^{-1}), for different coupling strengths α ranging from $1 \cdot 10^{-2}$ to $2 \cdot 10^{-1}$, in the case of $\hat{\boldsymbol{n}} = \hat{x}$. The number of modes has been fixed to $M = 80$, the cutoff frequency $\omega_c = 5h$, $N_{ph} = 3$ and $T = 0$.

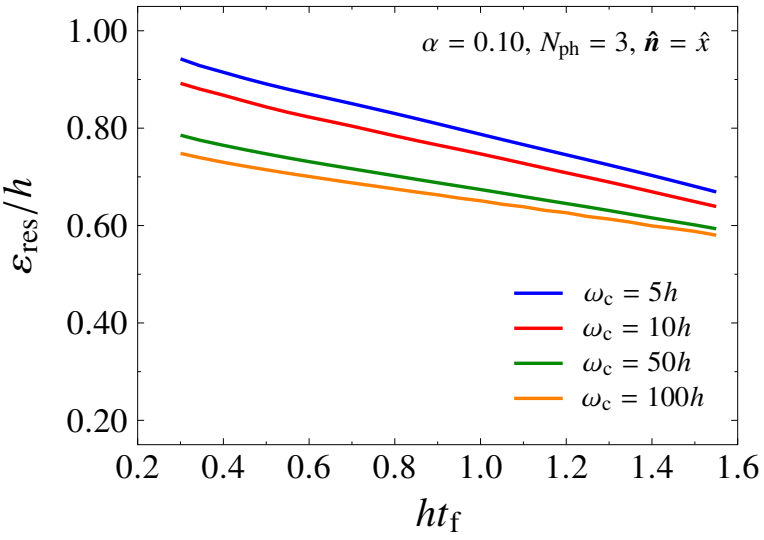

Figure 3.15: Excess energy plotted as a function of the final time t_f chosen in the range 0.2 to 1.5 (in units of h^{-1}), for fixed $\alpha = 0.10$, $M = 80$, $N_{ph} = 3$, $T = 0$ and different cutoff frequencies ω_c.

3.4 CONCLUSIONS

In this work, we studied the dynamics of a qubit in contact with its environment, subject both to static and driven external fields, from weak to strong coupling strengths, using the SIL approach. We showed that our method can provide a good description of the physics of the

SBM as a function of the coupling strength up to Toulouse point, where a crossover from coherent to incoherent behavior of the qubit magnetization takes place. We provided additional insights on the dynamics of the bath degrees of freedom, showing the changes in the bath response as a function of time. Moreover, we studied a protocol of a driven qubit subject to a time-periodic driving, with dissipation taking place along different directions. We showed that in the case of coupling along $\hat{z}$, if the dissipation strength is sufficiently weak, the influence of the bath can counteract the non-adiabaticity of the closed system evolution, leading to a non-monotonic behavior of the fidelity as a function of the coupling strength at fixed values of the final times. Conversely, at strong coupling bath-induced non adiabaticity [45] takes place, hindering the success of the protocol. This scenario changes if the coupling along $\hat{x}$ axis is considered: a measurable advantage over the closed system dynamics can be observed only for very fast sweeps, while for longer sweep durations we predict an increasingly non-adiabatic behavior, i. e. the excess energy tends to increase at increasing coupling strength. In the near future, we plan to extend our analysis to recently proposed time-dependent protocols implementing counter-diabatic driving [142, 143], in order to investigate the influence of the environment on the final success probability of these protocols in a broad range of coupling regimes. In addition, energy exchanges between systems of externally driven interacting qubits and the bath will also be analyzed, as well as prototypical models of quantum heat engines.

4 A NON-LINEARLY DRIVEN WORK TO WORK CONVERTER

In this chapter we present part of our original contributions to be submitted for publication.

Energy conversion at the microscopic scale poses great experimental and theoretical challenges. In the classical context, stochastic cyclic heat engines [144] are among the prototypical systems of interest [145, 146]. Here a single optically-trapped, micrometre-sized particle subject to periodically-driven forces and put in contact with two thermal reservoirs acts as working medium. In this context, the experimental realization of Brownian Carnot cycles has been recently achieved [147].

As the driving forces vary over timescales smaller than the thermal relaxation time, in these engines the thermal fluctuations arising from fluctuating forces cannot be neglected; as a consequence, the concepts of classical thermodynamics, i. e. heat, work and entropy production, need to be adequately generalized to nonequilibrium regime, and the fundamental limits set to heat-to-work conversion have to be reconsidered. The theoretical framework of Stochastic Thermodynamics [148], based on universal nonequilibrium fluctuation theorems [149, 150], has been widely employed to describe energy conversion in these microscopic engines, as it models heat, work and entropy production as stochastic quantities. The search for optimal working performance of these machines is relevant in the so-called field of finite-time thermodynamics [151, 152].

Steady-state thermal machines, e. g. thermoelectric devices contacted with time-independent reservoirs [153], belong to the class of autonomous thermal machines. Several interesting results have been derived for these machines, e. g. in the absence of time-reversal symmetry due to a magnetic field Carnot efficiency can be achieved at finite power [154]. Quite recently, a universal tradeoff relation has also been estabilished in the classical domain, linking the entropy production to power output and power fluctuations [155, 156], i. e. the so-called Thermodynamics Uncertainty Relations (TUR). TUR rule the tradeoff between entropy production and the output power relative fluctuations, i. e. the precision of the machine, so that working machines operating at near-to-zero entropy production cannot be achieved without a divergency in the relative output power fluctuations. Quite recently, a generalization of TUR has been provided in the context of periodically-driven systems, and operationally-accessible

bounds to entropy production, i.e. written in terms of quantities directly accessible to experiment [157, 158].

The implications of quantum mechanics on the mechanism of heat to work conversion have been not yet completely understood [26]. Fluctuation theorems have been generalized to the quantum domain [159, 160], so that a theoretical description of quantum fluctuations of heat and work has been provided. However, the measurement problem poses nontrivial difficulties to probe work statistics [161], and several measurement strategies have been devised to solve the issue [162]. A further fundamental difficulty is the lack of a rigorous definition of work, heat and entropy production in the presence of strong correlations with the thermal reservoirs [163].

However, different models of quantum heat engines and refrigerators have been devised, where the working medium can consist of a single driven TLS [23, 24, 164, 165], couples of harmonic oscillators [166, 167], pairs of qubits subject to unitary gates [168], quantum dots, autonomous motors made of Brownian particles [169], as well as many body systems near criticality [170]. Otto cycles, Carnot cycles, both in the adiabatic and finite-time configuration have been considered, where the working medium undergoes a finite number of strokes [24], and it is put in contact with two thermal reservoirs. In these works, different interesting results for the efficiency at maximum power have been reported, showing that in some cases the upper bound of the efficiency can be quite different from the Curzon-Ahlborn bound [171], while in some others the engine performance are found to depend on the bath spectral properties [80]. Despite all these efforts, it remains unclear whether or not the quantum nature of the working medium can provide a relevant enhancement in the efficiency of heat to work conversion. Further, the experimental realizations of these devices remain limited [172–174].

Great part of these works model the coupling with the reservoir by making use of Quantum Master Equations (QME), thus limiting the analysis to the weak coupling regime, while the mechanism of heat to work conversion in the strong coupling regime has received much less attention [175–179]. Furthermore, in the case of periodically-driven quantum engines, the actual validity of the tradeoff relations between entropy production, output power and fluctuations, devised in the classical Markovian setting, remains highly controversial [180].

Below, we consider a simple model of periodically driven, isothermal machine, where the working medium consists of a single TLS, driven by two external periodic fields of fixed amplitudes and permanently put in contact with a thermal bath. Similar machines, which have been recently discussed in the classical setting using linear irreversible thermodynamics [181], act as prototypes of work-to-work converters, where the work spent in the input channel, corresponding to positive entropy production, is converted to the output channel with

fixed efficiency. Employing a standard definition of work [179], we numerically simulate the dynamics of this engine for different values of the model parameters, restricting to linear response regime. We compute the efficiency, the output powers and fluctuations as functions of the model parameters, i. e. driving frequency, phase difference and dissipation strength. Our numerical approach, based on Short Iterative Lanczos (SIL) method, allows us to provide a reliable description of the system dynamics from weak to moderately strong dissipation, in the low-temperature regime, with almost no limitations on the value of the driving frequency. We show that a violation of TUR can occur in a wide range of model parameters, so that different working regimes exist in which the quantum converter may achieve a better tradeoff between entropy production and output power fluctuations.

4.1 SETUP OF THE CONVERTER

We model our system with a TLS in the presence of two external time-periodic driving fields of fixed amplitudes, phase difference and frequency ω. The TLS is in contact with a heat bath at fixed temperature T, as sketched in Fig. 4.1. Following Sec. 1.4, the Hamiltonian of the whole system can be written as

$$H(t) = H_S(t) + H_B + H_{SB}, \tag{4.1}$$

where $H_S(t)$, H_B are respectively the free Hamiltonian of the system and bath and H_{SB} is the interaction energy between the TLS and the bath.

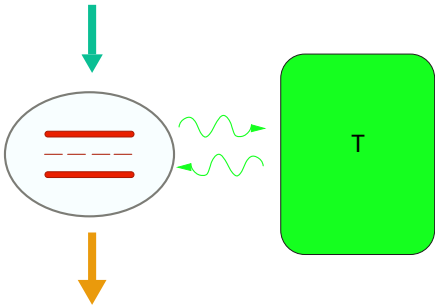

Figure 4.1: Schematic diagram of the coverter: a the TLS bias is periodically modulated in time, while the TLS is in contact with a thermal reservoir at fixed temperature T.

We choose for the TLS Hamiltonian the following form

$$H_S(t) = -\frac{1}{2}(\varepsilon_1(t) + \varepsilon_2(t))\sigma_z - \frac{\Delta}{2}\sigma_x. \tag{4.2}$$

Here Δ is the tunnelling element, and $\varepsilon_1(t), \varepsilon_2(t)$ are two external periodic driving fields, i. e. $\varepsilon_i(t) = \varepsilon_i(t + \mathcal{T})$, $i = 1, 2$, which

modulate the levels asymmetry. While there is no limitation on the form of the driving fields, we fix their configuration as follows: $\varepsilon_1(t) = \varepsilon_1 \sin \omega t$, $\varepsilon_2(t) = \varepsilon_2 \cos(n\omega t - \phi)$, where $\varepsilon_1, \varepsilon_2$ are the driving field amplitudes, $\omega = 2\pi/\mathcal{T}$ is the driving frequency and ϕ is the phase difference.

As in the previous chapters, we choose as a set of basis states for the TLS the eigenstates of σ_z operator, i. e. $\sigma_z |\hat{z}; \pm\rangle = \pm |\hat{z}; \pm\rangle$. We model the bath as in Eq. (1.8), and we fix the system-bath interaction as customary in the SBM, i. e. Eq.(1.9).

In this system the TLS, i. e. the working medium, is driven out of equilibrium by means of the two external fields, while the permanent contact with the bath induces dissipation and decoherence. Although Floquet theory provides a satisfactory description of the nonequilibrum dynamics of periodically-driven systems in the absence of system-bath interactions, the physical description of the open system dynamics beyond conventional Born-Markov approximation is still incomplete [182].

For this class of driven open quantum systems, at long times a nonequilibrium stationary state is expected, where the reduced density matrix of the TLS undergoes periodic time evolution with period $\mathcal{T}$. In this regime, the dynamics of energy exchange shows that the expectation values of the different contributions to the Hamiltonian operator in Eq. (4.1), i. e. $\langle H_S(t) \rangle$, $\langle H_B \rangle$, $\langle H_{SB} \rangle$, exhibit a periodic evolution with period equal to $\mathcal{T}$. However, the constant time-averaged power injected by the external drive onto the system is entirely drained by the bath, i. e. the powers drained by the TLS and the interaction channel SB average to zero over a period $\mathcal{T}$.

Provided that the two external driving fields can be experimentally distinguished [183], several parameter ranges of the model in Eq. (4.1) exist where the two fields behave as input and output channels, i. e. the mean powers of the different driving fields are opposite in sign and the whole system acts as a work-to-work converter. For sufficiently small amplitudes of the driving fields with respect to the driving frequency ω, a description based on linear irreversible thermodynamics [153, 181] can be employed, i. e. the mean values of the input and output powers to the field amplitudes $(\varepsilon_1, \varepsilon_2)$, the formers being proportional to the currents, while the latters playing the role of thermodynamic forces.

Similar models of converters have been studied [183], where in place of a single TLS a quantum Brownian particle in a tight-binding lattice has been considered. In the weak-tunnelling regime, it has been shown that the system can reach optimal performance maximizing the efficiency at finite power and achieving low power fluctuation, thus violating TUR over a wide range of driving frequencies. In the subsequent sections, we study the linear nonequilibrium properties of our converter: we first find regions in the parameter space where

work-to-work conversion occurs; then, we find evidence for systematic violations of TUR, which show up in the region of weak dissipation and in the low temperature regime.

4.2 ENERGY BALANCE OF THE SYSTEM

The dynamics of system in Eq. (4.1) is described by the density matrix $\rho(t)$, which obeys to Von Neumann equation of motion

$$\frac{d}{dt}\rho(t) = -i[H,\rho], \tag{4.3}$$

From the total density matrix, the state evolution of any subsytem belonging to the bipartition can be determined by performing the partial trace over the degrees of freedom of the other subsystem. The reduced density matrix of the TLS can be written as

$$\rho_S(t) = \mathrm{tr}_B\, \rho(t) \tag{4.4}$$

where the partial trace is taken over the bath degrees of freedom. The knowledge of the density matrix $\rho(t)$ allows us to compute the expectation value of the total energy of the system as follows

$$\langle H(t)\rangle = \mathrm{tr}\,[H(t)\rho] \tag{4.5}$$

Due to the external driving fields, the expectation value of the total energy of the system changes in time. From Eq. (4.1), we have

$$\frac{d}{dt}\langle H(t)\rangle = \mathrm{tr}\left[\frac{\partial H_S(t)}{\partial t}\rho\right] \tag{4.6}$$

We can thus define the power operator linked to each driving field as follows

$$P_i(t) = -\frac{1}{2}\dot{\varepsilon}_i(t)\sigma_z(t) \tag{4.7}$$

where $i = 1, 2$. These operators describe the exchanges of work per unit time linked to the converter. In general, the dynamics of $\rho(t)$ is nontrivial, due to the combined effects of the external fields and dissipation. However, at sufficiently long times a nonequilibrium stationary state is reached, where the state of the system evolves periodically in time, with period $\mathcal{T}$. Hence, at long times we can describe the physical properties of the system in terms of time-averaged expectation values of the power operators

$$\overline{P}_i = \frac{1}{\mathcal{T}}\int_t^{t+\mathcal{T}} \langle P_i(t')\rangle\, dt' \tag{4.8}$$

As it follows from analytical results [134], at long times the total power associated to the two channels is drained by the bath, i. e. the time

derivatives of the expectation values $\langle H_S(t)\rangle, \langle H_{SB}\rangle$ average to zero over a period $\mathcal{T}$. This can be directly seen by computing the time evolution of the former expectation values, showing that they evolve periodically in time (see Sec.4.4.1). This property allows to unambiguously define the heat exchanged with the bath per unit time, i. e. $\dot{\mathcal{W}}_B$ as the energy which flows into the bath per unit time, reading

$$\dot{\mathcal{W}}_B = -\operatorname{tr}[H_B\dot{\rho}] = i\operatorname{tr}[[H_B, H_{SB}]\rho]\,. \tag{4.9}$$

Integrating Eq. (4.9) over a period, from Eq. (4.8) we find

$$\mathcal{W}_B = -\int_t^{t+\mathcal{T}} \operatorname{tr}[H_B\dot{\rho}]\,dt = \langle H_B(0)\rangle - \langle H_B(T)\rangle = \mathcal{T}(\overline{P}_1 + \overline{P}_2) \tag{4.10}$$

Eq. (4.10) fixes the energy balance of our machine in the nonequilibrium steady-state regime. The system operates as a work-to-work converter if the average powers are opposite in signs, i. e. one of the channels behaves as the output, thus converting part of the work per unit time spent in input. We are interested in the efficiency of the conversion, which reads

$$\eta = \frac{|\overline{P}_{out}|}{\overline{P}_{in}}, \tag{4.11}$$

where we conventionally take as the output channel the one which brings negative power: $P_{out} = \overline{P}_1(\overline{P}_2)$ if $\overline{P}_1(\overline{P}_2) < 0$. Achieving a conversion efficiency close to 1 means that a small amount of the power spent in output is dissipated into the bath. However, in cyclic engines high efficiency has been often achieved in the adiabatic limit, with low output power. Furthermore, diverging output power fluctuations have been reported [170], which could hinder the performance of any engine. In order to characterize the converter performance, the computation of the output power fluctuations is thus needed. Following a recent work [183], at long times t, i. e. when the nonequilibrium stationary state has been reached, the power fluctuations can be computed as follows

$$D_i(t) = \int_0^\infty d\tau(\langle \delta P_i(t)\delta P_i(t-\tau)\rangle + \langle \delta P_i(t-\tau)\delta P_i(t)\rangle) \tag{4.12}$$

where $P_i(t)$ is the power operator and $\delta P_i(t) = P_i(t) - \langle P_i(t)\rangle$. The brackets indicate the quantum mechanical expectation value using the whole system + bath density matrix at time t. Inserting Eq. (4.8) into Eq. (4.12) and taking the time average over a period, the time-averaged power fluctuations can be expressed in terms of the two-time correlation functions

$$\overline{D}_i = \frac{1}{2\mathcal{T}}\int_0^{\mathcal{T}} dt\dot{\varepsilon}_i(t)\int_0^\infty d\tau\dot{\varepsilon}_i(t-\tau)(\operatorname{Re}\{\langle\sigma_z(t)\sigma_z(t-\tau)\rangle\} - \langle\sigma_z(t)\rangle\langle\sigma_z(t-\tau)\rangle) \tag{4.13}$$

For fixed driving frequency ω, the ratio of input and output powers over the corresponding field amplitudes can be modeled as currents of a two-terminal steady-state machines [153, 181, 183], where the field amplitudes ε_i play the role of the thermodynamic forces. Hence, it is possible to investigate the tradeoff between output power, entropy production and output power fluctuations for the work-to-work converter in the nonequilibrium steady-state regime.

As anticipated in the introduction, in the classical thermodynamics context it has been shown that currents in microscopic steady-state devices are linked to their mean fluctuations and to entropy production σ by means of TUR. In the case of our converter, TUR reads

$$\sigma \frac{\overline{D}_{\text{out}}}{\overline{P}^2_{\text{out}}} > 2. \tag{4.14}$$

Here it is worth rewriting the left hand side of Eq. (4.14), i. e. our tradeoff parameter, in terms of the conversion efficiency in Eq. (4.11) as follows

$$\mathcal{Q} = \sigma \frac{\overline{D}_{\text{out}}}{\overline{P}^2_{\text{out}}} = \beta \overline{P}_{\text{out}} \left(\frac{1}{\eta} - 1 \right) \Sigma^2_{\text{out}} \tag{4.15}$$

where $\Sigma_{\text{out}} = \sqrt{\overline{D}_{\text{out}} / \overline{P}^2_{\text{out}}}$ is the relative power uncertainty. This relation imposes a lower bound to the product of power fluctuations and entropy production at fixed output power, so that in the reversible operation regime the divergency of relative fluctuations follows. Several works have reported violations of TUR in the quantum realm [184], and a possible explanation has been proposed in [180], pointing towards a smaller lower bound set by quantum mechanics with respect to the classical case.

However, TUR has been recently generalized to the particular instance of periodically-driven nonequilibrium engines [158] as follows

$$\sigma(\omega) \frac{\overline{D}_{\text{out}}(\omega)}{\overline{P}^2_{\text{out}}(\omega)} > 2 \left(1 - \frac{\omega}{\overline{P}_{\text{out}}(\omega)} \overline{P}'_{\text{out}}(\omega) \right)^2 . \tag{4.16}$$

Eq. (4.16), as compared to the static relation, provides an expression for the bound written in terms of experimentally accessible quantities.

The nonequilibrium dynamics of the expectation values of power operators in Eq. (4.8), along with the two-time correlation function in Eq. (4.13) for the work-to-work converter in Eq. (4.1) can be computed numerically by employing the SIL method (see Chpt. 2), for every value of the fields amplitudes. We can thus compute all the quantities involved in Eq. (4.16) and look for possible violations. In the following section, we focus on the characterization of the converter in the linear response regime, i. e. adopting the framework of linear irreversible thermodynamics [153, 181]. This formalism allows us to easily find optimal operating regimes for the work-to-work conversion. We discuss the results and the regime of validity of the theory, postponing the nonlinear analysis to a subsequent work.

4.3 LINEAR RESPONSE REGIME

Following linear response theory, the Hamiltonian in Eq. (4.1) can be rewritten by grouping all the operators which explicitly depend on time t in the following way

$$H = H_o + H_{ext}(t),\ H_{ext}(t) = -\sum_{i=1,2} \frac{1}{2}\varepsilon_i(t)\sigma_z \tag{4.17}$$

where the operator H_o is the time-independent unperturbed Hamiltonian. In this limit, the term $H_{ext}(t)$ acts as a perturbation to the Hamiltonian H_o. The fluctuation of the expectation value of a generic observable $O(t)$ with respect to the unperturbed case can be written at first order in the perturbation $H_{ext}(t)$ as follows

$$\langle O(t)\rangle - \langle O(t)\rangle_o = \frac{i}{\hbar}\int_{t_0}^{t} dt' \left\langle \left[H_{ext}(t'), O(t)\right]\right\rangle_o \tag{4.18}$$

where $\langle O(t)\rangle = \langle \Psi(t_0)| O(t) |\Psi(t_0)\rangle$, the subscript 0 indicates that the expectation values are computed with respect to the unperturbed, time-independent Hamiltonian H_o, and $|\Psi(t_0)\rangle$ is the ket state at $t = t_o$. Here we want to compute the response of the power operators in Eq. (4.7): inserting the formal expressions of the operators in Eq. (4.18), we obtain

$$\langle P_j(t)\rangle - \langle P_j(t)\rangle_o = \frac{1}{4}\sum_{i=1,2}\int_{t_0}^{\infty} dt' \dot{\varepsilon}_j(t)\varepsilon_i(t')\chi(t,t'), \tag{4.19}$$

where we recasted Eq. (4.18) in terms of the susceptibility $\chi(t,t')$

$$\chi(t,t') = -\frac{i}{\hbar}\Theta(t-t')\left\langle \Psi(t_0)\right| \left[\sigma_z(t), \sigma_z(t')\right] \left|\Psi(t_0)\right\rangle_o . \tag{4.20}$$

Here $j = 1,2$ and the σ_z operators are computed in the Heisenberg representation of the unperturbed Hamiltonian H_o. At long times t, the correlation function on the right-hand side of Eq. (4.21) becomes a function of the time differences $t - t' = \tau$ and the expectation value $\langle P_j(t)\rangle_o$ vanishes.

After straightforward manipulations, we can take the average of the power expectation values over a period $\mathcal{T}$ of the driving frequency, in order to compute the nonequilibrium stationary mean powers as in Eq. (4.8) in the limit of linear response. Introducing the correlation function $C(\tau) = \left\langle \Psi(\bar{t})\right| \sigma_z(\tau)\sigma_z(0) \left|\Psi(\bar{t})\right\rangle_o$, where $\bar{t}$ is a sufficiently long time, we find for the mean powers

$$\overline{P}_j = \overline{\langle P_j(t)\rangle} = \frac{1}{2\hbar}\sum_{i=1,2}\frac{1}{\mathcal{T}}\int_0^{\mathcal{T}} dt \dot{\varepsilon}_j(t)\int_0^{\infty} d\tau \varepsilon_i(t-\tau)\,\mathrm{Im}\{C(\tau)\} \tag{4.21}$$

From Eq. (4.21), we can easily derive the general form of the Onsager matrix, which links the mean powers $\overline{P}_j$ to the field amplitudes as follows

$$\overline{P}_i = \sum_{j=1,2}\mathcal{L}_{ij}(\omega)\varepsilon_i\varepsilon_j \tag{4.22}$$

In this limit, the element of the Onsager matrix can be expressed in terms of the Fourier transform of the correlation function $\mathrm{Im}\{C(\tau)\}$, i. e. we rewrite Eq. (4.21) in terms of $\chi(\omega) = \int_0^\infty \exp(i\omega\tau)\,\mathrm{Im}\{C(\tau)\}d\tau$. Thus, inserting the field expressions $\varepsilon_1(t), \varepsilon_2(t)$ into Eq. (4.21), for each value of the driving frequency ω and the phase difference ϕ, the Onsager matrix reads

$$\begin{aligned}
\mathcal{L}_{11}(\omega) = \mathcal{L}_{22}(\omega) &= -\frac{\omega}{4}\,\mathrm{Im}\{\chi(\omega)\} \\
\mathcal{L}_{12}(\omega) &= \frac{\omega}{4}(\cos\phi\,\mathrm{Re}\{\chi(\omega)\} - \sin\phi\,\mathrm{Im}\{\chi(\omega)\}) \\
\mathcal{L}_{21}(\omega) &= -\frac{\omega}{4}(\cos\phi\,\mathrm{Re}\{\chi(\omega)\} + \sin\phi\,\mathrm{Im}\{\chi(\omega)\})
\end{aligned} \tag{4.23}$$

The knowledge of Onsager functions allows us to access the mean fluctuations of the output powers. Following a similar treatment as in Eq. (4.21), we can write

$$\overline{D}_\mathrm{i} = \frac{\varepsilon_i^2\omega^2}{4}\int_0^\infty d\tau\cos\omega\tau(\mathrm{Re}\{C(\tau)\}) \tag{4.24}$$

The last expression can be easily written in terms of the diagonal elements of the Onsager matrix: making use of the standard fluctuation-dissipation equalities holding at equilibrium, i. e. at long times t, we find

$$\overline{D}_\mathrm{i} = \varepsilon_i^2\omega\coth(\beta\omega/2)\mathcal{L}_{ii}(\omega) \tag{4.25}$$

From eqs. (4.21) and (4.24), it follows that the computation of the correlation function $C(\tau)$ allows us to characterize the nonequilibrium dynamics of the converter in the linear response regime. We stress that, although the function $C(\tau)$ is computed from the interacting spin-boson Hamiltonian in the absence of external fields, analytical solutions for $C(\tau)$ are limited to special values of the dissipation strength [91]; as a consequence, even in the linear response regime, a fully numerical approach is required.

Once the Onsager matrix is known, optimal working conditions can be easily found with straightforward algebra [153]. The line of maximum efficiency (ME) in the parameter space $(\varepsilon_1, \varepsilon_2)$, for fixed driving frequency and phase difference (ω, ϕ) reads

$$\varepsilon_{1\mathrm{ME}} = -\frac{\mathcal{L}_{22}(\omega)}{\mathcal{L}_{21}(\omega)}\left(1 - \sqrt{\frac{\det\mathcal{L}}{\mathcal{L}_{11}(\omega)\mathcal{L}_{22}(\omega)}}\right)\varepsilon_2. \tag{4.26}$$

Here $\det\mathcal{L}$ indicates the determinant of the Onsager matrix. Notice that when the system operates in TR symmetric regime, i. e. $\phi = \pi/2$, the Onsager matrix is symmetric, and all its element are equal to one another.

4.4 CONVERTER PERFORMANCE AND BOUND VIOLATIONS

Below, we simulate numerically the dynamics of the converter in the linear response regime. We employ the numerical SIL approach, which as explained in Chpt. 2 allows us to compute the unitary dynamics of the driven TLS + bath density operator $\rho(t)$, after a controlled truncation of the bath Hilbert space. We first identify regions in the parameter space where the system operates as a work-to-work converter; then, by choosing the operating point at ME, we characterize the performance of our converter, i. e. output power, efficiency and fluctuations, for different values of the coupling strength α, in the low temperature regime where non-Markovian effects are expected. Eventually, we compute both sides of Eq. (4.16) and indentify several frequency intervals where the Markovian TUR is violated. We also discuss the limits of validity of linear response regime, as SIL method can be employed with no further restrictions beyond linear response.

4.4.1 Powers, efficiency, fluctuations

We set the density matrix of system and the bath at initial time t_0 in a factorized state as in the previous chapters

$$\rho(t_0) = \rho_S(t_0) \otimes \frac{e^{-\beta H_B}}{Z_B}, \tag{4.27}$$

where $\rho_S(t) = \rho_S(t_0) = |\hat{z};+\rangle\langle\hat{z};+|$. Thus, we simulate the nonequilibrium dynamics of the expectation values of one time and two-time operators of interest, for different values of the model parameters, fixing the maximum number of excitations (see 2.1) $N_{ph} = 3$. In what follows, we set the fields $\varepsilon_1(t), \varepsilon_2(t)$ so that they modulate the level asymmetry of the TLS with the same frequency, i. e. we take $n = 1$. We start by describing the main features of the nonequilibrium dynamics of power operators in Eq. (4.7) and the energy exchange of the converter. In Fig. 4.2a, the dynamics of expectation values of power operators is plotted for fixed values of the field parameters, dissipation strength and temperature. It is shown that while the powers exhibit a transient behavior, marked by fast oscillations in time of decreasing amplitude, for $t \geq 30\Delta_{eff}^{-1}$ a stationary regime occurs, where the power expectation values undergo periodic oscillations in time, with period equal to $\mathcal{T}$, mean values over a period different from zero and opposite signs. A part of the work per unit time spent in a channel is thus given back in the other, i. e. the system operates as a work-to-work converter with finite efficiency η. The analysis of energy exchange among the TLS, the bath and interactions channels can be performed by plotting the expectation values of the different contributions in Eq. (4.1) as function of time, as reported in Fig. 4.2b. Notice that also the different

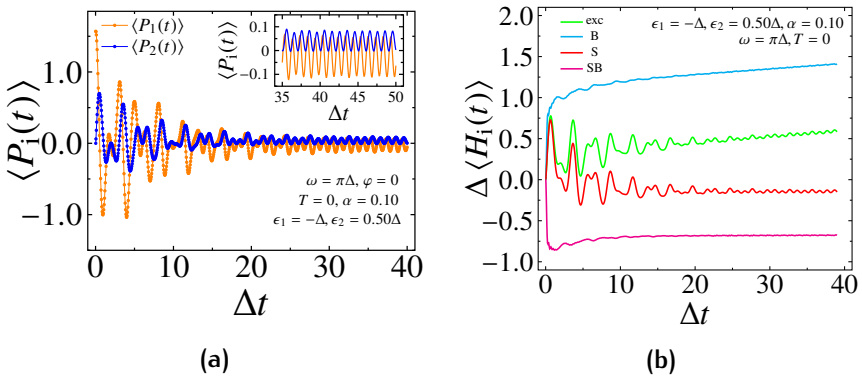

Figure 4.2: Panel a: Expectation value of power operators $\langle P_i(t)\rangle$, $i = 1, 2$ as function of time t, with fixed parameter $\varepsilon_1 = -\Delta, \varepsilon_2 = 0.50\Delta, \alpha = 0.10, T = 0, N_{\text{ph}} = 3$. Inset: nonequilibrium stationary state at long time show mean powers oscillating with period $\mathcal{T}$, and the time averages are of opposite signs, signaling work-to-work conversion. Panel b:variation of the expectation values of energy operators in Eq. (4.1), i. e. $\Delta\langle H_i(t)\rangle = \langle H_i(t)\rangle - \langle H_i(0)\rangle$ with $i = \text{S}, \text{B}, \text{SB}$ and exc indicating the total energy pumped in the system at time t. It can be noticed that the excess energy is entirely drained by the bath.

energy contributions experience a transient behavior, and at sufficiently long times a nonequilibrium stationary state is reached, where they oscillate in time with period $\mathcal{T}$. However, the analysis confirms that the mean total power injected into the system, i. e. $P = P_{\text{in}} - P_{\text{out}}$ is entirely drained by the bath while the TLS and the interaction energies oscillate around constant values, and the mean power drained by their channels vanishes. We stress that Fig. 4.2 reports the numerically exact expectation values of the operators of interest, without recurring to linear response. This is an advantage of our numerical approach (see 2.1), which can be directly employed in the nonlinear regime. From Fig. 4.2, it follows that the energy exchange has a clear interpretation only in the nonequilibrium steady state, while during the transient time a nontrivial energy exchange mechanism among the three different channels shows up. Limiting the analysis to the linear response regime, from the expression of the Onsager matrix elements reported in Eq. (4.25) for fixed phase difference ϕ, the occurrence of a frequency region where work-to-work conversion is absent follows. In Fig. 4.3, we plot the mean powers related to channels 1, 2 against the driving frequency ω, as derived from Eq. (4.22), for fixed dissipation strength and temperature T: it can be noticed that they both hold positive for frequencies of the order of the renormalized gap of the TLS $\Delta_{\text{r}} = \Delta(\Delta/\omega_{\text{c}})^{\alpha/(1-\alpha)}$, i. e. when the driving frequency is near resonance. Here both the channels absorb the power injected into the system, which is entirely dissipated into the bath, i. e. the heat flux to the bath is maximum and no work conversion occurs. On the other hand, when driving the system with frequency sufficiently far from

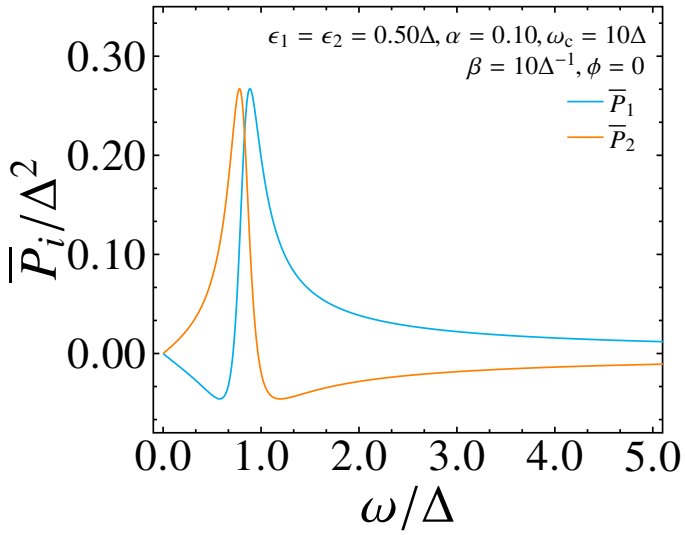

Figure 4.3: Average nonequilibrium powers $\overline{P}_1, \overline{P}_2$ computed in the linear response regime as function of the driving frequency ω, for fixed values of the fields amplitudes $\varepsilon_1 = \varepsilon_2 = 0.50\Delta, \alpha = 0.10, T = 0$. It is evident that a distinct region of driving frequencies exists so that the system cannot operate as work-to-work converter.

the resonance, the conversion takes place with finite efficiency. These results clearly depend on the phase difference ϕ between the two drives.

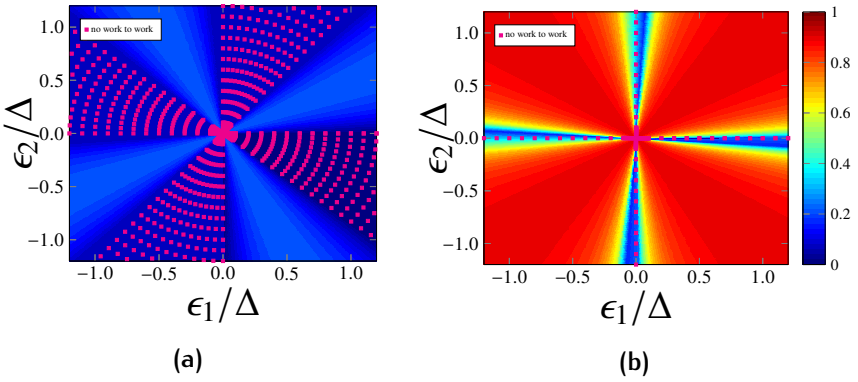

Figure 4.4: Efficiency as a function of the driving fields amplitudes $(\varepsilon_1, \varepsilon_2)$, plotted for fixed $\alpha = 0.10$, $T = 0.10\Delta$, $\phi = 0$ and $\omega = \{\Delta, 5\Delta\}$ respectively. Magenta dots indicate the parameter regions where no conversion occurs, while the ME line is plotted in cyan.

In what follows, we fix the phase difference $\phi = 0$, i. e. the converter operates in a TR asymmetric configuration and the Onsager matrix is antisymmetric. The conversion efficiency η can be computed from Eq. (4.11) as a function of the field amplitudes $(\varepsilon_1, \varepsilon_2)$, for fixed dissipation strength and temperature. In Fig. 4.4 we plot the efficiency for two different values of the driving frequency $\omega = (\Delta, 5\Delta)$. It is evident that, tuning the driving frequency near the resonance, all but lim-

ited regions of the plane $(\varepsilon_1, \varepsilon_2)$ exhibit no work-to-work conversion, while in the regions where conversion occurs a very low efficiency is achieved. On the other hand, tuning the frequency out of resonance a very different scenario can be observed, where the efficiency reach near-to-one value along the ME lines (cyan squares in Fig. 4.4) in Eq. (4.26), while small but finite input and output powers can be achieved.

As a consequence, choosing the converter operating point along the ME line allows us to optimize its performance. However, the analysis of the fluctuations of the output powers in this regime is also required, as with any microscopic heat engine. In addition, the mean fluctuations enter directly in the definition of TUR in Eq. (4.16). Moreover, an increase in the strength of dissipation at fixed temperature degrades the performance of the converter, changing the behavior of output power, efficiency and fluctuations. We set the operating point of the converter on the ME line and we investigate the non Markovian effects of dissipation on the converter performance, for any frequency value ω, at fixed temperature. In Fig. 4.5, we report the plots of the absolute value of output power, efficiency and mean fluctuations as function of the driving frequency, at fixed temperature $T = 0.1\Delta$ and for different values of the coupling strength α, taken in the range $1.25 \cdot 10^{-2}$ to $2.0 \cdot 10^{-1}$.

The powers in the two channels at ME are quite different from those in Fig. 4.3, as they don't change sign crossing the resonance. Fig. 4.5a shows the plot of the absolute value of the output power as function of driving frequency ω. A characteristic double-peak feature, separated by a narrow region where it drops to zero is clearly visible. By increasing the driving frequency ω, the output as well as the input power smoothly decreases. For increasing dissipation strengths, the double peak structure tends to smooth down and the resonance frequency, due to progressive shrinking of the TLS gap, moves toward lower frequencies. The input power changes similarly as function of dissipation strength α. As a direct consequence of this behavior, it can be noticed that the maximum efficiency curve η_{ME}, plotted in Fig. 4.5c, decreases in the whole frequency region with increasing α, i. e. the entropy production grows as a function of dissipation strength. However, even in the presence of moderately strong dissipation, i. e. $\alpha < 0.2$ the efficiency retains much of its shape and, for increasing frequencies ω its value remains above 0.50.

Mean fluctuations of the output power are shown in Fig. 4.5b as a function of the frequency ω. Notice that, in the resonance region the function shape is quite similar to the output power, though the double-peaked structure shows evident asymmetry. Fluctuations also decay at high driving frequencies. However, a marked difference with respect to the output power can be observed: sufficiently far from resonance, for increasing the coupling strength α a distinct growth

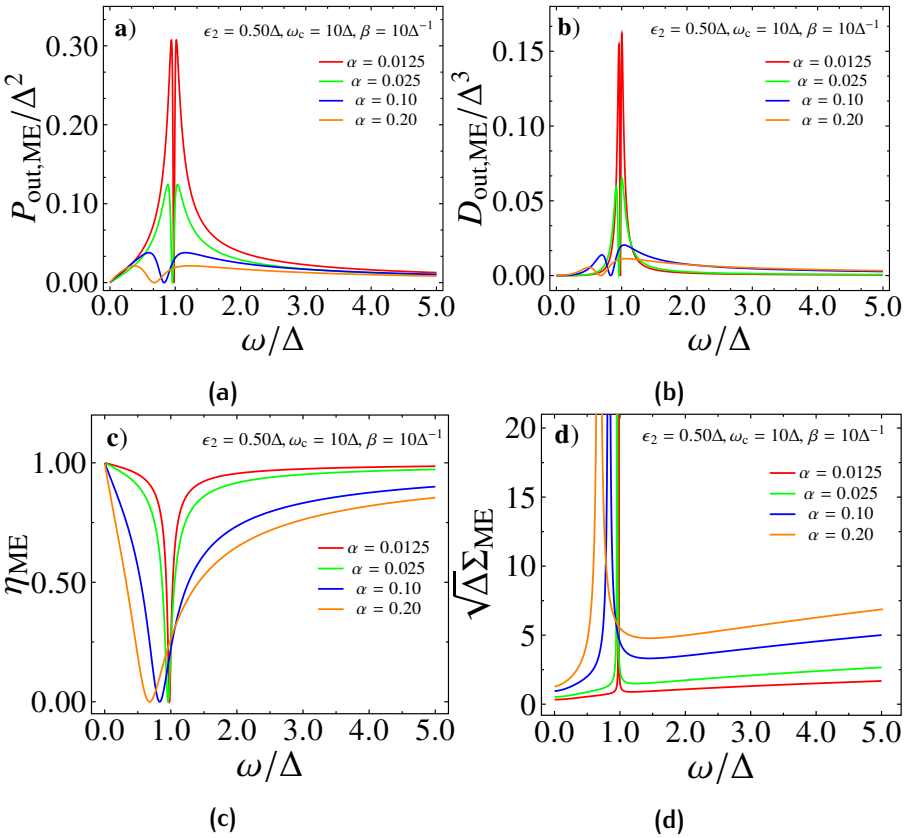

Figure 4.5: Performance of the work-to-work converter at ME as a function of the driving frequency ω, for different values of the dissipation strength α and fixed temperature $T = 0.10\Delta$. In Panel a, the absolute value of the output power P_{out}. In Panel b, the output power fluctuations; in Panel c, the efficiency curve computed from Eq. (4.11); in Panel d, the relative power uncertainty $\Sigma = \sqrt{D_{\mathrm{out}}/P_{\mathrm{out}}^2}$. The phase difference has been fixed to $\phi = 0$, and $\varepsilon_2 = 0.5\Delta$, so that the chosen point along ME line in Eq. (4.26) remains fixed for each value of ω.

in the mean fluctuations can be observed. This feature, along with the increase in the entropy production and the renormalization of the tunnelling element, is a characteristic effect of the quantum dissipative environment on the working medium. By inspecting the mean relative uncertainty, reported in Fig. 4.5d, it is shown that a divergency occurs in the vicinity of resonance region, mainly due to the rapid drop of output power with respect to fluctuation. Further, for increasing driving frequencies the relative uncertainty falls to a minimum and then start to grow slowly, i. e. at high frquency the converter porgressively loses precision. The loss of precision in the conversion process tends to increase mainly to the environment effect.

4.4.2 TUR violations

The study of converter performance as a function of the driving frequency and dissipation strength, carried out in the previous section, allows us to investigate the validity of TUR in Eq. (4.14) and (4.16) in the quantum domain. We compute the tradeoff parameter at ME $\mathcal{Q}_{ME}$, i. e. the left-hand side of Eq. (4.14), which links the conversion efficiency η, the output power P_{out} and the relative uncertainty Σ_{out}, as a function of the driving frequency ω, for different coupling strengths α and fixed temperature $T = 0.10\Delta$. We compare $\mathcal{Q}_{ME}$ with the lower bound, predicted in the static and periodically-driven fields case respectively. In Fig. 4.6a, we show the tradeoff parameter $\mathcal{Q}_{ME}$ as a

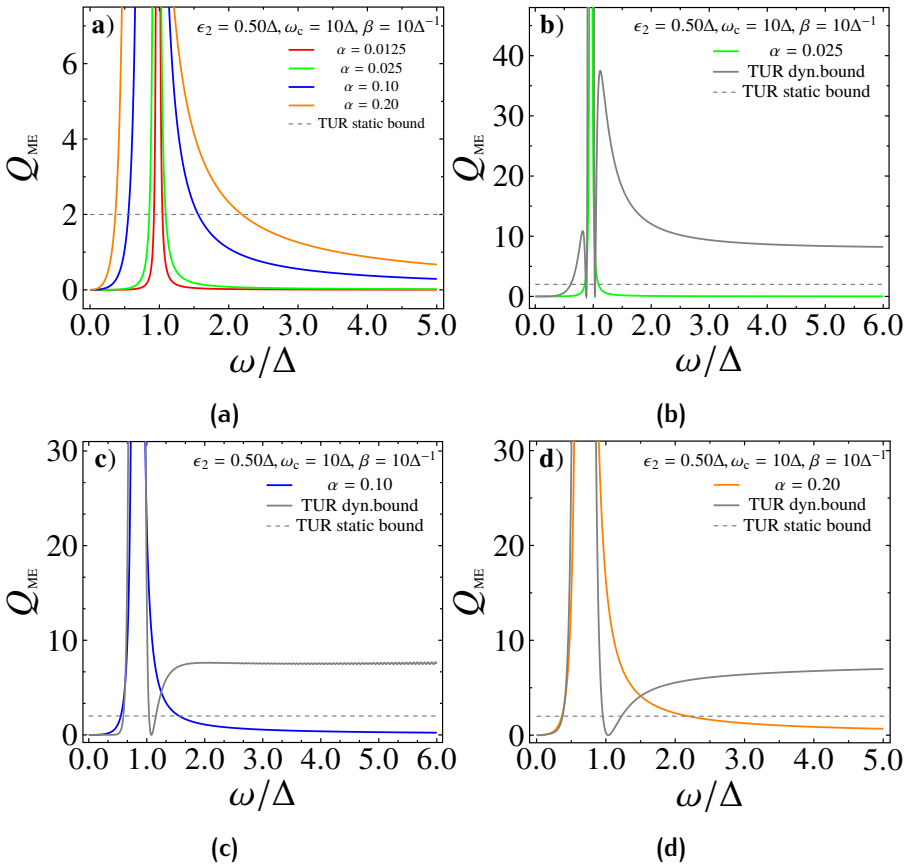

Figure 4.6: Tradeoff parameter $\mathcal{Q}_{ME}$ plotted as a function of the driving frequency ω, for different values of the coupling strength α, as compared with the lower TUR bounds in Eq. (4.14) and (4.14). The field parameters are the same as in Fig. 4.5. In Panel a, the parameter $\mathcal{Q}_{ME}$ is plotted against the static TUR bound, for different values of α. In Panels b,c,d, $\mathcal{Q}_{ME}$ is plotted against the dynamic bound, for $\alpha = 0.025, 0.10, 0.20$ respectively.

function of the driving frequency ω, computed for different values of dissipation strength. A divergency of the parameter $\mathcal{Q}_{ME}$ can be observed in the resonance region, which can be traced back to the peculiar behavior of relative fluctuations reported in Fig. 4.5d, while the

entropy production is finite. In this frequency region, where the system behaves as a trivial dissipator with no work-to-work conversion, the TUR holds. However, moving away from the resonance region, the tradeoff parameter falls well below the static bound in Eq. (4.14), thus violating the static TUR in a wide range of out-of-resonance driving frequencies. We stress that, from our numerical results of the tradeoff parameter $\mathcal{Q}_{ME}$, the violation of a finite static bound of the order of unity has also to be expected for sufficiently high driving frequencies. However, the observed violation might be due to the fact that Eq. (4.14) doesn't hold for periodically-driven systems, i. e. it has been derived for Markovian systems subject to static fields [155]. In Fig. 4.6, we thus compare $\mathcal{Q}_{ME}$ with the generalized bound in Eq. (4.16), which has been explicitly derived in the context of periodically-driven Markovian systems. Here it can be shown that, as in the static case, the resonance region exhibit a divergency which rules out any possible violation of Eq. (4.16). In addition, for ω slightly above and below resonance, the lower bound imposed by Eq. (4.16) vanishes, i. e. the output power is proportional to the driving frequency. It follows that, in the driven case even above resonance the TUR can be satisfied. On the other hand, this scenario dramatically changes at higher frequencies, where an even more pronounced violation of TUR with respect to the static case occurs. Due to the dependence of the dynamic bound on the output power, for increasing dissipation strength, our numerical results show that the shape of the bounding function in Eq. (4.16) undergoes severe changes. The double-peak structure above and below resonance tends to smooth down, while moving toward lower frequencies. It follows that at low frequency, the frequency region where violation is present reduces, while at high frequencies the dynamical bound decreases, and the tradeoff $\mathcal{Q}_{ME}$ increase.

Our analysis shows that the frequency regions where violation of TUR occurs progressively narrow with increasing dissipation strength, both in the static and dynamic setting. This could serve as a valid insight to explain that quantum coherence and non-Markovian effects induced by the system-bath coupling could be the main causes of the observed violations. Further useful tests would be the study of the tradeoff Q in the peculiar case of $\alpha = 1/2$, where the converter exhibit a completely incoherent dynamics due to the influence of the bath (see Chpt. 3). Also, the analysis in the Markovian setting, though extensively covered in the recent literature, could provide additional insights to shed light on the solution. Eventually, the extension of our analysis to nonlinear response regime would also add to the present understanding of the problem.

4.5 CONCLUSIONS

We studied the driven system in Eq. (4.1), showing that it can operate as a monothermal work-to-work converter. We provided a characterization of the converter performance by computing the efficiency, power fluctuations and output power in the linear response regime as function of the coupling strength α and driving frequency ω, in the low temperature regime. Combining these results, we tested the validity of classical TUR, in the driven as well as in the static field case. We found evidence of several parameter regions where the TUR are violated, i. e. a signature that the quantum machine in the time-reversal broken symmetry confguration ($\phi \neq \frac{\pi}{2}$) can achieve a better tradeoff between mean power fluctuations and entropy production for fixed power output. Actually the causes of these violations, which have been obtained in different contexts, are not yet clear. As it was observed in several works, in the static case the classical TUR relation in Eq. (4.14) may provide a wrong lower bound to the tradeoff $\mathcal{Q}$. In the quantum case, this lower bound has to be smaller [180], so that the observed violations could be traced back to the coherence of the quantum system. However, non-Markovian effects arising from system-bath correlations, correctly described by our simulation in a fairly wide range of parameters, may also play a role in the observed violation. A more accurate analysis of these violations is thus needed in order to achieve a better understanding of the physical scenario. A sensible starting point could be the test of the TUR relations in different limiting cases where analytical results are known, e. g. the completely incoherent tunnelling regime occurring at $\alpha = 1/2$ or the Markovian limit. Moreover, a quite unsettled and interesting issue is the test of validity of TUR in the nonlinear response regime, which we defer to a future work.

Part II

TOPOLOGICAL SYSTEMS IN THE PRESENCE OF E-PH INTERACTIONS.

5 SIMPLE MODELS OF TOPOLOGICAL INSULATORS

Topological insulators are one of the most active field of research in modern condensed matter physics. These materials are band insulators exhibiting a topologically non-trivial band structure [36, 37, 39]. The distinct topological phases are described in terms of the values of a bulk invariant [39], which depend both on the symmetries of the system and on the global properties of the band structure. The integer values assumed by the bulk invariants determine the presence of gapless edge modes, while the material has insulating behavior in the bulk.

Starting from the early-days experimental discovery of the integer Quantum Hall Effect (IQHE) [185] in 2D electron gas, described in terms of topological Chern number [186], the field has experienced a tremendous growth.

An enormous progress in the field has taken place following the works by Kane and Mele [187, 188], Bernevig and Zhang [189], who first theoretically predicted the existence of TR symmetry-protected topological band insulators in 2D, known as Quantum Spin Hall (QSH) insulators. In these systems, the possible topological phases are classified according to values of a $\mathbb{Z}_2$ invariant [188, 190, 191]; TR symmetry-protected helical (opposed chirality) pairs of edge modes are present and their number is related to the change in the value of $\mathbb{Z}_2$ invariant at the edge by bulk-boundary correspondence [36, 188, 189]. QSH insulators were found to belong to DII topological class [192–195]. Shortly after these works, the theory of QSH insulators was generalized to 3D [196], and it was confirmed by a number of experimental findings [197, 198]. Interestingly, the simultaneous presence of crystal symmetries and TR can lead to novel symmetry-protected topological states in 3-D, the so-called higher order topological insulators [199].

Topological insulators are short-range entangled topological phases of matter, being described by means of one-particle band theories. In general, the presence of electron-electron interactions are known to lead to topologically ordered phases [34], where the single-particle description cannot hold. The Fractional Quantum Hall Effect (FQHE) [200, 201], discovered in the 1980s, is now considered a prototype of topologically ordered state [36], exhibiting several distinctive properties, such as ground-state degeneracy, gapped anyonic excitations bringing fractional charge. However, the complete understanding of the effects of correlations on topological insulators remains an open problem, and it is the subject of an active field of research [40], as new

exotic states may arise from the interplay of nontrivial topology and interactions.

This chapter is aimed at giving a brief introduction to the general properties of two prototypical models of topological insulators which will be of interest below. We also quickly introduce the relations linking the band invariants to the fermionic Green functions, proposed in [202–205]. The knowledge of the Green function of the fermionic system in the presence of interactions allows us to compute the band invariants as function of the interaction parameters, thus sheding light on the properties of correlations.

5.1 CHERN INSULATORS

Models of Chern insulators describe fermions on a lattice showing nontrivial topological band structure properties , which are signaled by a nonzero Chern number. Historically, they have been introduced to describe fermionic systems displaying IQHE without a net magnetic flux through the lattice; in a modern perspective, they are considered as the simplest realization of topological insulators.

The IQHE has been first measured in systems of 2D electron gas in a Hall bar, i. e. subject to magnetic field of $B \simeq 10$ T orthogonal to the plane of the sample, in the low temperature regime. Transport measurement pointed towards the striking property of the existence of plateaus in the transverse Hall conductance

$$\sigma_{\mathrm{H}} = \nu \frac{e^2}{h}, \tag{5.1}$$

where ν, i. e. the filling factor, assumes perfectly quantized values. Furthermore, the occurrence of plateaus corresponds to the vanishing of longitudinal resistivity. It was soon realized that this property could be explained with the full occupation of Landau levels below the Fermi energy, when the latter lies in the localized tails of density of states between adjacent Landau bands. The noticeable absence of backscattering due to the structure of Landau states implies that electrons occupying the extended states in the Landau bands bring the same currents as with the bare Landau state, so that each Landau band contributes to the total conductivity by an amount e^2/h. Further, the lack of excited extended states in the vicinity of the Fermi level causes the longitudinal conductivity to vanish. However, the stability of the quantization was explained by Laughlin [201] in terms of the gauge invariance of the theory of the electron gas immersed in a magnetic field. Shortly after, in a subsequent work [186], by employing the Kubo formula the conductance of a system of fermions subject to

2D periodic potential and to an external magnetic field was shown to be written as follows

$$\sigma_{\mathrm{H}} = \frac{e^2}{h}\frac{1}{2\pi}\int\limits_{k_x,k_y\in BZ} dk_x dk_y \left(\frac{\partial A_y(\boldsymbol{k})}{\partial k_x} - \frac{\partial A_x(\boldsymbol{k})}{\partial k_y}\right), \tag{5.2}$$

where the components of the vector field $\boldsymbol{A}_i(\boldsymbol{k})$ read

$$A_i(\boldsymbol{k}) = -i\sum_{n \text{ filled}} \langle n,\boldsymbol{k}| \frac{\partial}{\partial k_i} |n,\boldsymbol{k}\rangle \, , \, i = x,y \tag{5.3}$$

Here $|n,\boldsymbol{k}\rangle$ are the 2D Bloch states of the electronic system, and the partial derivatives are taken with respect to the two components of wavevector (k_x,k_y). The integral in (5.2) is taken over the first Brillouin Zone (BZ) of the system. Due to the form of (5.2), the conductance can be rewritten by employing the Stokes theorem as follows

$$\sigma_{\mathrm{H}} = \frac{e^2}{h}\frac{1}{2\pi}\int\limits_{k_x,k_y\in BZ} d^2\boldsymbol{k}\cdot\boldsymbol{\nabla}\times\boldsymbol{A}(\boldsymbol{k}) = \frac{e^2}{h}\frac{1}{2\pi i}\int_C \boldsymbol{A}\cdot d\boldsymbol{r}, \tag{5.4}$$

where C is the "boundary" of BZ. Notice that the vector $\boldsymbol{A}$ is the Berry potential, where the Bloch states of the filled band replace the instantaneous eigenvectors of the Hamiltonian. In the formalism of Berry potential, a pure state $|\psi(0)\rangle$ evolves adiabatically in time under the Hamiltonian $H(\xi(t))$, which depends on the parameter $\xi(t)$. In the limit of adiabatic evolution, the evolved state at given time $\bar{t}$ differs from the instantaneous eigenstate of $H(\xi(\bar{t}))$, which we call $|\alpha(\xi(t')\rangle$, only by a phase $\gamma(t)$,

$$\gamma(t) = \frac{1}{\hbar}\int_0^{\bar{t}} E_\alpha(\xi(t'))dt' - i\int_0^{\bar{t}} \langle\alpha(\xi(t')|\frac{d}{dt'}|\alpha(\xi(t')\rangle\, dt'. \tag{5.5}$$

For a closed path in the parameters space, the phase assumes a form analogous to Eq. (5.3), as it reads

$$\gamma_\alpha = -i\int_C \langle\alpha(\xi)|\,\nabla_\xi\,|\alpha(\xi)\rangle\, d\xi, \tag{5.6}$$

It is known as geometric Berry phase. Provided that the instantaneous eigenvectors are single valued, the phase in Eq. (5.6) over a closed path is a gauge-invariant quantity. It also can change by integer multiples n of 2π. It follows that the Hall conductance has to be quantized as in Eq. (5.1).

The integer n is called Chern number. Actually, the rigorous proof of the quantization follows from the observation that Berry phase is an example of a Bott-Chern connection on principal $U(1)$-bundle. The curl of the Berry potential $\boldsymbol{A}$ is commonly called the Berry curvature, and it is the first Chern class corresponding to the connection. The integral over BZ of the Berry curvature, as in Eq. (5.2), is thus equivalent to the integration of the first Chern class over a torus T^2 in the

parameter space [206, 207]. A non-zero Chern number thus signals non trivial properties of the Berry potential in the BZ, i. e. a non trivial $U(1)$ bundle. It manifests by means of singularities in the vector potential $\boldsymbol{A}$, and it is equivalent to the impossibility of finding a global gauge in the parameters space continuous and single valued [39]. The singularity of the Berry vector potential implies that on the boundary between a Chern insulator and a trivial one, gapless chiral edge modes are present. The bulk-boundary correspondence links the change in

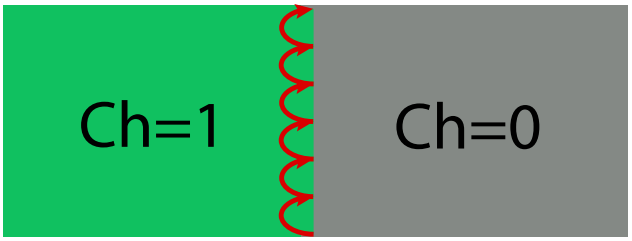

Figure 5.1: Schematic diagram of a chiral edge mode at the boundary of a nontrivial Chern insulator and a trivial insulator.

the Chern number across the interface with a trivial insulator to the number of edge modes, i. e. the number of edge modes is equal to Δn. Edge modes propagate in a single direction, as backscattering is not possible; they are reponsible for perfectly quantized conductance, and are robust against perturbations, i. e. the presence of disorder.

Band insulators exhibiting nontrivial Chern number, i. e. IQHE, can also occur in the absence of a net magnetic flux through the lattice plane [140]. The fundamental requirement to obtain IQHE is the absence of TR symmetry. In the following section, we introduce the prototypical model of the Haldane Chern insulator on a honeycomb lattice, which has been the first proposal in the field.

5.1.1 Haldane model of Chern insulator

The Haldane model [140] describes spinless fermions on a honeycomb lattice at half-filling. It is a tight binding model with nearest-neighbor (NN) and complex next nearest neighbor (NNN) hopping terms, including an on-site mass term, M. As compared to a conventional tight-binding models with NN hopping, the mass term M breaks the inversion symmetry of the lattice with respect to the center of the honeycomb cell (see Fig. 5.2a). The complex tunnelling breaks the time-reversal symmetry, realizing a staggered magnetic field on the lattice without a net magnetic flux through the plaquette. The Hamiltonian reads

$$H_H = -\sum_{i,j} t_{i,j} c_i^\dagger c_j + M \sum_i \xi_i c_i^\dagger c_i \tag{5.7}$$

where $c_i^\dagger(c_i)$ are fermionic creation (annihilation) operators on the site i, $t_{i,j} = t_1$ ($t_2 e^{i\xi_i \phi}$) is the nearest (next nearest) neighbor electronic

hopping, and ξ_i is an integer which takes the values ± 1 respectively on the two sublattices (A, B). As depicted in Fig. 5.2a, it is evident that the hopping elements of fermions on the two different sublattices are the complex conjugate of each other.

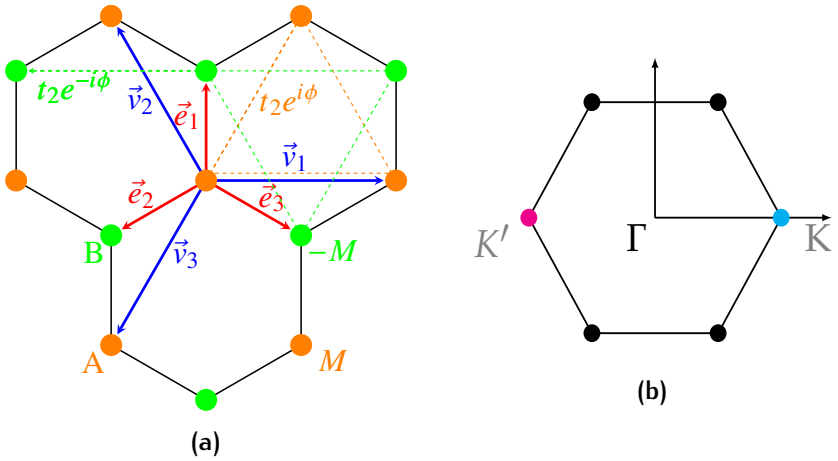

Figure 5.2: Panel a: the honeycomb lattice. In red, NN vectors $\boldsymbol{e}_i$, and the NNN vectors (blue arrows) $\boldsymbol{v}_i$, $i = 1,2,3$. Different sublattice sites A and B are labelled with different colors (orange,green). Dashed lines shows NNN complex hopping terms. Panel b: The B.Z. of the honeycomb lattice, with high-symmetry points K, K'

The model in Eq.(5.7) describes a topological Chern insulator, gapped at Dirac points K, K′ of the Brillouin zone. To show how it occurs, the Hamiltonian in Eq. (5.7) can be rewritten in the quasi-momentum space $\boldsymbol{k}$. We rewrite as (a_i, b_i) the two different fermionic operators at each sublattice site A, B, and take their Fourier transform $a_i(b_i) = \frac{1}{\sqrt{N_c}} \sum_k e^{i\boldsymbol{k}\cdot\boldsymbol{r}_i} a_k(b_k)$, where $N_c = N/2$. The Hamiltonian (5.7) can thus be written in the momentum space: for each vector $\boldsymbol{k}$ it can be recast in terms of that of a two level systems reading

$$H_H = \sum_k \begin{pmatrix} a_k^\dagger & b_k^\dagger \end{pmatrix} \left(\varepsilon(\boldsymbol{k})\, \mathbb{1} + \boldsymbol{h}(\boldsymbol{k}) \cdot \boldsymbol{\sigma}\right) \begin{pmatrix} a_k \\ b_k \end{pmatrix} \tag{5.8}$$

where

$$h_x(\boldsymbol{k}) = -t_1 \sum_i \cos(\boldsymbol{k} \cdot \boldsymbol{e}_i) \tag{5.9}$$

$$h_y(\boldsymbol{k}) = t_1 \sum_i \sin(\boldsymbol{k} \cdot \boldsymbol{e}_i) \tag{5.10}$$

$$h_z(\boldsymbol{k}) = M + 2t_2 \sin\phi \sum_i \sin(\boldsymbol{k} \cdot \boldsymbol{v}_i) \tag{5.11}$$

and $\varepsilon(\boldsymbol{k}) = -2t_2 \cos\phi \sum_i \cos(\boldsymbol{k} \cdot \boldsymbol{v}_i)$. Here σ_j, with $j = \{\hat{x},\hat{y},\hat{z}\}$ are the Pauli matrices along three spatial directions, while $\boldsymbol{e}_i$, $i = \{1,2,3\}$ are

three vectors in the lattice plane linking the NN sites (depicted in red in Fig. 5.2a), which read

$$\begin{aligned} \boldsymbol{e}_1 &= (0, \mathrm{a}) \\ \boldsymbol{e}_2 &= (-\frac{\sqrt{3}}{2}\mathrm{a}, -\mathrm{a}/2) \\ \boldsymbol{e}_3 &= (\frac{\sqrt{3}}{2}\mathrm{a}, -\mathrm{a}/2) \end{aligned} \tag{5.12}$$

Further, the vectors $\boldsymbol{v}_i$ (depicted in blue in Fig. 5.2a) link NNN sites belonging to the same sublattice

$$\begin{aligned} \boldsymbol{v}_1 &= (\sqrt{3}\mathrm{a}, 0) \\ \boldsymbol{v}_2 &= (-\frac{\sqrt{3}}{2}\mathrm{a}, \frac{3}{2}\mathrm{a}) \\ \boldsymbol{v}_3 &= (\frac{\sqrt{3}}{2}\mathrm{a}, \frac{3}{2}\mathrm{a}) \end{aligned} \tag{5.13}$$

and a is the lattice constant. In the vicinity of high symmetry points of the BZ of the honeycomb lattice, Eq. (5.8) has the form of a Dirac Hamiltonian [39], with a nonzero mass term. It is thus evident that for this model TR symmetry is broken even without a net magnetic flux through the lattice.

Thanks to its simple form, Eq. (5.8) can be diagonalized analytically, and the lower and upper band read

$$E_{k,\pm}(\boldsymbol{k}) = \varepsilon(\boldsymbol{k}) \pm \sqrt{h_x^2(\boldsymbol{k}) + h_y^2(\boldsymbol{k}) + h_z^2(\boldsymbol{k})}. \tag{5.14}$$

Notice that we are considering the chemical potential μ to be coincident with $E = 0$. From the two-band structure computed in the two nonequivalent points of the Brillouin zone, respectively $\mathrm{K} = (4\pi/(3\sqrt{3}\mathrm{a}), 0)$ $\mathrm{K}' = (-4\pi/(3\sqrt{3}\mathrm{a}), 0)$, by using vectors $\boldsymbol{v}_i$ it can be shown that the system gap is $\Delta = 2|M \mp \sqrt{3}t_2 \sin\phi|$. The gap thus depends on the mass term M and on the hopping parameter t_2. It follows that the Haldane model predicts the existence of different parameter regions in which the system behaves as an insulator, separated by a curve in the parameter space where gap closure occurs. In the vicinity of K′,K, crossing the curve of zero gap, the sign of $h_z(k)$ changes, as evident from Eq. (5.14). It is the mechanism of band inversion: the two gapped phases separated by the curve of zero gap are topologically distinct insulating phases, marked by the values of a topological invariant, i. e. the Chern number Ch. The different parameters regions corresponding to these insulating phase are depicted in Fig. 5.3b.

The topologically non-trivial insulating phase is characterized by $\mathrm{Ch} = \pm 1$, and it occurs for $-M_c < M < M_c$, where $M_c \equiv 3\sqrt{3}t_2 \sin\phi$. In all other cases $\mathrm{Ch} = 0$, and the system behaves as a trivial insulator. The particular nature of the problem can also be seen by observing that, if we restrict to the vicinity of the points K′,K, the Haldane Hamiltonian reduces to that of a massive Dirac fermion: if the Chern number

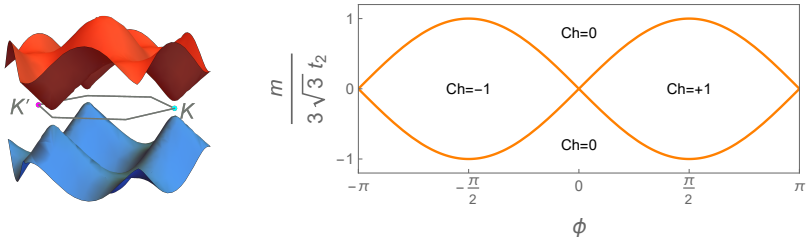

(a) (b)

Figure 5.3: Panel a: Plot of the two bands of the Haldane model in the gapped topological phase. Panel b : Phase diagram of the Haldane model in the plane $(\phi, m/(3\sqrt{3}t_2))$. The solid orange curve separates different topological phases (regions corresponding to different values of Ch). A topological transition can occur by crossing the line (gap closure).

is computed following Eq. (5.4), the results reads $\mathrm{Ch} = \frac{1}{2}\mathrm{sign}m$, where m is the mass term of the effective model [39]. It means that when the mass term changes sign by traversing the line of zero gap, we can only infer that $\Delta\mathrm{Ch} = 1$, but the exact value of the Ch can only be computed from the integral over the whole BZ. The eigenvectors corresponding to different bands can be written as

$$|k,-\rangle = \frac{1}{\sqrt{2(1+n_z)}}(n_x - in_y, -(n_z+1)) \tag{5.15}$$

$$|k,+\rangle = \frac{1}{\sqrt{2(1+n_z)}}(n_z+1, n_x+in_y) \tag{5.16}$$

where we indicate with $n_i = \frac{h_i(\boldsymbol{k})}{\|\boldsymbol{h}\|}$. We can also introduce the quasiparticle operator basis $\gamma_{k,\pm}$, which diagonalizes the Hamiltonian (5.8), i. e. $H_H = \sum_k (E_{k,-}\gamma^\dagger_{k,-}\gamma_{k,-} + E_{k,+}\gamma^\dagger_{k,+}\gamma_{k,+})$; these operators are linked to fermion operators by means of a unitary transformation

$$\gamma_{k,+} = \frac{1}{\sqrt{2(1+n_z)}}[(1+n_z)a_k + (n_x - in_y)b_k] \tag{5.17}$$

$$\gamma_{k,-} = \frac{1}{\sqrt{2(1+n_z)}}[(n_x + in_y)a_k - (1+n_z)b_k] \tag{5.18}$$

which clearly hold if $n_z \neq -1$, otherwise another expression for the operators has to be used.

5.2 TOPOLOGICAL INSULATORS

In the previous chapter, we have described the topological properties of Chern insulators as arising from TR symmetry breaking. If TR symmetry is restored, due to the structure of Dirac Hamiltonian, IQHE effect cannot occur. However, after the Kane and Mele (KM) seminal paper in 2005 [187], it has been proved that even in the presence

of TR symmetry nontrivial topological effect can occur. Indeed, TR symmetry gives rise to a different kind of topological phase, which has been called TR symmetry-protected topological state, i. e. a topological insulating state. In the following, our interest will be focused on the simplest prototypical model of topological insulator, namely the KM [187] model. It describes a 2D system of spinful fermions on a honeycomb lattice, where in place of the NNN hopping term a spin-orbit interaction is present. Spin-orbit interactions are a natural choice if a TR invariant Hamiltonian has to be written down. In its simplest formulation, the KM model assumes the form of a doubled Haldane model, each for the two different spin state. In this limit, it is equivalent to a doubled IQHE, with state of opposite spins described by different values of the Chern number. The striking signature of

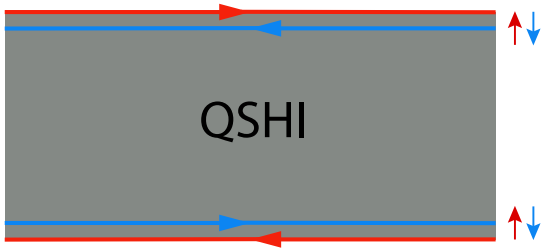

Figure 5.4: Schematic diagram of a 2D Quantum Spin Hall Insulator (QSHI). Adapted from [187].

topological properties described by KM model relies on the existence of odd number of pairs of gapless helical edge modes on each edge, as schematically depicted in Fig. 5.4. This phase is known as Quantum Spin Hall (QSH) effect. These edge modes are protected by TR symmetry, i. e. they cannot be gapped, only if they are an odd number of pairs for each edge, as a consequence of the Kramers theorem [39, 187]. The topological phase can be described by means of a $\mathbb{Z}_2$ invariant, which in analogy with the Chern insulator, distinguishes between a topologically trivial phase from QSH. In the following we will analyze only 2D systems, thus the invariant can be written as follows [191]

$$(-1)^{\nu} = \prod_{i=1}^{4} \delta(\Gamma_i) = \prod_{i=1}^{4} \frac{\mathrm{Pf}(w(\Gamma_i))}{\sqrt{w(\Gamma_i)}}. \tag{5.19}$$

Here $w_{\mathrm{nm}}(\boldsymbol{k}) = \langle n, -\boldsymbol{k}| \, T \, |m, \boldsymbol{k}\rangle$ is the expectation value of TR operator, i. e. $T = \exp(i\pi S_y)K$ on the occupied Bloch states, Γ_i are the TR points in the BZ of the considered system and the Pfaffian is defined from the determinant of matrix $w_{\mathrm{nm}}(\boldsymbol{k})$ as follows: $\mathrm{Pf}(w(\Gamma_i))^2 = \det\{w(\Gamma_i)\}$. Notice that, when computed in the TR points, the matrix $w_{\mathrm{nm}}(\boldsymbol{k})$ is antisymmetric. The topologically nontrivial QSH state is thus described by the value $\nu = 1$, while if $\nu = 0$ the system can be adiabatically connected to a trivial insulator. In the prototypical KM model, in the absence of Rashba spin-orbit term a topological transition between the two phases can take place only

by closing the gap [39]. In the presence of additional symmetries, Eq. (5.19) can be noticeably simplified [41, 191], and it will turn useful in the subsequent chapters.

5.2.1 The Kane-Mele model

The KM model [187, 188] describes spin-1/2 fermions on a honeycomb lattice, it is a prototypical model of QSH. Its general form reads

$$H_{KM} = H_{nn} + H_M + H_{SO} + H_R, \tag{5.20}$$

where H_{nn} is the usual NN hopping term, H_M is the on-site mass term as in the Haldane model, H_{SO} is the spin-orbit coupling energy and H_R is the Rashba coupling interaction. The last two contribution read respectively [41]

$$\begin{aligned} H_{SOC} &= -\sum_{\ll i,j \gg,\sigma,\sigma'} t_{so} c^\dagger_{i\sigma} \nu_{ij} (s_z)_{\sigma\sigma'} c_{j\sigma'} \\ H_R &= t_R \sum_{<i,j>} c^\dagger_i (\boldsymbol{s} \times \boldsymbol{d})_z c_j. \end{aligned} \tag{5.21}$$

Here $\nu_{ij} = (\boldsymbol{d_1} \times \boldsymbol{d_2})_z$, where $\boldsymbol{d_1}(\boldsymbol{d_2})$ are the two NN vectors which link the NNN sites i, j and $\boldsymbol{d}$ is a vector which links the NN sites; $c^\dagger_{i\sigma}(c_{i\sigma})$ are fermionic creation (annihilation) operators on the site i with spin σ, on the two sublattices (A, B); t_{so}, t_R are the strengths of the second nearest neighbor SOC term and the Rashba interaction, respectively. Below, we take into account only the SOC component term, thus disregarding Rashba-type terms (they break the spin symmetry and the spatial inversion symmetry), and we fix the mass term of the Haldane model to be zero. It follows that Eq. (5.20) can be described in terms of two copies of the Haldane model, one for each value of the spin along $\hat{z}$ axis, with additional Rashba SOC term. Then the KM Hamiltonian can be written as follows

$$H_{KM} = -t_1 \sum_{<i,j>,\sigma} c^\dagger_{i\sigma} c_{j\sigma} - \sum_{\ll i,j \gg,\sigma} t_{so} e^{i\xi_{i\sigma}\phi} c^\dagger_{i\sigma} c_{j\sigma}, \tag{5.22}$$

where t_1 is the nearest-neighbor hopping element, $\xi_{i\sigma} = \pm 1(\mp 1)$ for hopping on the sublattice sites A, (B) and spin-$\uparrow$ (spin-$\downarrow$) respectively. As evident from Eq. (5.22), the phase choice in the SOC term ensures that the net magnetic flux through the honeycomb is zero. However, due to the fact that the phases for different spin values are complex-conjugate of each other, the SOC term can open a gap in the high-symmetry points of the first Brillouin zone (BZ) of the honeycomb lattice without breaking TR symmetry. In what follows, we restrict to the case of particle-hole symmetry, i. e. we take $\phi = \pi/2$ and fix the chemical potential to be zero. The KM model can be rewritten in the quasi-momentum space, introducing creation (annihilation) fermionic operator $(a_{k\sigma}, b_{k\sigma})$ on each sublattice

$$H_{KM} = \sum_k \Psi^\dagger_k \mathcal{H}(\boldsymbol{k}) \Psi_k, \tag{5.23}$$

with $\Psi_k^\dagger = (a_{k\uparrow}^\dagger, b_{k\uparrow}^\dagger, a_{k\downarrow}^\dagger, b_{k\downarrow}^\dagger)$ and $\mathcal{H}(\boldsymbol{k})$ denotes the four-dimensional matrix

$$\mathcal{H}(\boldsymbol{k}) = \boldsymbol{h}(\boldsymbol{k}) \cdot \boldsymbol{\sigma} \mathbb{1}_{\sigma\sigma'} + h_{so}(\boldsymbol{k}) \sigma_z (s_z)_{\sigma\sigma'}, \tag{5.24}$$

where s_z is the spin operator along $\hat{z}$. As usual, we denote with $\boldsymbol{\sigma} = \sigma_i, i = x, y, z$ Pauli matrices, and the quasi-momentum $\boldsymbol{k} = (k_x, k_y)$ belongs to BZ. The vector $\boldsymbol{h}(\boldsymbol{k})$ is generally analogous to a 3D magnetic field, $\boldsymbol{h}(\boldsymbol{k}) = (h_x(\boldsymbol{k}), h_y(\boldsymbol{k}), h_z(\boldsymbol{k}))$; in the presence of inversion symmetry, the field component along $\hat{z}$ vanishes. The matrices $(\mathbb{1}, s_z)$ act on the space of the spin degree of freedom. The 4D Hamiltonian $\mathcal{H}(\boldsymbol{k})$, which is invariant under TR and inversion symmetry, can be written as a linear combination of 5 out of the 15 SU(4) matrices, i. e. $\Gamma_\alpha = (\sigma_x \mathbb{1}, \sigma_y \mathbb{1}, \sigma_z s_x, \sigma_z s_y, \sigma_z s_z)$ [39, 41, 191]. It can be readily diagonalized, through a unitary transformation, to give : $\mathcal{H}(\boldsymbol{k}) = E_{k,-} \sum_\sigma \gamma_{k,-,\sigma}^\dagger \gamma_{k,-,\sigma} + E_{k,+} \sum_\sigma \gamma_{k,+,\sigma}^\dagger \gamma_{k,+,\sigma}$, where $\gamma_{k,\pm,\sigma}$ denote quasi-particle creation (annihilation) operators and

$$E_{k,\pm} = \sqrt{h_{so}^2(\boldsymbol{k}) + h_x^2(\boldsymbol{k}) + h_y^2(\boldsymbol{k})}, \tag{5.25}$$

are the two-fold degenerate quasi-particles energy bands. The SOC term, which is $\propto \Gamma_5$, opens a gap at Dirac points K, K'. Notice that a small value of SOC is sufficient to open a gap at the high symmetry points. As long as the gap is open, the topological phases of KM can be classified according to the values of $\mathbb{Z}_2$ invariant. In the case of inversion symmetry, which is also the case of Eq. (5.24), it has been shown that using the properties of the parity operator $\mathcal{P} = \sigma_x \otimes \mathbb{1}$, the $\mathbb{Z}_2$ invariant in Eq. (5.19) can be reduced to

$$(-1)^\nu = \prod_{i=1}^{4} \delta(\Gamma_i), \; \delta(\Gamma_i) = -\mathrm{sign}(h_x(\Gamma_i)). \tag{5.26}$$

It follows that when the gap is open, the invariant in Eq. 5.26 gives exactly $\nu = 1$. The TR points Γ_i can be taken as $\Gamma = n_1 \mathrm{b}_1 + n_2 \mathrm{b}_2$,

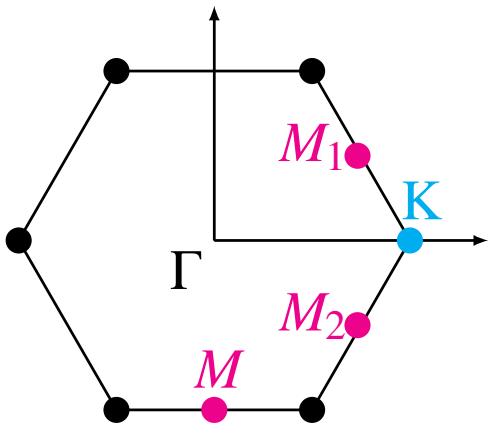

Figure 5.5: BZ of the honeycomb lattice and TR points.

where (b_1, b_2) are the primitive vectors of the reciprocal lattice. In the case of the honeycomb lattice, it can be easily found that these points correspond to the M points of BZ and the point Γ as in Fig. 5.5.

5.3 BAND INVARIANTS IN THE PRESENCE OF INTERACTIONS

It is sensible to conclude this chapter with a quick overview on the computation of band invariants. In the single-particle context, band invariants have succesfully been defined to describe different topological phases. However, in the presence of interactions a band theory cannot describe the physics of the system, so that the invariants have to be reformulated. We will adopt the approach followed by [204, 205], where an expression for the band invariants in the presence of interactions,e. g.Coulomb interactions is derived, starting from the Green function of the interacting system. The first step is the computation of the eigenvectors of the inverse Green function written in the momentum space and $G^{-1}(\mathrm{i}\omega, k)$

$$G^{-1}(\mathrm{i}\omega, k)\,|n(\mathrm{i}\omega, k)\rangle = \mu_n((\mathrm{i}\omega, k))\,|n(\mathrm{i}\omega, k)\rangle\,. \tag{5.27}$$

It can be shown that

$$G^{-1\dagger}(\mathrm{i}\omega, k) = G^{-1}(-\mathrm{i}\omega, k), \tag{5.28}$$

so that exactly at $\omega = 0$ the Green function is a Hermitian matrix. It follows that not only the eigenvalues are real, but the eigenvectors corresponding to different eigenvalues belong to orthogonal subspaces. Given that the eigenvectors of G and G^{-1} are the same, the straetegy is based on finding the eigenvectors of the zero-frequency Green functions. These eigenvectors $|n(0, k)\rangle$ can be classified according to the signs of their eigenvalues $\mu_n(0, k)$. Eigenvectors corresponding to positive eigenvalues are necessarily orthogonal to those corresponding to the negative ones. It means that a subspace R(L) can be identified, which is spanned by the collection of all $|n(0, k)\rangle$ corresponding to different k, and having negative(positive) eigenvalues. All the eigenvectors in R are orthogonal to those in L. This is sufficient for defining a band invariant which can be written in terms of a a kind of Berry potential

$$A_i(\boldsymbol{k}) = -i \sum_{n \in \text{R space}} \langle n, k|\, \frac{\partial}{\partial k_i}\, |n, k\rangle\,, \tag{5.29}$$

where the Bloch states are replaced with the many-body states belonging to the R space. Thus it is possible to define the invariant in the interacting case as the integral of the curvature related to the previous potential, in the same way as with (5.2). The main difference is that for every k the bundle is composed by all the eigenvectors

of R space. In this way, the major complexity in the computation of topological invariants in the presence of interactions resides only in the computation of the interacting Green function at $\omega = 0$ and in its diagonalization. The Chern number in the interacting case can be directly computed following this route. Notice that this method cannot work in the presence of nontrivial ground state degeneracies, as in FQHE. However, it has been proved to be totally equivalent to the rather more complicated field-theoretical formulation [208]. Besides Chern number, also $\mathbb{Z}_2$ invariants can be generalized to the interacting case by employing this method. In the following chapters, we will compute the invariants following this technique.

6 E-PH AND TOPOLOGICAL TRANSITION IN THE HALDANE CHERN INSULATOR

In this chapter we present part of our original contributions published in [209].

In the previous chapter, we introduced the properties of prototypical models of topological insulators. Below, we focus on Haldane model of Chern insulator (see Sec. 5.1.1), and we investigate the effects on the topological properties of the system when the spinless fermions couple to the lattice degrees of freedom.

The study of topological properties in the presence of correlations has been the focus of recent research. In general, the most of theoretical work has been done aimed at understanding the effect of Coulomb correlations on the topological properties [41, 210–215]. On the other hand, electron-phonon interaction is so inevitably present in any solid that, from the first principles, one cannot even distinguish and separate Coulomb and electron-phonon interaction because they are unambiguously connected [216]. The issue of Coulomb correlations has been thoroughly studied in the last decade, and the main properties of the phase diagrams are already known. Current studies are mainly focused on improving the reliability of the physical description, by the use of more refined numerical approaches, see e. g. [215]. On the other hand, there are only few studies of the influence of electron-phonon coupling (EPC) [217, 218] all considering models different from Haldane Chern insulator. To fill this gap, we account for the lattice quantum dynamics including on-site optical phonons coupled *a la* Holstein to spinless fermions, described by the Haldane model. We perform a numerical study of the bulk properties of the interacting system, employing Cluster Pertubation Theory (CPT) [48], that, starting from the exact numerical computation of the Green function, performed on a suitably chosen cluster, allows us to compute the interacting Green functions of the whole lattice, an experimentally accessible function through angle resolved photoemission spectroscopy measurements [219].

We find evidence of a topological phase transition driven by EPC. Starting from the topological phase in the bare Haldane model, we show that the increasing of the strength of the EPC drives the system towards a trivial insulator. Across the phase transition, a strong hybridization of the quasiparticle bands of the bare Haldane model occurs. Numerical simulations show also that the renormalized phonon propagator exhibits a two peak structure across the quantum transi-

tion, whereas, in absence of the mass term, there is indication of a complete softening of the effective vibrational mode signaling a CDW instability.

6.1 THE INTERACTING HALDANE MODEL

We add to the Haldane Hamiltonian described by Eq. (5.7) an interaction term typical of the Holstein model, where charge fluctuations are linearly coupled to the displacement of local lattice vibrations

$$H = H_H + \omega_0 \sum_i d_i^\dagger d_i + g\omega_0 \sum_i (c_i^\dagger c_i - \frac{1}{2})(d_i^\dagger + d_i). \tag{6.1}$$

We employ shorthand notation $d_i^\dagger (d_i)$ for two different bosonic operators, which respectively create (annihilate) a phonon on the two (A, B) sublattice sites, ω_0 is the optical mode frequency, and g represents the strength of the coupling with lattice. We introduce also the dimensionless parameter $\lambda = g^2\omega_0/4t_1$. Here we restrict our attention to the case of half-filling, i.e. $\sum_{i\in A} a_i^\dagger a_i + \sum_{i\in B} b_i^\dagger b_i = N_c = N/2$, where N_c (N) is the number of unit cells (lattice sites). In what follows, we present different approaches which can be employed to understand the physics behind Eq. (6.1).

6.2 LANG-FIRSOV APPROACH

If the optical mode frequency is the highest energy scale (antiadiabatic regime), i.e. $\omega_0 \gg t_1, t_2, M$, the physics is well captured by the Lang-Firsov approach (LFA) [220], that is based on the unitary transformation:

$$\tilde{H} = e^S H e^{-S} \tag{6.2}$$

where $S = g\sum_i (c_i^\dagger c_i - \frac{1}{2})(d_i^\dagger - d_i)$. In the new basis, the electronic hopping is assisted by phononic operators that, in the antiadiabatic regime, can be treated as a small perturbation. This approximation leads to renormalized values of t_1 and t_2 through the factor $e^{-\frac{4\lambda t_1}{\omega_0}}$. On the other hand, as it is straightforward to verify, the value of M is not affected by the unitary transformation. The net result is that it is possible to replace the Hamiltonian $\tilde{H}$ with that of an effective Haldane model, where now the parameters, and then the topological-trivial insulator transition, are controlled by the strength of the EPC. In other words, by increasing the value of λ, it is possible to induce a topological quantum transition. On the other hand, this approach becomes exact only in the limit $t_1 = t_2 = 0$. In order to investigate if these effects survive for parameter values of physical interest, a more accurate treatment of EPC is needed. To this aim we employ

the CPT (see Sec. 6.3), that allows us to compute the electronic Green function, $G_{i,j}(\boldsymbol{q}, z)$, of the interacting system, from which detailed informations on the renormalized band structure as well as spectral functions can be derived. Here i stands for (A, B), i.e. indicates the two sublattices, and $z = \omega + i\eta$ lies in the complex upper half plane. Starting from $G_{i,j}$, it is straightforward to derive the Green functions $G_{(+,+)}$ and $G_{(-,-)}$, corresponding to the quasiparticle operators of the bare Haldane model. We will focus our attention on the following set of parameters: $t_2/t_1 = 0.3$, $\omega_0 = 3t_1$, $\phi = \frac{\pi}{2}$ and two different values of M, i.e. $M_1 = 0.94M_c$ and $M_2 = 0.42M_c$. In the absence of EPC, these two values describe the topological insulator phase near and far from, respectively, the transition towards to a trivial insulator. Furthermore, for these values of the parameters, the lowest gap is located at K point, and H_H exhibits hole-particle symmetry so that $\mu = 0$.

6.3 CLUSTER PERTURBATION THEORY

We employ the Cluster Perturbation Technique (CPT) [48] in order to compute the Green functions of the interacting system described in Eq. (6.1); the general expression for the Green function can be written as

$$\mathcal{G}_{ij}(\omega) = \mathcal{G}^{+}_{ij}(\omega) + \mathcal{G}^{-}_{ij}(\omega), \tag{6.3}$$

where

$$\begin{aligned} \mathcal{G}^{+}_{ij}(\omega) &= \langle \psi_0 |\, c_i (\omega - H + E_0)^{-1} c_j^{\dagger} \,| \psi_0 \rangle \\ \mathcal{G}^{-}_{ij}(\omega) &= \langle \psi_0 |\, c_i^{\dagger} (\omega + H - E_0)^{-1} c_j \,| \psi_0 \rangle \,. \end{aligned} \tag{6.4}$$

$|\psi_0\rangle$ is the ground state of H, and E_0 is the corresponding ground state energy.

The numerical method is based on the division of the lattice in identical clusters containing a finite number N_c of sites. As a consequence, each cluster can be interpreted as a site of a superlattice. The Hamiltonian of the full system can thus be rewritten as a sum of a cluster Hamiltonian and an interaction term which links inter-cluster sites

$$H = H_c + V_{ic} \tag{6.5}$$

where V_{ic} is a one-body operator. The Fourier transform of the Green function (6.3) over the whole superlattice can be written as

$$\mathcal{G}^{-1}(\boldsymbol{K}, \omega) = \mathcal{G}_c^{-1}(\omega) + \mathcal{V}_{ic}(\boldsymbol{K}) \tag{6.6}$$

where $\boldsymbol{K}$ is the reduced wave-vector belonging to the first Brillouin zone of the superlattice, and $\mathcal{G}_c$ is the Green function of the cluster, which is independent of $\boldsymbol{K}$; $\mathcal{V}_{ic}(\boldsymbol{K})$ is the Fourier transform of the inter-cluster term, that is diagonal in $\boldsymbol{K}$. The advantages of using this method for interacting Hamiltonians of the form reported in Eq. (6.1) are clear: if the interactions can be modeled by means of local

fermionic operator, like the electronic occupation on each site of the lattice, the computation of the whole Green function of the bulk system is reduced to the numerical computation of $\mathcal{G}_c$ on the cluster chosen. Several numerical reduction techniques, like Lanczos algorithm, allow to perform an efficient diagonalization of the matrix describing the cluster, when the number of cluster's sites grows. Moreover, exploiting the superlattice properties, each wavevector in the original lattice Brillouin zone can be uniquely written in terms of the reciprocal superlattice wavevector $\boldsymbol{K}_r$, i.e. $\boldsymbol{k} = \boldsymbol{K}_r + \boldsymbol{K}$; it follows that, by imposing periodic boundary conditions, the Green function in the bulk of the system can be computed.

Below, we make the simple choice of a two-sites cluster containing the lattice basis, i. e. a couple of nearest-neighbor sites, respectively of type A and B displaced along a single bond of the Graphene lattice.

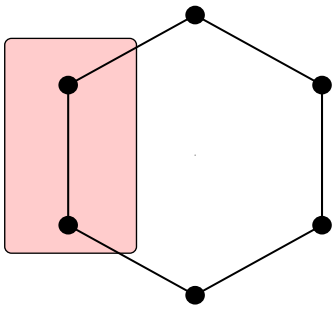

Figure 6.1: Schematic diagram of the cluster adopted to compute the $\mathcal{G}_c$: it contatins two NN sites of type A and B.

Adopting a truncation of the Hilbert space of bosonic field, the cluster Hamiltonian can be directly diagonalized, and the function $\mathcal{G}_c$ is readily computed. Due to the simple structure of the problem, the analytic form of $\mathcal{V}_{ic}(\boldsymbol{K})$ can be straightforwardly computed for each couple of sites belonging to different sublattices.

We thus can efficiently compute the Green functions in Eq. (6.3) related to each sublattice fermionic operator, i. e. $c_k = (a_k, b_k)$, along with the Green functions for the quasi-particle operators $(\gamma_{k_+}, \gamma_{k_-})$ of the single-particle Haldane model in the presence of interactions. From each Green function, the computation of the spectral functions can be performed

$$A(\boldsymbol{k}, \omega) = -\frac{1}{\pi} \operatorname{Im}\{\mathcal{G}(\boldsymbol{k}, \omega)\} \tag{6.7}$$

Furthermore, the Density of States (DOS) of the interacting model can also be computed from the spectral function

$$\rho(\omega) = \frac{1}{N_c} \sum_k A(\boldsymbol{k}, \omega) \tag{6.8}$$

Thus, we can directly analyze the change in the spectral properties of the system in the presence of interactions, e. g. the lower band spectral

function $A_{(-,-)}(\boldsymbol{k},\omega)$ around the Dirac points K, K′. Eventually, every moment of the spectral functions $A(\boldsymbol{k},\omega)$ can be computed, e. g. the occupation of a given fermionic band reading

$$n_k = \int_{-\infty}^{+\infty} A(\boldsymbol{k},\omega) n_F(\omega) d\omega \tag{6.9}$$

This numerical approach can thus provide useful information on the effect of interactions on the topological properties of Chern insulators.

6.4 RESULTS

Within the hole sector, near K point, we followed the dispersion of lowest energy quasiparticle peak associated to one of the two spectral weight functions $A_{(\mp,\mp)}(\boldsymbol{q},\omega) = -\operatorname{Im}\left\{G_{(\mp,\mp)}(\boldsymbol{q},z)\right\}/\pi$. It turns out to be equivalent to that of an effective Haldane model. In Fig. 6.2a

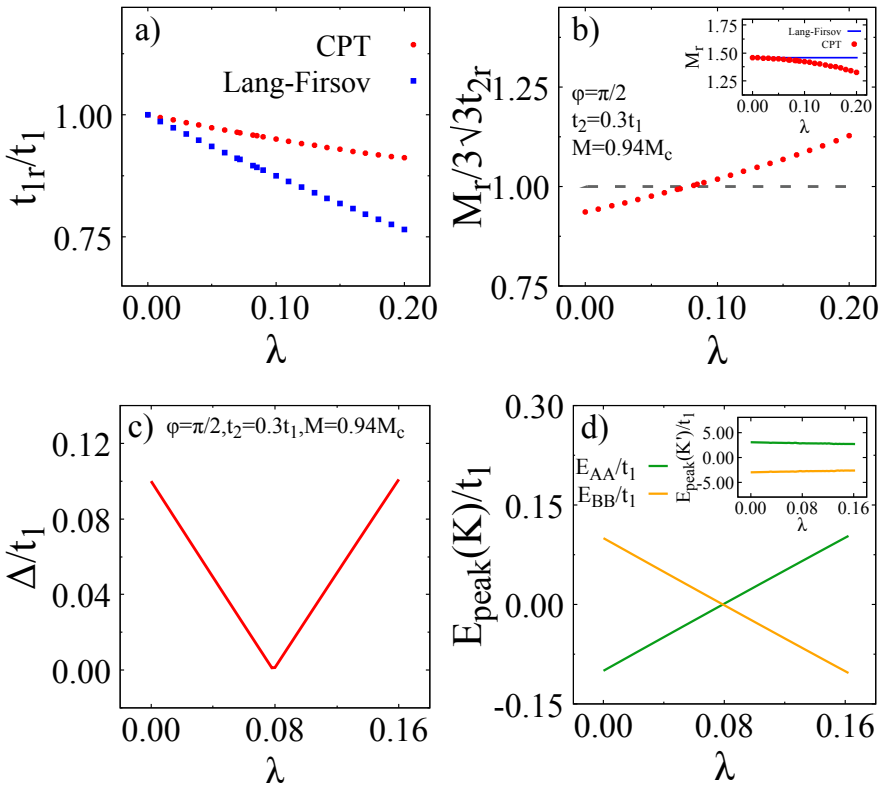

Figure 6.2: (a) and (b): parameters of the effective Haldane model vs λ; (c) and (d): behavior of the gap and the energies of the peaks of $A_{(A,A)}$ and $A_{(B,B)}$, at K and K′, as function of λ.

and Fig. 6.2b we plot, as function of the interaction strength λ, the renormalized values of the electronic hopping and M, i.e. t_{1r}, t_{2r} and M_r, and compare them with those predicted within LFA. In the CPT all the parameters, including M, are renormalized, but, also in this

approach, a topological quantum transition occurs. Indeed, around $\lambda_c \simeq 0.08$, the ratio $M_r/(3\sqrt{3}t_{2r})$ becomes greater than 1, signaling the phase transition. Fig. 6.2c shows that the gap, by increasing λ, first decreases, at λ_c becomes zero, and then increases. It is also worth noting that, within the bare Haldane model, the spectral weight functions corresponding to the two sublattices assume the following form: $A_{(A,A)}(\boldsymbol{q},\omega) = \frac{(1+n_z)}{2}\delta(\omega - E_{q,+}) + \frac{(1-n_z)}{2}\delta(\omega - E_{q,-})$ and $A_{(B,B)}(\boldsymbol{q},\omega) = \frac{(1-n_z)}{2}\delta(\omega - E_{q,+}) + \frac{(1+n_z)}{2}\delta(\omega - E_{q,-})$, where $n_z = \frac{h_z}{\|\boldsymbol{h}\|}$. Here $\delta(\omega)$ is the Dirac delta function. On the other hand, we emphasize that, again at $\lambda = 0$, if the system is in the topological phase $0 < M < M_c$, n_z, when evaluated at K and K′, assumes opposite values, respectively -1 and 1, whereas, in the trivial insulating phase ($M > M_c$), $n_z = 1$ at both K and K′. Then, at $\lambda = 0$, it is clear that $A_{(A,A)}(\mathrm{K},\omega)$ ($A_{(B,B)}(\mathrm{K},\omega)$) is peaked only at $E_{\mathrm{K},-}$ ($E_{\mathrm{K},+}$) in the topological phase and only at $E_{\mathrm{K},+}$ ($E_{\mathrm{K},-}$) in the trivial insulating phase. On the other hand, $A_{(A,A)}(\mathrm{K}',\omega)$ ($A_{(B,B)}(\mathrm{K}',\omega)$) has spectral weight different from zero only at $E_{\mathrm{K}',+}$ ($E_{\mathrm{K}',-}$), independently on the phase. We followed, as function of λ, the peak position of these two spectral functions at both K and K′. Fig. 6.2d shows that at $\lambda < \lambda_c$ ($\lambda > \lambda_c$) the behavior of the fermions on the two sublattices is in agreement with that predicted by the bare Haldane model in the topological (trivial) insulating phase. It confirms that at λ_c a quantum transition occurs.

Now we focus our attention on the spectral weight functions corresponding to the operators describing the quasiparticles in the bare Haldane model, i.e. $A_{(-,-)}$ and $A_{(+,+)}$. These two functions, at the Dirac point K, are plotted in Fig. 6.3a and Fig. 6.3b for two different values of λ, $\lambda = 0.075$ and $\lambda = 0.085$, respectively before and after the topological phase transition. Crossing λ_c, the energy gap closes and opens again, and, at the same time, the character of the two bands changes, i.e. the peak of $A_{(-,-)}$ ($A_{(+,+)}$) is located above (below) the chemical potential. The plots (Fig. 6.3c and Fig. 6.3d) of the density of states associated to the two bands, $DOS_{(-,-)}(\omega) = \frac{1}{N_c}\sum_q A_{(-,-)}(\boldsymbol{q},\omega)$ and $DOS_{(+,+)}(\omega) = \frac{1}{N_c}\sum_q A_{(+,+)}(\boldsymbol{q},\omega)$, furtherly clarify this picture. Indeed $DOS_{(-,-)}$ ($DOS_{(+,+)}$) (see the two insets) exhibits a peak above (below) μ, at $\lambda > \lambda_c$. It indicates a strong hybridization between the quasiparticles of the bare Haldane model across the topological quantum transition. In the density of states, the Van Hove singularities and the satellite bands, stemming from the EPC, are clearly distinguishable.

In Fig. 6.4a we plot the average number of fermions $n_{(-,-)}(\boldsymbol{q})$, at $\boldsymbol{q} = \mathrm{K}$, as function of λ: $n_{(-,-)}(\boldsymbol{q}) = \int_{-\infty}^{\infty} A_{(-,-)}(\boldsymbol{q},\omega) n_F(\omega) d\omega$, where $n_F(\omega)$ is the Fermi function. By decreasing the broadening factor η, it becomes more and more clear that $n_{(-,-)}(\mathrm{K})$ exhibits a finite discontinuity at the transition point, so that it can be used as direct indicator of the topological quantum transition. We find also (Fig. 6.4c) that a greater EPC is needed to destroy the topological phase when the initial parameters of the bare Haldane model are such

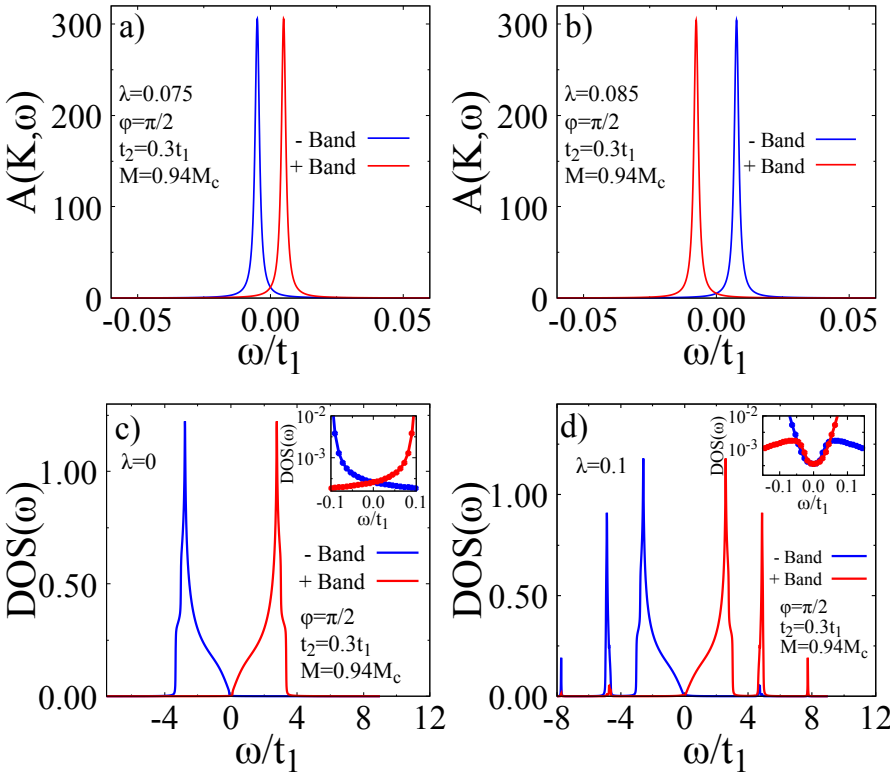

Figure 6.3: (a) and (b): $A_{(-,-)}$ and $A_{(+,+)}$, at K, just below and above λ_c; (c) and (d): density of states with zoom (insets) around μ ($\omega = 0$), at $\lambda = 0$ and $\lambda > \lambda_c$.

that spinless fermions are well inside the topological phase. In this case the discontinuity at the transition point reduces indicating the presence of strong electron-electron correlations induced by the EPC. The plots in Fig. 6.4b and Fig. 6.4d, i.e the behavior, across the phase transition, of $n_{(-,-)}(\boldsymbol{q})$ along the line $\mathrm{K}' - \Gamma - \mathrm{K}$, point out that the quantum transition affects only a small region of the Brillouin zone around the Dirac point K.

The occurrence of the topological phase transition is further verified by means of the computation of the interacting Chern number Ch (see Sec. 5.3), which we report as a function of the coupling strength λ in the inset of Fig. 6.4, panel a. Here we show that exactly at the critical coupling strength λ_c, *Ch* drops from 1 to 0, signaling the transition from topological to trivial phase.

Finally, we investigate the effects of the quantum transition on the lattice. To this aim, we emphasize that the exact integration of the phonon degrees of freedom, through path integral technique, leads to a retarded electron-electron interaction on the same sublattice. This coupling is controlled by the bare phonon propagator, $D^0(\boldsymbol{q}, z) = \frac{1}{z-\omega_0} - \frac{1}{z+\omega_0}$, and the charge-phonon vertex: $V^0_{i,i}(\boldsymbol{q}, z) = \frac{g^2\omega_0^2}{N_c} D^0(\boldsymbol{q}, z)$ [220, 221]. At the lowest order in the EPC, there is no coupling between

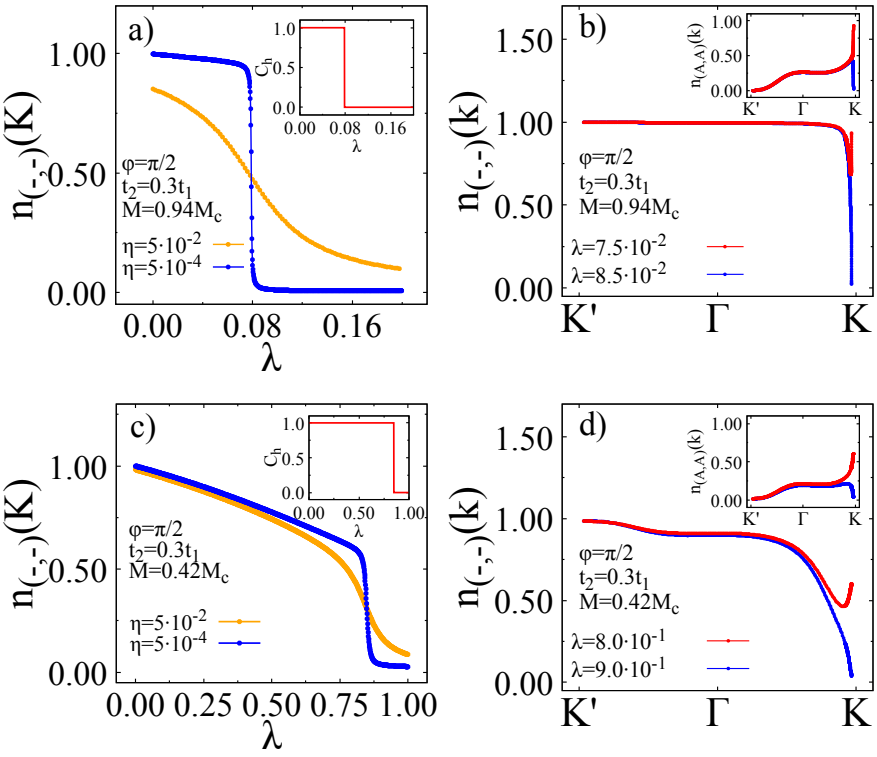

Figure 6.4: The average number of fermions $n_{(-,-)}$, at K ((a) and (c)) and along $K' - \Gamma - K$ ((b) and (d), in the inset $n_{(A,A)}$), for two different values of M.

two electrons on different sublattices, i.e. $V^0_{(A,B)}(\boldsymbol{q}, z) = 0$. On the other hand, the effective interaction between two charge carriers obeys the Dyson equation [220, 221]:

$$V^{eff}_{i,j}(\boldsymbol{q}, z) = V^0_{i,j}(\boldsymbol{q}, z) + V^0_{i,h}(\boldsymbol{q}, z)\Pi^*_{h,k}(\boldsymbol{q}, z\ )V^{eff}_{k,j}(\boldsymbol{q}, z),$$

which defines the proper polarization insertion $\Pi^*_{i,j}(\boldsymbol{q}, z)$. Since $\Pi^*_{i,j}$, in general, is a non diagonal matrix, there is an effective phonon mediated interaction even between two charge carriers located in different sublattices. At the lowest order $\Pi^*_{i,j}(\boldsymbol{q}, z)$ is the particle-hole bubble. The next step is to replace, in this lowest order diagram, the unperturbed electron Green functions with the interacting Green functions calculated within the CPT. This procedure allows to obtain the effective interaction between two electrons and, then, the renormalized phonon propagator $D_{i,j}$.

We focus our attention on the spectral weight function $B_{(A,A)}(\boldsymbol{q}, \omega) = -\frac{\mathrm{Im}\{D_{(A,A)}\}(\boldsymbol{q},z)}{\pi}$, an odd function, that, in the absence of EPC, is peaked at $\omega = \omega_0$. At $\lambda \neq 0$, it exhibits a softening at $\boldsymbol{q_c}$ around $\frac{\boldsymbol{b_1}}{2}$ and $\frac{\boldsymbol{b_2}}{2}$, where $\boldsymbol{b_1}$ and $\boldsymbol{b_2}$ are the primitive vectors of the reciprocal lattice. In Fig. 6.5 we plot $B_{(A,A)}(\boldsymbol{q_c}, \omega)$ for four different values of the EPC. Near the topological phase transition there is a splitting of the main peak.

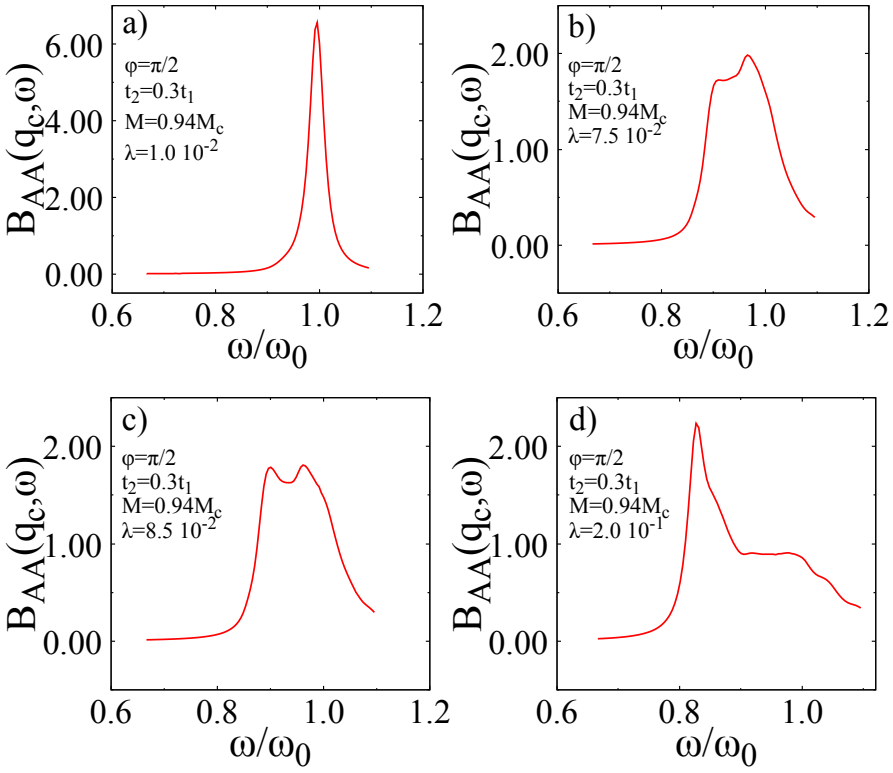

Figure 6.5: Phonon spectral weight function for four different values of λ.

By increasing λ, the spectral weight of the lowest (highest) energy peak increases (decreases), and, around λ_c, the two peaks have the same intensity. We emphasize that the energy of the lowest peak is strictly related to the energy difference between the two Dirac points, both in the hole and particle sectors (compare energy of K and K′ in Fig. 6.2d and its inset), i. e. K and K′ are connected by the EPC. On the other hand, the highest energy peak is reminiscent of the bare phonon frequency.

Finally, at $M = 0$, by increasing EPC, the peak softening becomes more and more pronounced signaling a CDW. We can investigate the tendency of the system towards a CDW instability as follows. The dynamical effective interaction between two charge carriers obeys the Dyson equation in Eq. (6.10). It follows that

$$V^{eff} = (\mathbb{1} - V^0 \Pi^*)^{-1} V^0. \tag{6.10}$$

The evaluation of the function $P = (\mathbb{1} - V^0\Pi^*)^{-1}$ provides information on the stability of the system. In particular a divergence of this quantity, at $\omega = 0$, signals the occurency of a CDW instability. Indeed one can immediately recognize that it implies a diverging response of the boson propagator, of the scattering amplitude mediated by the same boson propagator and the density-density correlation function. The numerical simulations show that $P(\boldsymbol{q} \to 0, \omega = 0)$ exhibits a divergence at $\lambda_c \simeq 0.877$, in the four channels (A, A) (see Fig. 6.6a),

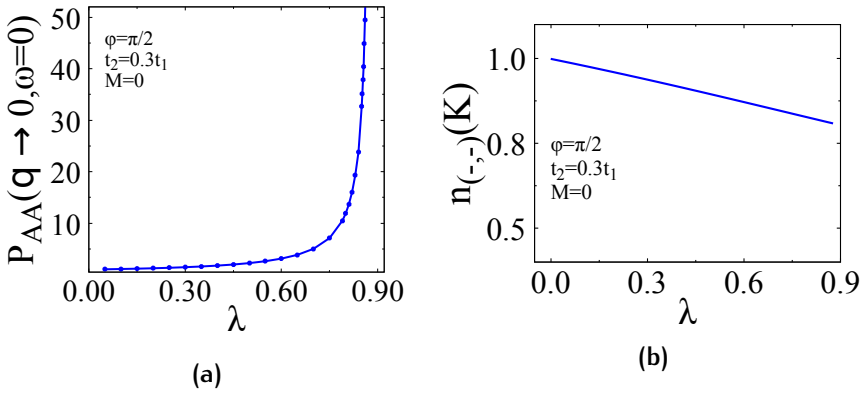

Figure 6.6: Panel a: correlation function $P_{A,A}(\boldsymbol{q} \to 0, \omega = 0)$ plotted vs λ, for fixed band-model parameters: $\phi = \pi/2$, $t_3 = 0.3t_1$, $M = 0$. Panel b: Average number of fermions $n_{(-,-)}$ computed in the K point as a function of λ, and fixed band-model parameters $\phi = \pi/2$, $t_3 = 0.3t_1$, $M = 0$.

(B, B), (A, B) and (B, A), signaling a charge density wave within the unit cell. On the other hand, the average number of fermions at K point, plotted as a function of λ in Fig. 6.6b, in this parameter region, $\lambda \leq \lambda_c$, don't exhibit a rapid drop as shown in 6.4. It follows that we don't observe a gap closing and reopening, as in Fig. 6.2 [209]. In conclusion, at $M = 0$, the system does not exhibit any topological transition, but only a tendency towards a charge density wave instability, that sets in before the gap closing.

6.5 CONCLUSIONS

We have investigated the effects of the interaction between the vibrational modes of the lattice and the spinless charge carriers in the Haldane model on a honeycomb lattice. We found evidence of a topological quantum transition. Starting from the topological phase in the bare Haldane model, the increasing of the strength of the EPC, λ, drives the system towards a trivial insulator. By varying λ, the energy gap first decreases, closes at the transition point, and then increases. Across the transition point, a strong hybridization between the quasiparticles of the bare Haldane model occurs near the Dirac point characterized by the lowest gap. The average number of fermions exhibits a finite discontinuity at the transition in this particular point of the Brillouin zone and can be used as direct indicator of the topological quantum transition. We have also shown that the renormalized phonon propagator exhibits a two peak structure across the quantum transition, whereas, in absence of the mass term, there is indication of a complete softening of the effective vibrational mode signaling a charge density wave instability.

7 E-PH AND TOPOLOGICAL TRANSITION IN THE QSH SYSTEM.

In this chapter we present part of our original contributions published in [222].

Below, we extend the study of the previous chapter by taking into account the effect of EPC on the topological properties of the KM model of a QSH band insulator. Although KM model describes spin 1/2 fermions in the presence of a hopping contribution, an intrinsic spin-orbit coupling (SOC) term, and an additional Rashba SOC on a half-filled honeycomb lattice [187, 188], in this paper we consider the Rashba spin-orbit interaction to be zero.

As explained in Sec. 5.2.1, the Hamiltonian can be obtained by considering two copies of the model introduced earlier by Haldane [140], where the second-nearest neighbor hoppings for spin-$\uparrow$ and -$\downarrow$ electrons are complex valued and complex conjugate to each other. We will focus our attention on the case where next-nearest-neighbor spin-orbit hopping integral is purely imaginary, i.e. in the presence of the particle-hole symmetry. As in the previous chapter, we describe the lattice dynamics by introducing on-site optical modes, coupled to fermions by means Holstein-type interaction term.

We compute the single particle Green's propagator in the thermodynamic limit by using the CPT. We choose the model parameter values such that the minimal gap of the bare topological insulator is located at the two inequivalent Dirac points of the Graphene, K and K$'$. We show that EPC induces a topological-trivial quantum phase transition through a gap closing and reopening in the M point of the Brillouin zone.

By following Wang et al. [204, 205] we compute the topological invariant via the parity eigenvalues of the fully interacting Green's function obtained at the time-reversal invariant momenta and zero energy. The numerical simulations show that, by varying the strenght of EPC, the $\mathbb{Z}_2$ invariant drops from one to zero just where the gap closes. Here a strong hybridization between the two bare quasiparticle bands of the KM model occurs. We show also that, in analogy to the previous chapter, the average number of fermions at the M point of the Brillouin zone can be used as a specific indicator of the quantum phase transition. Furthermore, a splitting and a softening of the phonon Green's function are observed around the topological transition; eventually, we show that many kinks in the electron

renormalized dispersion appear as direct consequence of the coupling between the charges and the lattice boson mode.

7.1 THE INTERACTING KM MODEL

We aim at describing the effects of the EPC on the topological properties of KM model (5.22). Following the previous chapter, we introduce the EPC by means of the Holstein model, which linearly couples the charge fluctuations to the displacement of on-site lattice vibrations:

$$H = H_{KM} + \omega_0 \sum_i d_i^\dagger d_i + g\omega_0 \sum_i (n_i - 1)(d_i^\dagger + d_i) \tag{7.1}$$

We employ shorthand notation $d_i^\dagger(d_i)$ for two different bosonic operators, which respectively create (annihilate) a phonon on the two (A, B) sublattice sites, n_i indicates the electron number operator on the site i, ω_0 is the optical mode frequency, and g represents the strength of the coupling with lattice. We introduce also the dimensionless parameter $\lambda = g^2\omega_0/4t_1$. Here we restrict our attention to the case of half-filling, i.e. $\sum_{i\in A} a_i^\dagger a_i + \sum_{i\in B} b_i^\dagger b_i = 2N_c = N$, where N_c (N) is the number of unit cells (lattice sites). We choose $t_1 = 1$, $\omega_0 = 0.1$, $t_{so} = 0.1$, and use units such that $\hbar = 1$.

7.2 RESULTS

The single particle Green's function $\boldsymbol{G}_\sigma(\boldsymbol{k}, z)$, where $z = \omega + i\eta$ lies in the complex upper half plane, is obtained by using the CPT. Due to the explicit s_z conservation of the Hamiltonian, the Green's function is block-diagonal in spin-space, and, furthermore, $\boldsymbol{G}_\sigma$ is a 2x2 matrix in the (A, B) sublattice basis. We emphasize that this does not mean that up and down spin electrons are decoupled. Indeed they interact with each other through the EPC. By using the unitary transformation introduced to diagonalize the Hamiltonian, it is straightforward to extract the Green's functions relative to the operators $\gamma_{\boldsymbol{k},\pm,\sigma}$ representing the quasiparticles in the absence of the EPC. In Fig. 7.1 we plot, for different values of the charge-lattice coupling, the density of states: $DOS_{(\mp,\mp)}(\omega) = \frac{1}{N_c}\sum_{\boldsymbol{k}} A_{\sigma,(\mp,\mp)}(\boldsymbol{k},\omega)$, where the two spectral weight functions $A_{\sigma,(\mp,\mp)}(\boldsymbol{k},\omega)$ are given by: $A_{\sigma,(\mp,\mp)}(\boldsymbol{k},\omega) = -\frac{\mathrm{Im}\{G_{\sigma,(\mp,\mp)}(\boldsymbol{k},z)\}}{\pi}$. At $\lambda = 0$, where $A_{\sigma,(\mp,\mp)}$ are delta functions peaked at $E_{k,-}$ and $E_{k,+}$, the two density of states exhibit Van Hove singularities and a finite gap due to the presence of spin-orbit coupling t_{so}. In this case the two bands are completely separated, i.e. $A_{\sigma,(-,-)}$ ($A_{\sigma,(+,+)}$) is different from zero only at ω lower (greater) than μ. By increasing EPC the two bare bands of the KM model hybridize and the gap reduces.

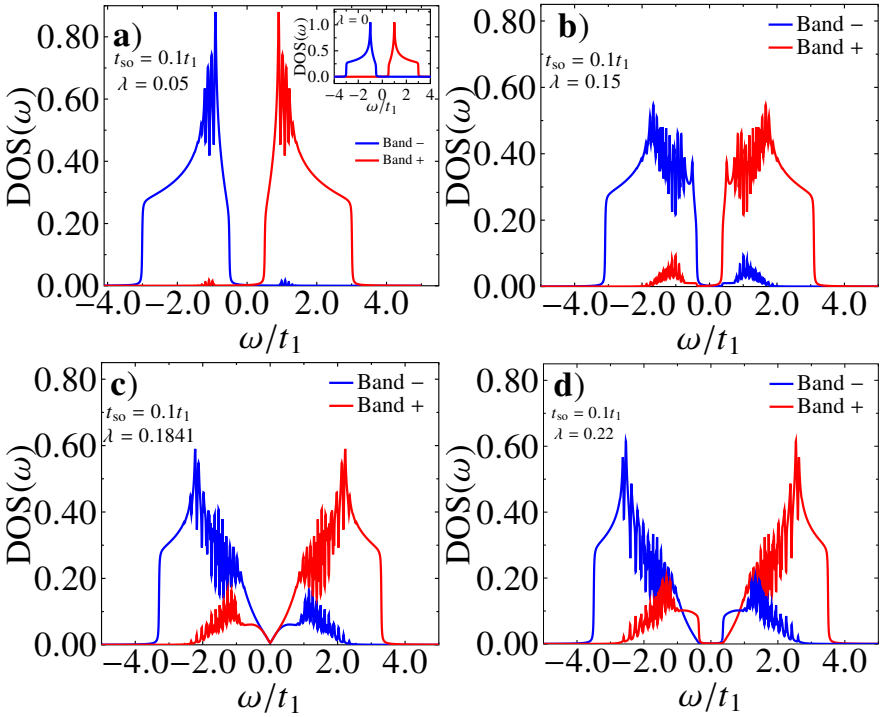

Figure 7.1: Density of states for different values of EPC.

In particular the spectra point out that, near the Van Hove singularity, there is a stronger effective charge-lattice coupling. At $\lambda_c = 0.1841$, the gap closes and, then, by further increasing EPC, reopens and becomes larger and larger. Figures 7.2a and 7.2b show that, at the K point, the spectral weight functions exhibit a finite gap for any value of λ, i.e. the Dirac points of the Graphene, K and K′, are not responsible of the behavior observed in the *DOS*. On the other hand, the plots in Fig. 7.2c, Fig. 7.2d and Fig. 7.3a point out that, by increasing the strength of EPC, the gap at M point reduces, closes exactly at λ_c (here both the functions display a peak at μ) and reopens for $\lambda > \lambda_c$. In particular, at λ_c, we followed, within the hole sector and near M point, the dispersion of the lowest energy quasiparticle peak. Fig. 7.3b shows that, at the M point, a semimetal Dirac cone appears just at λ_c. It is also worth mentioning the behavior of the average number of electrons, $n_{(-,-)}$ and $n_{(+,+)}$, associated to the lower and upper bands of the bare KM model at the M and K points. They are obtained integrating the corresponding spectral weight function up to the chemical potential. Fig. 7.3c and Fig. 7.3d show that: i) $n_{(-,-)}(\mathrm{M})$ and $n_{(+,+)}(\mathrm{M})$ present a sharp discontinuity at λ_c pointing out that they can be used as direct indicators of the quantum phase transition; ii) $n_{(-,-)}(\mathrm{K})$ and $n_{(+,+)}(\mathrm{K})$ exhibit a change of the sign of the second derivative at the value of λ where the gap at M point becomes less than the one at K point (see also Fig. 7.3a). Furthermore the value, near 0.5, reached by all the average fermion numbers for $\lambda > \lambda_c$, points out the strong

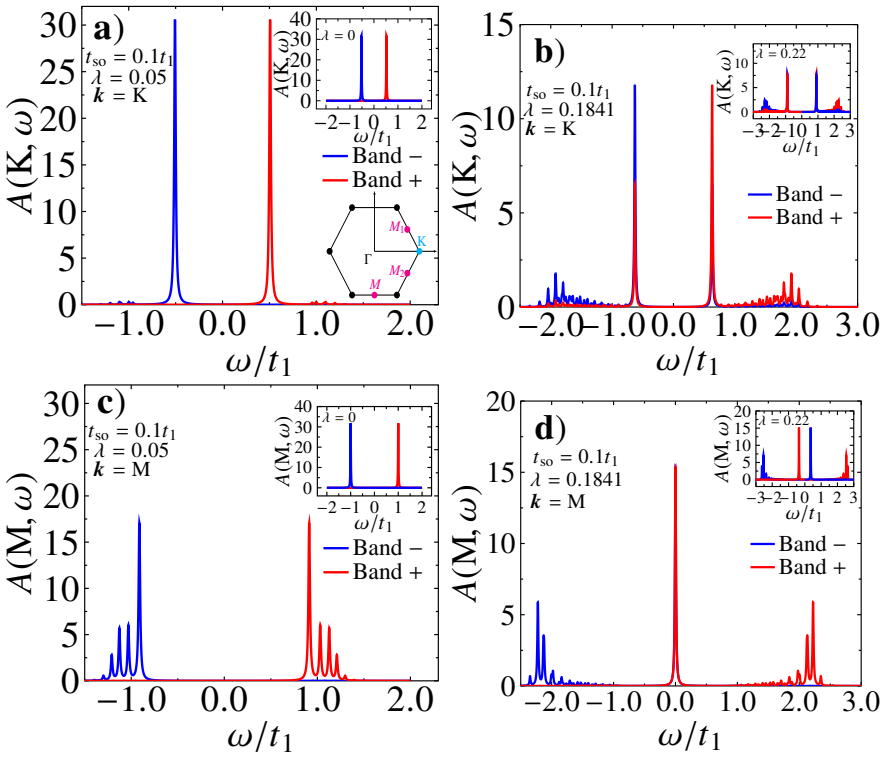

Figure 7.2: Spectral weight function at: K ((a) and (b)) and M ((c) and (d)) for different values of λ across the quantum phase transition. In the panel (a) the Brillouin zone with the time reversal invariant momenta (Γ, M, M_1,M_2) and K point indicated.

hybridization, induced by EPC, between the two bare bands of the bare KM model.

In order to shed light on the nature of the observed phase transition, we calculated the $\mathbb{Z}_2$ topological index, that, in two dimensions and in the presence of time-reversal invariance, characterizes topological band insulators. The $\mathbb{Z}_2$ invariant, ν, in the presence of inversion symmetry, can be computed via the parity eigenvalues of the interacting Green's function, obtained within the CPT, at zero energy and the time-reversal invariant momenta Γ_i. Here: i) Γ_i satisfies the relation: $-\Gamma_i = \Gamma_i + \boldsymbol{b}$, where $\boldsymbol{b}$ is a reciprocal-lattice translation vector; ii) the parity operator, i.e. the operator that interchanges the two sublattices and squares to the identity, is represented, in the sublattice basis, by the first Pauli-matrix, $P = \sigma_x$. Indeed, simultaneously diagonalizing the two matrices P and $G_\sigma(\Gamma_i, 0)$, and considering, for each of the four momenta Γ_i, the eigenvalue of P, δ_i, for the common eigenvector with a positive eigenvalue of $\boldsymbol{G}_\sigma(\Gamma_i, 0)$, it can be shown [204, 205] that: $(-1)^\nu = \prod_{i=1}^{4} \delta_i$. A topological non-trivial phase ($\nu = 1$) is associated with the occurrence of a TR-symmetry-protected pair of gapless edge modes on each edge, which takes quantized conductance. The inset in Fig. 7.3b points out that ν changes from one to zero just where the gap closes,

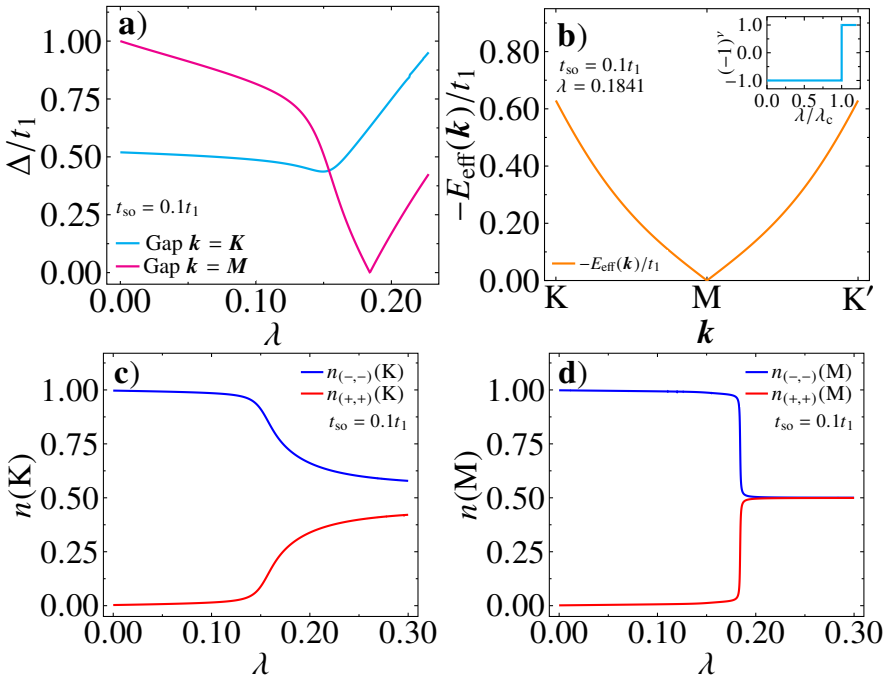

Figure 7.3: (a): the gap at K and M as function of λ; (b): the quasiparticle dispersion, within the hole sector, along the K-M-K′, at λ_c; n(K) and n(M) ((c) and (d)) as function of EPC.

i.e. at λ_c. It confirms that at λ_c a quantum phase transition, from topological to trivial insulator, occurs.

Now we investigate the effects of the quantum transition on the lattice. To this aim, we emphasize that the exact integration of the phonon degrees of freedom, through path integral technique, leads to a retarded electron-electron interaction on the same sublattice (V^0). On the other hand, the effective interaction between two charge carriers obeys the Dyson equation [220, 221]:

$$V^{eff}_{i,j}(\boldsymbol{q},z) = V^0_{i,j}(\boldsymbol{q},z) + V^0_{i,h}(\boldsymbol{q},z)\Pi^*_{h,k}(\boldsymbol{q},z\ )V^{eff}_{k,j}(\boldsymbol{q},z),$$

which defines the proper polarization insertion $\Pi^*_{i,j}(\boldsymbol{q},z)$. Here i represents a pair of indexes: the first one indicates the sublattice and the other one the spin. At the lowest order $\Pi^*_{i,j}(\boldsymbol{q},z)$ is the particle-hole bubble. The next step is to replace, in this lowest order diagram, the unperturbed electron Green's functions with the interacting Green's functions calculated within the CPT. This procedeure allows to obtain the effective interaction between two electrons and, then, the renormalized phonon propagator $D_{i,j}$.

We focus our attention on the spectral weight function $B_{(i,i)}(\boldsymbol{q}\rightarrow 0,\omega) = -\frac{\mathrm{Im}\{D_{(i,i)}\}(\boldsymbol{q},z)}{\pi}$ ($i = (A,\uparrow)$), an odd function, that, in the absence of EPC, is peaked at $\omega = \omega_0$. In Fig. 7.4 we show that, by increasing λ, the spectral weight function displays a two-peak structure. Furthermore: i) the lowest energy peak softens with EPC; ii) the

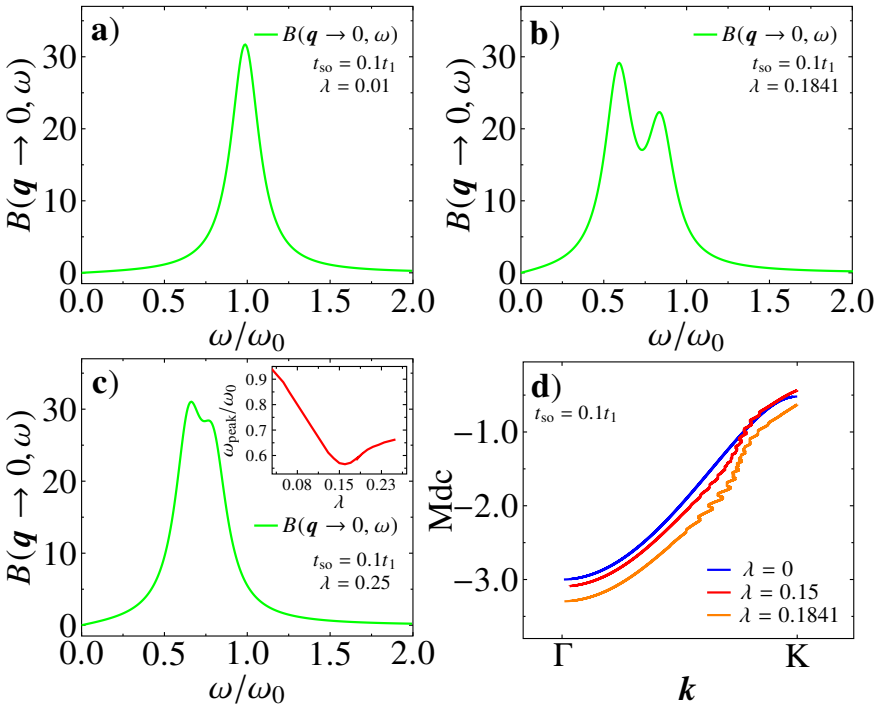

Figure 7.4: Phonon spetral weight function at different values of λ ((a), (b), and (c)). In the inset the behavior of the lowest energy peak as function of λ; (d): hole dispersion from momentum distribution curves along $\Gamma - K$ direction.

maximum softening occurs across the quantum phase transition (see inset of Fig. 7.4c). It is well known that the doubling of the phonon peak occurs when the phonon frequency is close to electronic excitation which is strongly coupled to phonon [223]. Hence, the retarded nature of the interaction induced by EPC with its own (phonon) frequency gives us a chance, which is absent in case of instantaneous Coulomb interaction, to pin down the characteristic energy scale stabilizing the topological phase, close to phonon energy within our set of parameters. Finally, in Fig. 7.4d we plot the hole peak dispersion, derived from the momentum distribution curves, along the K-Γ direction of the Brillouin zone, at different values of λ. It is evident the presence of many kinks, at $\lambda \neq 0$, caused by the coupling between the charges and the lattice vibrations.

7.3 CONCLUSIONS

We have highlighted the effects, induced by a local electron-phonon interaction, on the QSH topological insulator described by the half-filled KM model on an honeycomb lattice. By increasing EPC, a quantum phase transition, from topological to trivial insulator, is observed through a gap closing and reopening in the M point of the Brillouin

zone. Here, when the gap is closed, a semimetal Dirac cone appears and a strong hybridization between the two bare quasiparticle bands of the KM model occurs. The abrupt change in the average number of fermions at the M point, the two peak structure and the softening of the phonon Green's function, and the presence of several kinks in the renormalized quasiparticle dispersion are other distinctive features of this topological quantum phase transition.

CONCLUSIONS AND PERSPECTIVES

In this thesis work, we carried out a theoretical study of different instances of quantum systems in the presence of their environment, focusing on physical regimes where consolidated weak-coupling approaches cannot be employed. Our analysis has focused on models of macroscopic quantum systems and topological insulators. Here the physical environment is very different from one model to another. As stressed in chapter 1, in the case of a macroscopic quantum system the environment is described according to a phenomenological model, which takes into account the quantum noise arising from the coupling of the system to its sorrounding. On the other hand, in solids the presence of lattice vibrations at low temperatures is responsible for the emergence of strongly correlated phases, e. g. CDW instabilities, dramatically changing the equlibrium phase diagram of these electronic systems.

In both cases, however, in the strong coupling setting, a description based on single-particle (qubit) model cannot be succesful, as the entanglement between the interacting systems cannot be neglected, leading to interesting physical effects.

Adopting a numerically exact approach in a truncated Hilbert space, in chapters 2 and 3 we have investigated the effects of strong system-bath coupling on the dynamics of a single qubit, taking into account the non-Markovian contributions on the dynamics arising from the interaction. In the absence of driving fields, our approach has proven to succesfully describe the physics of system-bath correlations in a fairly wide range of coupling strengths.

Our analysis has then moved to different finite-time driving protocols, which are of interest in the fields of AQC and quantum simulation. Here we described in detail the dynamics of the relevant observables of the system, focusing on the environmental effects on the fidelity at final time. For intermediate up to strong dissipation, we found limited ranges of the driving parameters where the environmental influence can act to improve the fidelity of the protocols at final time. These results mainly arise from the nontrivial competition of nonadiabatic effects and decoherence in the dynamics of the reduced density operator. However, the magnitude of these effects is found to crucially depend on the form of the coupling with the environmental degrees of freedom and on the detailed protocol chosen, so that it appears difficult to draw general conclusions, and the problem thus deserves further analysis. On the other hand, for increasing coupling strengths, we found that the fidelity of the protocol quickly decreases

as strong decoherence effects set in, and our results agree with the accepted scenario.

Adopting a similar approach, in chapter 4 we studied a model of a periodically driven TLS in contact with a thermal bath, a simple model of isothermal machine operating as work-to-work converter. We simulated the nonequilibrium dynamics of the converter, and analyzed its performance in terms of efficiency, output powers and fluctuations, for different values of the driving frequency and dissipation strength. Restricting only for the sake of simplicity to the linear response regime, a wide range of driving frequencies was shown to exist such that the converter performance can violate TUR. We stress that TUR was developed in the stochastic thermodynamics setting as a tradeoff relation between entropy production and relative fluctuations of the power output in steady-state heat engines. As previous violations have been reported in the literature, a clear explanation of this result is still lacking. Coherence and non-Markovian effects in the dynamics, correctly described in our approach, could be the main causes of the described violation. It is also worth mentioning that the converter operates in a TR symmetry broken configuration, for which it has been proven that Carnot efficiency and finite power can be achieved. In the near future, our work will be devoted to a systematic understanding of these effects. As a feasible extension of our analysis, we plan to consider cyclic heat engines contacted with two thermal reservoirs and periodically driven by external fields, in order to go beyond the widely employed Markovian approach and fully understand the influence of strong system-bath correlations on the engine performance. The study could be further extended to recently proposed counter-diabatic protocols, in order to analyze their consequence on energy exchange at the microscopic scale.

In chapters 6 and 7 we have proposed a study of systems of fermions on lattices, known as prototypical examples of topological insulators. We considered the effects of microscopic EPH correlations on these systems, describing the optical phonons on the lattice by means of the Holstein model. Actually these systems belong to the class of correlated topological insulators and they have received much less attention with respect to e-e interacting case. By employing CPT methods, we studied the effects of strong EPH correlations in the Haldane model of a Chern insulator. We showed that a critical coupling strength exists for which a topological phase transition driven by EPH occurs, in which the Chern number quickly drops from 1 to 0 as a function of the EPH interaction strength. In the absence of mass term, the analysis of the phonon propagator has shown a typical signature of CDW order, i. e. the ground state of the system becomes strongly-correlated and no quantum phase trasition occurs.

A quite similar analysis has been performed in the case of KM model. In the absence of Rashba-type term, the electronic spin along

the $\hat{z}$ direction is conserved. Starting from the topological phase, which is estabilished with the gap opening due to spin-orbit interaction, increasing the interaction strength causes the gap to close in the M point of the honeycomb lattice BZ. This in turn causes the $\mathbb{Z}_2$ invariant to change sign, and thus the system turns into a trivial insulator. Our findings show that the EPH correlations act as detrimental effects to the stability of the topological phase, i. e. a gap closure and reopening occurs. This effects may be of interest, as they confirm that EPH correlations can induce bulk modifications capable of altering the topological phase, both in the absence and in the presence of TR. As it was not previously unknown that EPH can lead to band inversion, this findings can help in sheding light on the complex interplay between strong correlations and topological properties. Indeed, further extensions of this work could be linked to the search of physical systems where EPH correlations can give rise to nontrivial topological bandstructures.

Part III

APPENDIX

A SPIN-BOSON MODEL IN THE LINDBLAD APPROXIMATION

Below, we briefly report the solution of the Lindblad equation in Eq. (1.29) for the SBM Hamiltonian, discussed in Chpt.2. Following Eq. (1.29), we have to write down the eigenoperators of H_S, which can be written in terms of the Lindblad operators A_k as

$$A_k(\omega) = \sum_{E_i - E_j = \omega} \mathcal{P}(E_i) A_k \mathcal{P}(E_j) \tag{a.1}$$

where $\mathcal{P}$ are the projector over the subspace spanned by the eigenvectors of H_S, and E_i indicate the corresponding eigenvalues. The general form of the system-bath interaction is

$$H_{SB} = \sum_k A_k \otimes B_k = \sigma_z \otimes \sum_k g_k (a_k^\dagger + a_k) \tag{a.2}$$

We also indicate with E_1, E_2 and $\{|\psi_1\rangle, |\psi_2\rangle\}$ the eigenvalues and the eigenvectors of the TLS Hamiltonian in Eq. (1.7) respectively. Then the form of the eigenoperators Eq. a.1 is straightforward, and reads

$$A_k(\omega) = \sum_{E_i - E_j = \omega} |\psi_i\rangle \langle\psi_i| \sigma_z |\psi_j\rangle \langle\psi_j| \tag{a.3}$$

Notice that the Lindblad operators are independent on k, so that we can restrict the sum over the bath modes only to the decay rates. It follows that we can rewrite the dissipator and the Lamb shift as

$$\mathcal{D}(\rho_S(t)) = \sum_\omega \gamma(\omega) \left(A(\omega) \rho_S A^\dagger(\omega) - \frac{1}{2} \left\{ A^\dagger(\omega) A(\omega), \rho_S \right\} \right) \tag{a.4}$$

$$H_{LS} = \sum_\omega S(\omega)(\omega) A^\dagger(\omega) A(\omega) \tag{a.5}$$

with $\gamma(\omega)(S(\omega)) = \sum_{k,k'} \gamma_{k,k'}(\omega)(S_{k,k'}(\omega))$.

The decay rate can be found by easy manipulations. First of all, we recast it as follows

$$\begin{aligned} \gamma_{k,k'}(\omega) &= \int_{-\infty}^{+\infty} \exp(i\omega\tau) \langle B_k(\tau) B_{k'}(0) \rangle = \\ &= \int_{-\infty}^{+\infty} d\tau \exp(i\omega\tau) g_k^\star g_{k'} \left\langle (a_k^\dagger + a_k)(\tau)(a_{k'}^\dagger + a_{k'}) \right\rangle \end{aligned} \tag{a.6}$$

where the mean expectation values are to be taken over the equilibrium state of the bath, so that it holds

$$\gamma_{k,k'} = \delta_{k,k'} |g_k|^2 \int_{-\infty}^{+\infty} d\tau \exp(i\omega\tau) \left(\exp(i\omega_k \tau) \overline{n}_k + \exp(-i\omega_k \tau)(1 + \overline{n}_k) \right) \tag{a.7}$$

where $n_k = 1/(\exp(\beta\omega_k) - 1)$ are bosonic equilibrium populations of each mode. In the continuum limit, we can write the decay rate needed in Eq. (a.4) in terms of the bath spectral distribution $J(\omega) = \sum_k g_k^2 \delta(\omega - \omega_k)$ as follows

$$\begin{aligned}\gamma(\omega) = \sum_k \gamma_{k,k}(\omega) = \int_{-\infty}^{+\infty} d\tau \exp(i\omega\tau) \cdot \\ \int_0^{\infty} d\omega' J(\omega')(\exp(i\omega'\tau) n(\omega') + \exp(-i\omega'\tau)(1 + n(\omega'))) = \\ = \int_{-\infty}^{+\infty} d\tau \int_0^{\infty} d\omega' J(\omega')(\cos\omega'\tau \coth\left(\frac{\beta\omega'}{2}\right) - i\sin\omega'\tau) \quad \text{(a.8)}\end{aligned}$$

As a consequence, the closed form of $S(\omega)$ follows from reads

$$S(\omega) = 2\pi J(\omega)(\overline{n}(\omega)\Theta(-\omega) + (1 + \overline{n}(\omega))\Theta(\omega)) \quad \text{(a.9)}$$

It is thus easy to find the differential equation for the reduced density matrix $\rho_S(t)$. Indicating with $E_g = E_2 - E_1$ the gap of the TLS, only three eigenoperators are different from zero, namely

$$\begin{aligned} A(E_g) &= |\psi_2\rangle \langle\psi_2| \sigma_z |\psi_1\rangle \langle\psi_1| \\ A(-E_g) &= |\psi_1\rangle \langle\psi_1| \sigma_z |\psi_2\rangle \langle\psi_2| \\ A(0) &= \langle\psi_1| \sigma_z |\psi_1\rangle |\psi_1\rangle \langle\psi_1| + \langle\psi_2| \sigma_z |\psi_2\rangle |\psi_2\rangle \langle\psi_2| \end{aligned} \quad \text{(a.10)}$$

In the following, we restrict to the unbiased case, as it is the case of interest in Sec. 2.2 thus the qubit Hamiltonian reads $H_S = -\Gamma\sigma_x$. We choose the eigenstates $|\hat{x};\pm\rangle$ of H_S as a set of basis states, and fix the values of the reduced density matrix $[\rho_S(0)]_{ij}$, $i,j = \pm$ at initial time $t = 0$. In this basis, the only two eigenoperators different from zero are $A(E_g), A(-E_g)$, and the gap is $E_g = 2\Gamma$, so that the Lindblad solution for the considered expectation values reads [20]

$$\begin{aligned} \rho_{-+}(t) &= \rho_{-+}(0)\, e^{-i[S(2\Gamma) - S(-2\Gamma) + 2\Gamma]t} e^{-t/T_2}; \\ \rho_{--}(t) &= \rho_G(-) + [\rho_{--}(0) - \rho_G(-)]\, e^{-t/T_1}, \end{aligned} \quad \text{(a.11)}$$

where $\rho_G(\pm) = e^{\pm\beta\Gamma}/Z$ are the Gibbs distributions associated with the eigenstates $|\hat{x};\pm\rangle$, respectively, $Z = e^{\beta\Gamma} + e^{-\beta\Gamma}$ is the partition function, $S(\omega)$ is defined in Eq. (1.32) and the times $T_{1,2}$ are equal to

$$T_1 = \frac{1}{\gamma(2\Gamma)(1 + e^{-2\beta\Gamma})}, \qquad T_2 = 2T_1. \quad \text{(a.12)}$$

Starting from Eq. (a.11), the time evolution for the expectation values of $\langle\sigma_x(t)\rangle$ and $\langle\sigma_z(t)\rangle$ can be derived:

$$\begin{aligned} \langle\sigma_z(t)\rangle_L &= \rho_{-+}(0)\, e^{-i[S(2\Gamma) - S(-2\Gamma) + 2\Gamma]t} e^{-t/T_2} + \text{c.c.}; \\ \langle\sigma_x(t)\rangle_L &= \tanh(\beta\Gamma) - 2[\rho_{--}(0) - \rho_G(-)]\, e^{-t/T_1}. \end{aligned} \quad \text{(a.13)}$$

As evident from Eq. (a.13), the asymptotic value of $\langle\sigma_x(t)\rangle_L$ does not depend on the coupling strength η, but the latter affects only the equilibration time T_1.

b DETAILS ON THE QUBIT DYNAMICS

The qubit dynamics ruled by Eq. (3.5) can be easily solved in the counter-rotating reference frame around the $\hat{y}$ axis, if the static field h_o is taken to be equal to zero. Given the rotation operator of angle ϕ around the $\hat{n}$ direction $U(\hat{n}, \phi) = \exp(-\mathrm{i}\,\hat{\boldsymbol{n}} \cdot \sigma\phi/2)$, we can write the Schrödinger equation for the rotated ket $|\psi(t)\rangle_r = U\,|\psi(t)\rangle$; taking $\hbar = 1$, the Hamiltonian H_r in the rotating frame reads

$$H_r = \mathrm{i}\,\frac{\mathrm{d}U}{\mathrm{d}t}U^\dagger + UHU^\dagger \tag{b.1}$$

Notice that the Hamiltonian can be written as a sum of two terms, the first is the adiabatic gauge potential in the rotating frame, while the second is the diagonalized Hamiltonian operator. The adiabatic gauge term is responsible for the transitions between diabatic states in the rotating frame: this implies that, as shown in [143, 224], at least in principle it is possible to engineer counter-adiabatic Hamiltonians for which these transitions are always suppressed in the rotating frame. In our conventional scheme, we take $\hat{n} = \hat{y}$ and impose the counter-rotating condition $\phi(t) = -\theta(t)$, the resulting Hamiltonian H_r is time-independent and it reads:

$$H_\mathrm{r} = -\frac{h}{2}\sigma_z - \frac{\dot{\theta}}{2}\sigma_y \tag{b.2}$$

The adiabatic eigenvalues of Hamiltonian in Eq. (b.2) are $E_\pm = \pm\frac{1}{2}\sqrt{\dot{\theta}^2 + h^2}$; after computing the adiabatic eigenvectors of Eq. (b.2), given the initial state of the qubit $|\psi(t_o)\rangle$, the state of the qubit at final time t can be easily found:

$$|\psi(t)\rangle = U^\dagger(\hat{y}, \theta(t))U_r(t, t_o)U(\hat{y}, \theta(t_0))\,|\psi(t_0)\rangle \tag{b.3}$$

where $U_\mathrm{r}(t, t_o)$ is the evolution operator in the rotating frame. In the protocol described in 3.3 the qubit is initially prepared in the state $|\psi(t_o)\rangle = |\hat{z}; +\rangle$: by choosing $t_0 = 0$, the magnetic field evolves from $\theta(0) = 0$ to $\theta(t_\mathrm{f}) = \pi$, thus the final state reads

$$|\psi(t_\mathrm{f})\rangle = -\mathrm{i}\,\sigma_y \exp(-\mathrm{i}\,H_\mathrm{r} t_\mathrm{f})\,|+\rangle \tag{b.4}$$

From Eq. (b.4), the magnetization along $\hat{z}$ at the end of the protocol can be straightforwardly derived, and it reads:

$$\langle\sigma_z(t_\mathrm{f})\rangle = -\frac{h^2 + \dot{\theta}^2\cos\left(\pi\sqrt{\dot{\theta}^2 + h^2}/\dot{\theta}\right)}{\dot{\theta}^2 + h^2} \tag{b.5}$$

The excess energy at the end of the annealing can thus be directly evaluated and gives Eq. (3.8).

BIBLIOGRAPHY

[1] Arute F. et al. "Quantum supremacy using a programmable superconducting processor." English. In: *Nature* 574 (2019). ISSN: 1476-4687. DOI: 10.1038/s41586-019-1666-5. URL: https://doi.org/10.1038/s41586-019-1666-5.

[2] R. P. Feynman. In: *Int. J. Theor. Phys* 21 (1982), pp. 467–488.

[3] I. M. Georgescu, S. Ashhab, and Franco Nori. "Quantum simulation." In: *Rev. Mod. Phys.* 86 (1 2014), pp. 153–185. DOI: 10.1103/RevModPhys.86.153. URL: https://link.aps.org/doi/10.1103/RevModPhys.86.153.

[4] Maciej Lewenstein, Anna Sanpera, Veronica Ahufinger, Bogdan Damski, Aditi Sen(De), and Ujjwal Sen. "Ultracold atomic gases in optical lattices: mimicking condensed matter physics and beyond." In: *Advances in Physics* 56.2 (2007), pp. 243–379. DOI: 10.1080/00018730701223200. eprint: https://doi.org/10.1080/00018730701223200. URL: https://doi.org/10.1080/00018730701223200.

[5] J. Zhang, G. Pagano, P. W. Hess, A. Kyprianidis, P. Becker, H. Kaplan, A. V. Gorshkov, Z.-X. Gong, and C. Monroe. "Observation of a many-body dynamical phase transition with a 53-qubit quantum simulator." In: *Nature Physics* 551 (2017), pp. 601–604. DOI: 10.1038/nature24654. URL: https://doi.org/10.1038/nature24654.

[6] J. Smith, A. Lee, P. Richerme, B. Neyenhuis, P. W. Hess, P. Hauke, M. Heyl, D. A. Huse, and C. Monroe. "Many-body localization in a quantum simulator with programmable random disorder." In: *Nature Physics* 12 (2016), pp. 907–911. DOI: 10.1038/nphys3783i. URL: https://doi.org/10.1038/nphys3783.

[7] N. Goldman, J. C. Budich, and P. Zoller. "Topological quantum matter with ultracold gases in optical lattices." In: *Nature Physics* 12 (2016), pp. 639–645. DOI: 10.1038/nphys3803. URL: https://doi.org/10.1038/nphys3803.

[8] Andrew D. et al. King. "Observation of topological phenomena in a programmable lattice of 1,800 qubits." In: *Nature Physics* 560 (2018), pp. 456–460. DOI: 10.1038/s41586-018-0410-x. URL: https://doi.org/10.1038/s41586-018-0410-x.

[9] Sankar Das Sarma, Michael Freedman, and Chetan Nayak. "Majorana zero modes and topological quantum computation." In: *npj Quantum Information* 1 (1 2015). DOI: 10.1038/npjqi.2015.1. URL: https://doi.org/10.1038/npjqi.2015.1.

[10] Simon J Devitt, William J Munro, and Kae Nemoto. "Quantum error correction for beginners." In: *Reports on Progress in Physics* 76.7 (2013), p. 076001. DOI: 10.1088/0034-4885/76/7/076001. URL: https://doi.org/10.1088%2F0034-4885%2F76%2F7%2F076001.

[11] E. Paladino, Y. M. Galperin, G. Falci, and B. L. Altshuler. "1/f noise: Implications for solid-state quantum information." In: *Rev. Mod. Phys.* 86 (2 2014), pp. 361–418. DOI: 10.1103/RevModPhys.86.361. URL: https://link.aps.org/doi/10.1103/RevModPhys.86.361.

[12] A. O. Caldeira and A. J. Leggett. "Quantum tunnelling in a dissipative system." In: *Annals of Physics* 149.2 (1983), p. 374. ISSN: 0003-4916. URL: http://www.sciencedirect.com/science/article/pii/0003491683902026.

[13] W. G. Unruh. "Maintaining coherence in quantum computers." In: *Phys. Rev. A* 51 (2 1995), pp. 992–997. DOI: 10.1103/PhysRevA.51.992. URL: https://link.aps.org/doi/10.1103/PhysRevA.51.992.

[14] F. M. Cucchietti, J. P. Paz, and W. H. Zurek. "Decoherence from spin environments." In: *Phys. Rev. A* 72 (5 2005), p. 052113. DOI: 10.1103/PhysRevA.72.052113. URL: https://link.aps.org/doi/10.1103/PhysRevA.72.052113.

[15] Wojciech Hubert Zurek. "Decoherence, einselection, and the quantum origins of the classical." In: *Rev. Mod. Phys.* 75 (3 2003), pp. 715–775. DOI: 10.1103/RevModPhys.75.715. URL: https://link.aps.org/doi/10.1103/RevModPhys.75.715.

[16] Wojciech Hubert Zurek. "Quantum Darwinism." In: *Nature Physics* 5 (3 2009), pp. 181–188. DOI: 10.1038/nphys1202. URL: https://doi.org/10.1038/nphys1202.

[17] Tameem Albash and Daniel A. Lidar. "Adiabatic quantum computation." In: *Rev. Mod. Phys.* 90 (1 2018), p. 015002. DOI: 10.1103/RevModPhys.90.015002. URL: https://link.aps.org/doi/10.1103/RevModPhys.90.015002.

[18] R. Harris et al. "Quantum annealing with manufactured spins." In: *Nature* 473 (7346 2011), pp. 194–198. URL: http://dx.doi.org/10.1038/nature10012.

[19] A. M. Childs, E. Farhi, and J. Preskill. "Robustness of adiabatic quantum computation." In: *Phys. Rev. A* 65 (1 2001), p. 012322. URL: http://link.aps.org/doi/10.1103/PhysRevA.65.012322.

[20] T. Albash and D. A. Lidar. "Decoherence in adiabatic quantum computation." In: *Phys. Rev. A* 91 (6 2015), p. 062320. URL: http://link.aps.org/doi/10.1103/PhysRevA.91.062320.

[21] A. Mishra, T. Albash, and D. A. Lidar. "Finite temperature quantum annealing solving exponentially small gap problem with non-monotonic success probability." English. In: *Nature Communications* 9 (2018). DOI: 10.1038/s41467-018-05239-9. URL: https://doi.org/10.1038/s41467-018-05239-9.

[22] R Alicki. "The quantum open system as a model of the heat engine." In: *Journal of Physics A: Mathematical and General* 12.5 (1979), pp. L103–L107. DOI: 10.1088/0305-4470/12/5/007. URL: https://doi.org/10.1088%2F0305-4470%2F12%2F5%2F007.

[23] D. Gelbwaser-Klimovsky, R. Alicki, and G. Kurizki. "Minimal universal quantum heat machine." In: *Phys. Rev. E* 87 (1 2013), p. 012140. DOI: 10.1103/PhysRevE.87.012140. URL: https://link.aps.org/doi/10.1103/PhysRevE.87.012140.

[24] Raam Uzdin, Amikam Levy, and Ronnie Kosloff. "Equivalence of Quantum Heat Machines, and Quantum-Thermodynamic Signatures." In: *Phys. Rev. X* 5 (3 2015), p. 031044. DOI: 10.1103/PhysRevX.5.031044. URL: https://link.aps.org/doi/10.1103/PhysRevX.5.031044.

[25] Michele Campisi, Jukka Pekola, and Rosario Fazio. "Nonequilibrium fluctuations in quantum heat engines: theory, example, and possible solid state experiments." In: *New Journal of Physics* 17.3 (2015), p. 035012. DOI: 10.1088/1367-2630/17/3/035012. URL: https://doi.org/10.1088%2F1367-2630%2F17%2F3%2F035012.

[26] Kosloff R. Alicki R. "Introduction to Quantum Thermodynamics: History and Prospects." In: *Binder F., Correa L., Gogolin C., Anders J., Adesso G. (eds) Thermodynamics in the Quantum Regime* vol 195 (2018), p. 015002. DOI: https://doi.org/10.1007/978-3-319-99046-0_1. URL: https://link.aps.org/doi/10.1103/RevModPhys.90.015002.

[27] John Goold, Marcus Huber, Arnau Riera, Lídia del Rio, and Paul Skrzypczyk. "The role of quantum information in thermodynamics—a topical review." In: *Journal of Physics A: Mathematical and Theoretical* 49.14 (2016), p. 143001. DOI: 10.1088/1751-8113/49/14/143001. URL: https://doi.org/10.1088%2F1751-8113%2F49%2F14%2F143001.

[28] U. Weiss. *Quantum dissipative systems*. World Scientific, 2012. ISBN: 978-981-4374-92-7.

[29] Jozef T Devreese and Alexandre S Alexandrov. "Fr ohlich polaron and bipolaron: recent developments." In: *Reports on Progress in Physics* 72.6 (2009), p. 066501. DOI: 10.1088/0034-4885/72/6/066501. URL: https://doi.org/10.1088%2F0034-4885%2F72%2F6%2F066501.

[30] G. Grüner. "The dynamics of charge-density waves." In: *Rev. Mod. Phys.* 60 (4 1988), pp. 1129–1181. DOI: 10.1103/RevModPhys.60.1129. URL: https://link.aps.org/doi/10.1103/RevModPhys.60.1129.

[31] B. Keimer, S. A. Kivelson, M. R. Norman, S. Uchida, and J. Zaanen. "From quantum matter to high-temperature superconductivity in copper oxides." In: *Nature Physics* 518 (2015). DOI: 10.1038/nature14165. URL: https://doi.org/10.1038/nature14165.

[32] Subir Sachdev. *The Theory of Open Quantum Systems*. Cambridge University Press, 2011. ISBN: 9780521514682.

[33] Matthias Vojta. "Quantum phase transitions." In: *Reports on Progress in Physics* 66.12 (2003), pp. 2069–2110. DOI: 10.1088/0034-4885/66/12/r01. URL: https://doi.org/10.1088%2F0034-4885%2F66%2F12%2Fr01.

[34] Xiao-Gang Wen. "Colloquium: Zoo of quantum-topological phases of matter." In: *Rev. Mod. Phys.* 89 (4 2017), p. 041004. DOI: 10.1103/RevModPhys.89.041004. URL: https://link.aps.org/doi/10.1103/RevModPhys.89.041004.

[35] Xiao-Gang Wen. *Quantum Field Theory of Many-Body Systems: From the Origin of Sound to an Origin of Light and Electrons*. Cambridge University Press, 2007. ISBN: 9780199227259. DOI: 10.1093/acprof:oso/9780199227259.001.0001.

[36] M. Z. Hasan and C. L. Kane. "Colloquium: Topological insulators." In: *Rev. Mod. Phys.* 82 (4 2010), pp. 3045–3067. DOI: 10.1103/RevModPhys.82.3045. URL: https://link.aps.org/doi/10.1103/RevModPhys.82.3045.

[37] Xiao-Liang Qi and Shou-Cheng Zhang. "Topological insulators and superconductors." In: *Rev. Mod. Phys.* 83 (4 2011), pp. 1057–1110. DOI: 10.1103/RevModPhys.83.1057. URL: https://link.aps.org/doi/10.1103/RevModPhys.83.1057.

[38] László Oroszlány János K. Asbóth and András Pályi. *A Short Course on Topological Insulators*. Springer International Publishing, 2016. ISBN: 978-3-319-25607-8.

[39] B. Andrei Bernevig. *Topological insulators and topological superconductors*. Princeton University Press, 2013. ISBN: 9780691151755.

[40] Stephan Rachel. "Interacting topological insulators: a review." In: *Reports on Progress in Physics* 81.11 (2018), p. 116501. DOI: 10.1088/1361-6633/aad6a6. URL: https://doi.org/10.1088%2F1361-6633%2Faad6a6.

[41] Stephan Rachel and Karyn Le Hur. "Topological insulators and Mott physics from the Hubbard interaction." In: *Phys. Rev. B* 82 (7 2010), p. 075106. DOI: 10.1103/PhysRevB.82.075106. URL: https://link.aps.org/doi/10.1103/PhysRevB.82.075106.

[42] S. Raghu, Xiao-Liang Qi, C. Honerkamp, and Shou-Cheng Zhang. "Topological Mott Insulators." In: *Phys. Rev. Lett.* 100 (15 2008), p. 156401. DOI: 10.1103/PhysRevLett.100.156401. URL: https://link.aps.org/doi/10.1103/PhysRevLett.100.156401.

[43] Titus Neupert, Luiz Santos, Claudio Chamon, and Christopher Mudry. "Fractional Quantum Hall States at Zero Magnetic Field." In: *Phys. Rev. Lett.* 106 (23 2011), p. 236804. DOI: 10.1103/PhysRevLett.106.236804. URL: https://link.aps.org/doi/10.1103/PhysRevLett.106.236804.

[44] L. Magazzú, P. Forn-Díaz, R. Belyansky, J.L. Orgiazzi, M. A. Yurtalan, M. R. Otto, A. Lupascu, C. M. Wilson, and M. Grifoni. "Probing the strongly driven spin-boson model in a superconducting quantum circuit." In: *Nature Communications* 9 (2018). DOI: 10.1038/s41467-018-03626-w. URL: https://doi.org/10.1038/s41467-018-03626-w.

[45] Loïc Henriet, Antonio Sclocchi, Peter P. Orth, and Karyn Le Hur. "Topology of a dissipative spin: Dynamical Chern number, bath-induced nonadiabaticity, and a quantum dynamo effect." In: *Phys. Rev. B* 95 (5 2017), p. 054307. DOI: 10.1103/PhysRevB.95.054307. URL: https://link.aps.org/doi/10.1103/PhysRevB.95.054307.

[46] Karel Proesmans, Bart Cleuren, and Christian Van den Broeck. "Power-Efficiency-Dissipation Relations in Linear Thermodynamics." In: *Phys. Rev. Lett.* 116 (22 2016), p. 220601. DOI: 10.1103/PhysRevLett.116.220601. URL: https://link.aps.org/doi/10.1103/PhysRevLett.116.220601.

[47] D. Meyer, A. C. Hewson, and R. Bulla. "Gap Formation and Soft Phonon Mode in the Holstein Model." In: *Phys. Rev. Lett.* 89 (19 2002), p. 196401. DOI: 10.1103/PhysRevLett.89.196401. URL: https://link.aps.org/doi/10.1103/PhysRevLett.89.196401.

[48] David Sénéchal, Danny Perez, and Dany Plouffe. "Cluster perturbation theory for Hubbard models." In: *Phys. Rev. B* 66 (7 2002), p. 075129. DOI: 10.1103/PhysRevB.66.075129. URL: https://link.aps.org/doi/10.1103/PhysRevB.66.075129.

[49] A. J. Leggett, S. Chakravarty, A. T. Dorsey, Matthew P. A. Fisher, Anupam Garg, and W. Zwerger. "Dynamics of the dissipative two-state system." In: *Rev. Mod. Phys.* 59 (1 1987), pp. 1–85. DOI: 10.1103/RevModPhys.59.1. URL: https://link.aps.org/doi/10.1103/RevModPhys.59.1.

[50] Matthew P. A. Fisher and Wilhelm Zwerger. "Quantum Brownian motion in a periodic potential." In: *Phys. Rev. B* 32 (10 1985), pp. 6190–6206. DOI: 10.1103/PhysRevB.32.6190. URL: https://link.aps.org/doi/10.1103/PhysRevB.32.6190.

[51] Hermann Grabert, Ulrich Weiss, and Peter Talkner. "Quantum theory of the damped harmonic oscillator." In: *Zeitschrift für Physik B Condensed Matter* 55.1 (1984), pp. 87–94. ISSN: 1431-584X. DOI: 10.1007/BF01307505. URL: https://doi.org/10.1007/BF01307505.

[52] M. Topaler and N. Makri. "Quasi-adiabatic propagator path integral methods. Exact quantum rate constants for condensed phase reactions." In: *Chemical Physics Letters* 210.1 (1993), pp. 285–293. ISSN: 0009-2614. DOI: https://doi.org/10.1016/0009-2614(93)89135-5. URL: http://www.sciencedirect.com/science/article/pii/0009261493891355.

[53] Reinhold Egger and C. H. Mak. "Low-temperature dynamical simulation of spin-boson systems." In: *Phys. Rev. B* 50 (20 1994), pp. 15210–15220. DOI: 10.1103/PhysRevB.50.15210. URL: https://link.aps.org/doi/10.1103/PhysRevB.50.15210.

[54] Ze-Liang Xiang, Sahel Ashhab, J. Q. You, and Franco Nori. "Hybrid quantum circuits: Superconducting circuits interacting with other quantum systems." In: *Rev. Mod. Phys.* 85 (2 2013), pp. 623–653. DOI: 10.1103/RevModPhys.85.623. URL: https://link.aps.org/doi/10.1103/RevModPhys.85.623.

[55] J. I. Cirac and P. Zoller. "Quantum Computations with Cold Trapped Ions." In: *Phys. Rev. Lett.* 74 (20 1995), pp. 4091–4094. DOI: 10.1103/PhysRevLett.74.4091. URL: https://link.aps.org/doi/10.1103/PhysRevLett.74.4091.

[56] D. Jaksch, C. Bruder, J. I. Cirac, C. W. Gardiner, and P. Zoller. "Cold Bosonic Atoms in Optical Lattices." In: *Phys. Rev. Lett.* 81 (15 1998), pp. 3108–3111. DOI: 10.1103/PhysRevLett.81.3108. URL: https://link.aps.org/doi/10.1103/PhysRevLett.81.3108.

[57] M A Cirone, G De Chiara, G M Palma, and A Recati. "Collective decoherence of cold atoms coupled to a Bose–Einstein condensate." In: *New Journal of Physics* 11.10 (2009), p. 103055. DOI: 10.1088/1367-2630/11/10/103055. URL: https://doi.org/10.1088%2F1367-2630%2F11%2F10%2F103055.

[58] M. Vojta, N.-H. Tong, and R. Bulla. "Quantum Phase Transitions in the Sub-Ohmic Spin-Boson Model: Failure of the Quantum-Classical Mapping." In: *Phys. Rev. Lett.* 94 (7 2005), p. 070604. DOI: 10.1103/PhysRevLett.94.070604. URL: https://link.aps.org/doi/10.1103/PhysRevLett.94.070604.

[59] Y. Nakamura, Yu. A. Pashkin, and J. S Tsai. "Coherent control of macroscopic quantum states in a single-Cooper-pair box." In: *Nature physics* 398 (6730 1999). DOI: 10.1038/19718. URL: https://doi.org/10.1038/19718.

[60] J. Clarke and Frank K. Wilhelm. "Superconducting quantum bits." In: *Nature Physics* 9 (2008). DOI: 10.1038/nature07128. URL: https://doi.org/10.1038/nature07128.

[61] E. Paladino, L. Faoro, G. Falci, and Rosario Fazio. "Decoherence and $1/f$ Noise in Josephson Qubits." In: *Phys. Rev. Lett.* 88 (22 2002), p. 228304. DOI: 10.1103/PhysRevLett.88.228304. URL: https://link.aps.org/doi/10.1103/PhysRevLett.88.228304.

[62] Alexander Shnirman, Yuriy Makhlin, Yuriy Makhlin, and Gerd Schön. "Noise and Decoherence in Quantum Two-Level Systems." In: *Physica Scripta* T102.1 (2002), p. 147. DOI: 10.1238/physica.topical.102a00147. URL: https://doi.org/10.1238%2Fphysica.topical.102a00147.

[63] G Wendin. "Quantum information processing with superconducting circuits: a review." In: *Reports on Progress in Physics* 80.10 (2017), p. 106001. DOI: 10.1088/1361-6633/aa7e1a. URL: https://doi.org/10.1088%2F1361-6633%2Faa7e1a.

[64] Jonathan J. Burnett, Andreas Bengtsson, Marco Scigliuzzo, David Niepce, Marina Kudra, Per Delsing, and Jonas Bylander. "Superconducting quantum bits." In: *npj Quantum Information* 5 (2019). DOI: 10.1038/s41534-019-0168-5. URL: https://doi.org/10.1038/s41534-019-0168-5.

[65] K. Le Hur. "Entanglement entropy, decoherence, and quantum phase transitions of a dissipative two-level system." In: *Annals of Physics* 323.9 (2008), pp. 2208 –2240. ISSN: 0003-4916. DOI: https://doi.org/10.1016/j.aop.2007.12.003. URL: http://www.sciencedirect.com/science/article/pii/S0003491607001790.

[66] Alexander Cyril Hewson. *The Kondo Problem to Heavy Fermions*. Cambridge University Press, 1993. ISBN: 9780511470752.

[67] F. Guinea, V. Hakim, and A. Muramatsu. "Bosonization of a two-level system with dissipation." In: *Phys. Rev. B* 32 (7 1985), pp. 4410–4418. DOI: 10.1103/PhysRevB.32.4410. URL: https://link.aps.org/doi/10.1103/PhysRevB.32.4410.

[68] Karyn Le Hur, Philippe Doucet-Beaupré, and Walter Hofstetter. "Entanglement and Criticality in Quantum Impurity Systems." In: *Phys. Rev. Lett.* 99 (12 2007), p. 126801. DOI: 10.1103/PhysRevLett.99.126801. URL: https://link.aps.org/doi/10.1103/PhysRevLett.99.126801.

[69] Jan von Delft and Herbert Schoeller. "Bosonization for beginners - refermionization for experts." In: *Annalen der Physik* 7.4 (1998), pp. 225–305. DOI: 10.1002/(SICI)1521-3889(199811)7:4<225::AID-ANDP225>3.0.CO;2-L. eprint: https://onlinelibrary.wiley.com/doi/pdf/10.1002/%28SICI%291521-3889%28199811%297%3A4%3C225%3A%3AAID-ANDP225%3E3.0.CO%3B2-L. URL: https://onlinelibrary.wiley.com/doi/abs/10.1002/%28SICI%291521-3889%28199811%297%3A4%3C225%3A%3AAID-ANDP225%3E3.0.CO%3B2-L.

[70] P. W. Anderson, G. Yuval, and D. R. Hamann. "Exact Results in the Kondo Problem. II. Scaling Theory, Qualitatively Correct Solution, and Some New Results on One-Dimensional Classical Statistical Models." In: *Phys. Rev. B* 1 (11 1970), pp. 4464–4473. DOI: 10.1103/PhysRevB.1.4464. URL: https://link.aps.org/doi/10.1103/PhysRevB.1.4464.

[71] J. M. Kosterlitz and D. J. Thouless. "Ordering, metastability and phase transitions in two-dimensional systems." In: *Journal of Physics C: Solid State Physics* 6.7 (1972), pp. 1181–1203.

[72] Matthias Vojta. "Impurity quantum phase transitions." In: *Philosophical Magazine* 86.13-14 (2006), pp. 1807–1846. DOI: 10.1080/14786430500070396. eprint: https://doi.org/10.1080/14786430500070396. URL: https://doi.org/10.1080/14786430500070396.

[73] G. De Filippis, A. de Candia, L. M. Cangemi, M. Sassetti, R. Fazio, and V. Cataudella. *Quantum Phase Transitions in the Spin-Boson model: MonteCarlo Method vs Variational Approach a la Feynman*. 2019. arXiv: 1912.13448 [cond-mat.stat-mech].

[74] R. Bulla, N.-H. Tong, and M. Vojta. "Numerical Renormalization Group for Bosonic Systems and Application to the Sub-Ohmic Spin-Boson Model." In: *Phys. Rev. Lett.* 91 (17 2003), p. 170601. DOI: 10.1103/PhysRevLett.91.170601. URL: https://link.aps.org/doi/10.1103/PhysRevLett.91.170601.

[75] H. P. Breuer and F. Petruccione. *The Theory of Open Quantum Systems*. OUP Oxford, 2007. ISBN: 9780199213900.

[76] Peter P. Orth, Adilet Imambekov, and Karyn Le Hur. "Nonperturbative stochastic method for driven spin-boson model." In: *Phys. Rev. B* 87 (1 2013), p. 014305. DOI: 10.1103/PhysRevB.87.014305. URL: https://link.aps.org/doi/10.1103/PhysRevB.87.014305.

[77] Robert Zwanzig. *Nonequilibrium statistical mechanics*. Oxford University Press, 2001. ISBN: 0195140184.

[78] Heinz-Peter Breuer, Elsi-Mari Laine, Jyrki Piilo, and Bassano Vacchini. "Colloquium: Non-Markovian dynamics in open quantum systems." In: *Rev. Mod. Phys.* 88 (2 2016), p. 021002.

DOI: 10.1103/RevModPhys.88.021002. URL: https://link.aps.org/doi/10.1103/RevModPhys.88.021002.

[79] T. Albash, S. Boixo, D. A. Lidar, and P. Zanardi. "Quantum adiabatic Markovian master equations." In: *New Journal of Physics* 14.12 (2012), p. 123016. URL: http://stacks.iop.org/1367-2630/14/i=12/a=123016.

[80] Vasco Cavina, Andrea Mari, and Vittorio Giovannetti. "Slow Dynamics and Thermodynamics of Open Quantum Systems." In: *Phys. Rev. Lett.* 119 (5 2017), p. 050601. DOI: 10.1103/PhysRevLett.119.050601. URL: https://link.aps.org/doi/10.1103/PhysRevLett.119.050601.

[81] Robert Alicki and K. Lendi. *Quantum Dynamical Semigroups and Applications*. Springer-Verlag Berlin Heidelberg, 2007. ISBN: 978-3-540-70860-5.

[82] Michael A. Nielsen and Isaac L. Chuang. *Quantum Computation and Quantum Information*. Cambridge University Press, 2010. ISBN: 9780511976667.

[83] G. Lindblad. "On the generators of quantum dynamical semigroups." In: *Comm. Math. Phys.* 48.2 (1976), pp. 119–130. URL: https://projecteuclid.org:443/euclid.cmp/1103899849.

[84] Vittorio Gorini, Andrzej Kossakowski, and E. C. G. Sudarshan. "Completely positive dynamical semigroups of N level systems." In: *Journal of Mathematical Physics* 17.5 (1976), pp. 821–825. DOI: 10.1063/1.522979. eprint: https://aip.scitation.org/doi/pdf/10.1063/1.522979. URL: https://aip.scitation.org/doi/abs/10.1063/1.522979.

[85] R.P Feynman and F.L Vernon. "The theory of a general quantum system interacting with a linear dissipative system." In: *Annals of Physics* 24 (1963), pp. 118 –173. ISSN: 0003-4916. DOI: https://doi.org/10.1016/0003-4916(63)90068-X. URL: http://www.sciencedirect.com/science/article/pii/000349166390068X.

[86] Francesco Nesi, Elisabetta Paladino, Michael Thorwart, and Milena Grifoni. "Spin-boson dynamics beyond conventional perturbation theories." In: *Phys. Rev. B* 76 (15 2007), p. 155323. DOI: 10.1103/PhysRevB.76.155323. URL: https://link.aps.org/doi/10.1103/PhysRevB.76.155323.

[87] Milena Grifoni and Peter Hänggi. "Driven quantum tunneling." In: *Physics Reports* 304.5 (1998), pp. 229 –354. ISSN: 0370-1573. DOI: https://doi.org/10.1016/S0370-1573(98)00022-2. URL: http://www.sciencedirect.com/science/article/pii/S0370157398000222.

[88] Milton Abramowitz. *Handbook of Mathematical Functions, With Formulas, Graphs, and Mathematical Tables*, USA: Dover Publications, Inc., 1974. ISBN: 0486612724.

[89] Reinhold Egger, Hermann Grabert, and Ulrich Weiss. "Crossover from coherent to incoherent dynamics in damped quantum systems." In: *Phys. Rev. E* 55 (4 1997), R3809–R3812. DOI: 10.1103/PhysRevE.55.R3809. URL: https://link.aps.org/doi/10.1103/PhysRevE.55.R3809.

[90] M Carrega, P Solinas, A Braggio, M Sassetti, and U Weiss. "Functional integral approach to time-dependent heat exchange in open quantum systems: general method and applications." In: *New Journal of Physics* 17.4 (2015), p. 045030. DOI: 10.1088/1367-2630/17/4/045030. URL: https://doi.org/10.1088%2F1367-2630%2F17%2F4%2F045030.

[91] Maura Sassetti and Ulrich Weiss. "Correlation functions for dissipative two-state systems: Effects of the initial preparation." In: *Phys. Rev. A* 41 (10 1990), pp. 5383–5393. DOI: 10.1103/PhysRevA.41.5383. URL: https://link.aps.org/doi/10.1103/PhysRevA.41.5383.

[92] Curt Wittig. "The Landau âĹŠ Zener Formula." In: *The Journal of Physical Chemistry B* 109.1 (2005), pp. 8428–8430. DOI: doi:10.1021/jp040627u. URL: https://doi.org/10.1021/jp040627u.

[93] Yosuke Kayanuma. "Nonadiabatic Transitions in Level Crossing with Energy Fluctuation. I. Analytical Investigations." In: *Journal of the Physical Society of Japan* 53.1 (1984), pp. 108–117. DOI: 10.1143/JPSJ.53.108. eprint: https://doi.org/10.1143/JPSJ.53.108. URL: https://doi.org/10.1143/JPSJ.53.108.

[94] Yuval Gefen, Eshel Ben-Jacob, and Amir O. Caldeira. "Zener transitions in dissipative driven systems." In: *Phys. Rev. B* 36 (5 1987), pp. 2770–2782. DOI: 10.1103/PhysRevB.36.2770. URL: https://link.aps.org/doi/10.1103/PhysRevB.36.2770.

[95] Ping Ao and Jo/rgen Rammer. "Quantum dynamics of a two-state system in a dissipative environment." In: *Phys. Rev. B* 43 (7 1991), pp. 5397–5418. DOI: 10.1103/PhysRevB.43.5397. URL: https://link.aps.org/doi/10.1103/PhysRevB.43.5397.

[96] Martijn Wubs, Keiji Saito, Sigmund Kohler, Peter Hänggi, and Yosuke Kayanuma. "Gauging a Quantum Heat Bath with Dissipative Landau-Zener Transitions." In: *Phys. Rev. Lett.* 97 (20 2006), p. 200404. DOI: 10.1103/PhysRevLett.97.200404. URL: https://link.aps.org/doi/10.1103/PhysRevLett.97.200404.

[97] M. H. S. Amin, Peter J. Love, and C. J. S. Truncik. "Thermally Assisted Adiabatic Quantum Computation." In: *Phys. Rev. Lett.* 100 (6 2008), p. 060503. DOI: 10.1103/PhysRevLett.100.060503. URL: https://link.aps.org/doi/10.1103/PhysRevLett.100.060503.

[98] N. G. Dickson et al. "Thermally assisted quantum annealing of a 16-qubit problem." English. In: *Nature Communications* 4 (2013). ISSN: 2041-1723. DOI: 10.1038/ncomms2920. URL: https://www.nature.com/articles/ncomms2920.

[99] G. Passarelli, G. De Filippis, V. Cataudella, and P. Lucignano. "Dissipative environment may improve the quantum annealing performances of the ferromagnetic *p*-spin model." In: *Phys. Rev. A* 97 (2 2018), p. 022319. DOI: 10.1103/PhysRevA.97.022319. URL: https://link.aps.org/doi/10.1103/PhysRevA.97.022319.

[100] Luca Arceci, Simone Barbarino, Rosario Fazio, and Giuseppe E. Santoro. "Dissipative Landau-Zener problem and thermally assisted Quantum Annealing." In: *Phys. Rev. B* 96 (5 2017), p. 054301. DOI: 10.1103/PhysRevB.96.054301. URL: https://link.aps.org/doi/10.1103/PhysRevB.96.054301.

[101] Eric Boyers, Mohit Pandey, David K. Campbell, Anatoli Polkovnikov, Dries Sels, and Alexander O. Sushkov. "Floquet-engineered quantum state manipulation in a noisy qubit." In: *Phys. Rev. A* 100 (1 2019), p. 012341. DOI: 10.1103/PhysRevA.100.012341. URL: https://link.aps.org/doi/10.1103/PhysRevA.100.012341.

[102] Pieter W. Claeys, Mohit Pandey, Dries Sels, and Anatoli Polkovnikov. "Floquet-Engineering Counterdiabatic Protocols in Quantum Many-Body Systems." In: *Phys. Rev. Lett.* 123 (9 2019), p. 090602. DOI: 10.1103/PhysRevLett.123.090602. URL: https://link.aps.org/doi/10.1103/PhysRevLett.123.090602.

[103] F. Grossmann, T. Dittrich, P. Jung, and P. Hänggi. "Coherent destruction of tunneling." In: *Phys. Rev. Lett.* 67 (4 1991), pp. 516–519. DOI: 10.1103/PhysRevLett.67.516. URL: https://link.aps.org/doi/10.1103/PhysRevLett.67.516.

[104] Robert Alicki, Daniel A. Lidar, and Paolo Zanardi. "Internal consistency of fault-tolerant quantum error correction in light of rigorous derivations of the quantum Markovian limit." In: *Phys. Rev. A* 73 (5 2006), p. 052311. DOI: 10.1103/PhysRevA.73.052311. URL: https://link.aps.org/doi/10.1103/PhysRevA.73.052311.

[105] Noam Erez, Goren Gordon, Mathias Nest, and Gershon Kurizki. "Thermodynamic control by frequent quantum measurements." In: *Nature Physics* 452 (2001). DOI: 10.1038/nature06873. URL: https://doi.org/10.1038/nature06873.

[106] Nancy Makri and Dmitrii E. Makarov. "Tensor propagator for iterative quantum time evolution of reduced density matrices. II. Numerical methodology." In: *The Journal of Chemical Physics* 102.11 (1995), pp. 4611–4618. DOI: 10.1063/1.469509. eprint: https://doi.org/10.1063/1.469509. URL: https://doi.org/10.1063/1.469509.

[107] A. Strathearn, P. Kirton, D. Kilda, J. Keeling, and B. W. Lovett. "Efficient non-Markovian quantum dynamics using time-evolving matrix product operators." In: *Nature Communications* 9 (Aug. 2018). DOI: 10.1038/s41467-018-05617-3. URL: https://doi.org/10.1038/s41467-018-05617-3.

[108] L. M. Cangemi, G. Passarelli, V. Cataudella, P. Lucignano, and G. De Filippis. "Beyond the Born-Markov approximation: Dissipative dynamics of a single qubit." In: *Phys. Rev. B* 98 (18 2018), p. 184306. DOI: 10.1103/PhysRevB.98.184306. URL: https://link.aps.org/doi/10.1103/PhysRevB.98.184306.

[109] V. N. Smelyanskiy, D. Venturelli, A. Perdomo-Ortiz, S. Knysh, and M.I. Dykman. In: *Phys. Rev. Lett.* 118 (2017), p. 066802.

[110] K. Kechedzhi and V. N. Smelyanskiy. In: *Phys. Rev. X* 6 (2016), p. 021028.

[111] T. Kadowaki and H. Nishimori. "Quantum annealing in the transverse Ising model." In: *Phys. Rev. E* 58 (5 1998), pp. 5355–5363. URL: http://link.aps.org/doi/10.1103/PhysRevE.58.5355.

[112] Edward Farhi, Jeffrey Goldstone, Sam Gutmann, and Michael Sipser. *Quantum Computation by Adiabatic Evolution*. 2000. arXiv: quant-ph/0001106 [quant-ph].

[113] Simone Cialdi, Davide Brivio, Enrico Tesio, and Matteo G. A. Paris. "Programmable entanglement oscillations in a non-Markovian channel." In: *Phys. Rev. A* 83 (4 2011), p. 042308. DOI: 10.1103/PhysRevA.83.042308. URL: https://link.aps.org/doi/10.1103/PhysRevA.83.042308.

[114] Bi-Heng Liu, Li Li, Yun-Feng Huang, Chuan-Feng Li, Guang-Can Guo, Elsi-Mari Laine, Heinz-Peter Breuer, and Jyrki Piilo. "Experimental control of the transition from Markovian to non-Markovian dynamics of openÂăquantumÂăsystems." English. In: *Nature Physics* 7 (2011). DOI: 10.1038/nphys2085. URL: https://doi.org/10.1038/nphys2085.

[115] M. Thorwart, J. Eckel, and E. R. Mucciolo. "Non-Markovian dynamics of double quantum dot charge qubits due to acoustic phonons." In: *Phys. Rev. B* 72 (23 2005), p. 235320. DOI: 10.1103/PhysRevB.72.235320. URL: https://link.aps.org/doi/10.1103/PhysRevB.72.235320.

[116] I. Goychuk and P. Hänggi. "Quantum two-state dynamics driven by stationary non-Markovian discrete noise: Exact results." In: *Chemical Physics* 324.1 (2006), pp. 160–171. ISSN: 0301-0104. DOI: https://doi.org/10.1016/j.chemphys.2005.11.026. URL: http://www.sciencedirect.com/science/article/pii/S030101040500621X.

[117] Inés de Vega, Ulrich Schollwöck, and F. Alexander Wolf. "How to discretize a quantum bath for real-time evolution." In: *Phys. Rev. B* 92 (15 2015), p. 155126. DOI: 10.1103/PhysRevB.92.155126. URL: https://link.aps.org/doi/10.1103/PhysRevB.92.155126.

[118] Tae Jun Park and J. C. Light. "Unitary quantum time evolution by iterative Lanczos reduction." In: *The Journal of Chemical Physics* 85.10 (1986), pp. 5870–5876. DOI: 10.1063/1.451548. eprint: https://doi.org/10.1063/1.451548. URL: https://doi.org/10.1063/1.451548.

[119] Ana Laura Frapiccini, Aliou Hamido, Sebastian Schröter, Dean Pyke, Francisca Mota-Furtado, Patrick F. O'Mahony, Javier Madroñero, Johannes Eiglsperger, and Bernard Piraux. "Explicit schemes for time propagating many-body wave functions." In: *Phys. Rev. A* 89 (2 2014), p. 023418. DOI: 10.1103/PhysRevA.89.023418. URL: https://link.aps.org/doi/10.1103/PhysRevA.89.023418.

[120] Fabio Novelli et al. "Witnessing the formation and relaxation of dressed quasi-particles in a strongly correlated electron system." In: *Nature Communications* 5 (Oct. 2014). DOI: 10.1038/ncomms6112. URL: http://dx.doi.org/10.1038/ncomms6112.

[121] G. De Filippis, V. Cataudella, E. A. Nowadnick, T. P. Devereaux, A. S. Mishchenko, and N. Nagaosa. "Quantum Dynamics of the Hubbard-Holstein Model in Equilibrium and Nonequilibrium: Application to Pump-Probe Phenomena." In: *Phys. Rev. Lett.* 109 (17 2012), p. 176402. DOI: 10.1103/PhysRevLett.109.176402. URL: https://link.aps.org/doi/10.1103/PhysRevLett.109.176402.

[122] G. De Filippis, V. Cataudella, A. S. Mishchenko, and N. Nagaosa. "Optical conductivity of polarons: Double phonon cloud-concept verified by diagrammatic Monte Carlo simulations." In: *Phys. Rev. B* 85 (9 2012), p. 094302. DOI: 10.1103/PhysRevB.85.094302. URL: https://link.aps.org/doi/10.1103/PhysRevB.85.094302.

[123] D. J. J. Marchand, G. De Filippis, V. Cataudella, M. Berciu, N. Nagaosa, N. V. Prokof'ev, A. S. Mishchenko, and P. C. E. Stamp. "Sharp Transition for Single Polarons in the One-Dimensional Su-Schrieffer-Heeger Model." In: *Phys. Rev. Lett.* 105 (26 2010), p. 266605. DOI: 10.1103/PhysRevLett.105.266605. URL: https://link.aps.org/doi/10.1103/PhysRevLett.105.266605.

[124] R. Bulla, N.-H. Tong, and M. Vojta. "Numerical Renormalization Group for Bosonic Systems and Application to the Sub-Ohmic Spin-Boson Model." In: *Phys. Rev. Lett.* 91 (17 2003), p. 170601. DOI: 10.1103/PhysRevLett.91.170601. URL: https://link.aps.org/doi/10.1103/PhysRevLett.91.170601.

[125] Y.-Y. Zhang, Q.-H. Chen, and K.-L. Wang. "Quantum phase transition in the sub-Ohmic spin-boson model: An extended coherent-state approach." In: *Phys. Rev. B* 81 (12 2010), p. 121105. DOI: 10.1103/PhysRevB.81.121105. URL: https://link.aps.org/doi/10.1103/PhysRevB.81.121105.

[126] L. Landau. "Zur theorie der energieüÌĹbertragung." In: *Physikalische Zeitschrift der Sowjetunion* 2 (1932), pp. 46–51.

[127] C. Zener. "Non-Adiabatic Crossing of Energy Levels." In: *Proc. R. Soc. London, Ser. A* 137.833 (1932), pp. 696–702. ISSN: 0950-1207. URL: http://rspa.royalsocietypublishing.org/content/137/833/696.

[128] P. Nalbach and M. Thorwart. "Landau-Zener Transitions in a Dissipative Environment: Numerically Exact Results." In: *Phys. Rev. Lett.* 103 (22 2009), p. 220401. DOI: 10.1103/PhysRevLett.103.220401. URL: https://link.aps.org/doi/10.1103/PhysRevLett.103.220401.

[129] S. Javanbakht, P. Nalbach, and M. Thorwart. "Dissipative Landau-Zener quantum dynamics with transversal and longitudinal noise." In: *Phys. Rev. A* 91 (5 2015), p. 052103. DOI: 10.1103/PhysRevA.91.052103. URL: https://link.aps.org/doi/10.1103/PhysRevA.91.052103.

[130] M. Thorwart, E. Paladino, and M. Grifoni. "Dynamics of the spin-boson model with a structured environment." In: *Chemical Physics* 296.2 (2004), pp. 333–344. ISSN: 0301-0104. DOI: https://doi.org/10.1016/j.chemphys.2003.10.007. URL: http://www.sciencedirect.com/science/article/pii/S0301010403005469.

[131] Peihao Huang and H Zheng. "Quantum dynamics of a qubit coupled with a structured bath." In: *Journal of Physics: Condensed Matter* 20.39 (2008), p. 395233. URL: http://stacks.iop.org/0953-8984/20/i=39/a=395233.

[132] Neill Lambert, Shahnawaz Ahmed, Mauro Cirio, and Franco Nori. "Modelling the ultra-strongly coupled spin-boson model with unphysical modes." In: *Nature Communications* 10 (2019). DOI: 10.1038/s41467-019-11656-1. URL: https://doi.org/10.1038/s41467-019-11656-1.

[133] L. M. Cangemi, V. Cataudella, M. Sassetti, and G. De Filippis. "Dissipative dynamics of a driven qubit: Interplay between nonadiabatic dynamics and noise effects from the weak to strong coupling regime." In: *Phys. Rev. B* 100 (1 2019), p. 014301. DOI: 10.1103/PhysRevB.100.014301. URL: https://link.aps.org/doi/10.1103/PhysRevB.100.014301.

[134] Matteo Carrega, Paolo Solinas, Maura Sassetti, and Ulrich Weiss. "Energy Exchange in Driven Open Quantum Systems at Strong Coupling." In: *Phys. Rev. Lett.* 116 (24 2016), p. 240403. DOI: 10.1103/PhysRevLett.116.240403. URL: https://link.aps.org/doi/10.1103/PhysRevLett.116.240403.

[135] Ettore Majorana. "Atomi orientati in campo magnetico variabile." In: *Il Nuovo Cimento (1924-1942)* 9.2 (1932), pp. 43–50. ISSN: 1827-6121. DOI: 10.1007/BF02960953. URL: https://doi.org/10.1007/BF02960953.

[136] V. Gritsev and A. Polkovnikov. "Dynamical quantum Hall effect in the parameter space." In: *Proceedings of the National Academy of Sciences* (2012). ISSN: 0027-8424. DOI: 10.1073/pnas.1116693109. URL: https://www.pnas.org/content/early/2012/04/04/1116693109.

[137] P. Roushan et al. "Observation of topological transitions in interacting quantum circuits." In: *Nature* 515 (2014), pp. 241–244. URL: https://doi.org/10.1038/nature13891.

[138] Canran Xu, Amrit Poudel, and Maxim G. Vavilov. "Nonadiabatic dynamics of a slowly driven dissipative two-level system." In: *Phys. Rev. A* 89 (5 2014), p. 052102. DOI: 10.1103/PhysRevA.89.052102. URL: https://link.aps.org/doi/10.1103/PhysRevA.89.052102.

[139] Luigi Amico, Rosario Fazio, Andreas Osterloh, and Vlatko Vedral. "Entanglement in many-body systems." In: *Rev. Mod. Phys.* 80 (2 2008), pp. 517–576. DOI: 10.1103/RevModPhys.80.517. URL: https://link.aps.org/doi/10.1103/RevModPhys.80.517.

[140] F. D. M. Haldane. "Model for a Quantum Hall Effect without Landau Levels: Condensed-Matter Realization of the "Parity Anomaly"." In: *Phys. Rev. Lett.* 61 (18 1988), pp. 2015–2018. DOI: 10.1103/PhysRevLett.61.2015. URL: https://link.aps.org/doi/10.1103/PhysRevLett.61.2015.

[141] Zhe Sun, Longwen Zhou, Gaoyang Xiao, Dario Poletti, and Jiangbin Gong. "Finite-time Landau-Zener processes and counterdiabatic driving in open systems: Beyond Born, Markov, and rotating-wave approximations." In: *Phys. Rev. A* 93 (1 2016), p. 012121. DOI: 10.1103/PhysRevA.93.012121. URL: https://link.aps.org/doi/10.1103/PhysRevA.93.012121.

[142] Eric Boyers, Mohit Pandey, David K. Campbell, Anatoli Polkovnikov, Dries Sels, and Alexander O. Sushkov. "Floquet-engineered quantum state manipulation in a noisy qubit." In: *arXiv e-prints*, arXiv:1811.09762 (2018), arXiv:1811.09762. arXiv: 1811.09762 [quant-ph].

[143] Dries Sels and Anatoli Polkovnikov. "Minimizing irreversible losses in quantum systems by local counterdiabatic driving." In: *Proceedings of the National Academy of Sciences* 114.20 (2017), E3909–E3916. ISSN: 0027-8424. DOI: 10.1073/pnas.1619826114. eprint: https://www.pnas.org/content/114/20/E3909.full.pdf. URL: https://www.pnas.org/content/114/20/E3909.

[144] Valentin Blickle and Clemens Bechinger. "Realization of a micrometre - sized stochastic heatÂăengine." In: *Nature Physics* 8 (2 2012). DOI: 10.1038/nphys2163. URL: https://doi.org/10.1038/nphys2163.

[145] T. Schmiedl and U. Seifert. "Efficiency at maximum power: An analytically solvable model for stochastic heat engines." In: *EPL (Europhysics Letters)* 81.2 (2007), p. 20003. DOI: 10.1209/0295-5075/81/20003. URL: https://doi.org/10.1209%2F0295-5075%2F81%2F20003.

[146] Viktor Holubec. "An exactly solvable model of a stochastic heat engine: optimization of power, power fluctuations and efficiency." In: *Journal of Statistical Mechanics: Theory and Experiment* 2014.5 (2014), P05022. DOI: 10.1088/1742-5468/2014/05/p05022. URL: https://doi.org/10.1088%2F1742-5468%2F2014%2F05%2Fp05022.

[147] I. A. Martínez, É. Roldán, L. Dinis, D. Petrov, J. M. R. Parrondo, and R. A. Rica. "Brownian Carnot engine." In: *Nature Physics* 12 (1 2016). DOI: 10.1038/nphys3518. URL: https://doi.org/10.1038/nphys3518.

[148] Udo Seifert. "Stochastic thermodynamics, fluctuation theorems and molecular machines." In: *Reports on Progress in Physics* 75.12 (2012), p. 126001. DOI: 10.1088/0034-4885/75/12/126001. URL: https://doi.org/10.1088%2F0034-4885%2F75%2F12%2F126001.

[149] C. Jarzynski. "Nonequilibrium Equality for Free Energy Differences." In: *Phys. Rev. Lett.* 78 (14 1997), pp. 2690–2693. DOI: 10.1103/PhysRevLett.78.2690. URL: https://link.aps.org/doi/10.1103/PhysRevLett.78.2690.

[150] Gavin E. Crooks. "Entropy production fluctuation theorem and the nonequilibrium work relation for free energy differences." In: *Phys. Rev. E* 60 (3 1999), pp. 2721–2726. DOI: 10.1103/PhysRevE.60.2721. URL: https://link.aps.org/doi/10.1103/PhysRevE.60.2721.

[151] C. Van den Broeck. "Thermodynamic Efficiency at Maximum Power." In: *Phys. Rev. Lett.* 95 (19 2005), p. 190602. DOI: 10.1103/PhysRevLett.95.190602. URL: https://link.aps.org/doi/10.1103/PhysRevLett.95.190602.

[152] Massimiliano Esposito, Ryoichi Kawai, Katja Lindenberg, and Christian Van den Broeck. "Efficiency at Maximum Power of Low-Dissipation Carnot Engines." In: *Phys. Rev. Lett.* 105 (15 2010), p. 150603. DOI: 10.1103/PhysRevLett.105.150603. URL: https://link.aps.org/doi/10.1103/PhysRevLett.105.150603.

[153] Giuliano Benenti, Giulio Casati, Keiji Saito, and RobertÂăS. Whitney. "Fundamental aspects of steady-state conversion of heat to work at the nanoscale." In: *Physics Reports* 694 (2017). Fundamental aspects of steady-state conversion of heat to work at the nanoscale, pp. 1 –124. ISSN: 0370-1573. DOI: https://doi.org/10.1016/j.physrep.2017.05.008. URL: http://www.sciencedirect.com/science/article/pii/S0370157317301540.

[154] Giuliano Benenti, Keiji Saito, and Giulio Casati. "Thermodynamic Bounds on Efficiency for Systems with Broken Time-Reversal Symmetry." In: *Phys. Rev. Lett.* 106 (23 2011), p. 230602. DOI: 10.1103/PhysRevLett.106.230602. URL: https://link.aps.org/doi/10.1103/PhysRevLett.106.230602.

[155] Patrick Pietzonka and Udo Seifert. "Universal Trade-Off between Power, Efficiency, and Constancy in Steady-State Heat Engines." In: *Phys. Rev. Lett.* 120 (19 2018), p. 190602. DOI: 10.1103/PhysRevLett.120.190602. URL: https://link.aps.org/doi/10.1103/PhysRevLett.120.190602.

[156] Jordan M. Horowitz and Todd R. Gingrich. "Thermodynamic uncertainty relations constrain non-equilibrium fluctuations." In: *Nature Physics* 16 (1 2019). DOI: 10.1038/s41567-019-0702-6. URL: https://doi.org/10.1038/s41567-019-0702-6.

[157] Andre C Barato, Raphael Chetrite, Alessandra Faggionato, and Davide Gabrielli. "Bounds on current fluctuations in periodically driven systems." In: *New Journal of Physics* 20.10 (2018),

p. 103023. DOI: 10.1088/1367-2630/aae512. URL: https://doi.org/10.1088%2F1367-2630%2Faae512.

[158] Timur Koyuk and Udo Seifert. "Operationally Accessible Bounds on Fluctuations and Entropy Production in Periodically Driven Systems." In: *Phys. Rev. Lett.* 122 (23 2019), p. 230601. DOI: 10.1103/PhysRevLett.122.230601. URL: https://link.aps.org/doi/10.1103/PhysRevLett.122.230601.

[159] M. Esposito, U. Harbola, and S. Mukamel. "Nonequilibrium fluctuations, fluctuation theorems, and counting statistics in quantum systems." In: *Rev. Mod. Phys.* 81 (4 2009), pp. 1665–1702. DOI: 10.1103/RevModPhys.81.1665. URL: https://link.aps.org/doi/10.1103/RevModPhys.81.1665.

[160] M. Campisi, P. Hänggi, and P. Talkner. "Colloquium: Quantum fluctuation relations: Foundations and applications." In: *Rev. Mod. Phys.* 83 (3 2011), pp. 771–791. DOI: 10.1103/RevModPhys.83.771. URL: https://link.aps.org/doi/10.1103/RevModPhys.83.771.

[161] Peter Talkner, Eric Lutz, and Peter Hänggi. "Fluctuation theorems: Work is not an observable." In: *Phys. Rev. E* 75 (5 2007), p. 050102. DOI: 10.1103/PhysRevE.75.050102. URL: https://link.aps.org/doi/10.1103/PhysRevE.75.050102.

[162] Augusto J. Roncaglia, Federico Cerisola, and Juan Pablo Paz. "Work Measurement as a Generalized Quantum Measurement." In: *Phys. Rev. Lett.* 113 (25 2014), p. 250601. DOI: 10.1103/PhysRevLett.113.250601. URL: https://link.aps.org/doi/10.1103/PhysRevLett.113.250601.

[163] S. Alipour, F. Benatti, F. Bakhshinezhad, M. Afsary, S. Marcantoni, and A. T. Rezakhani. "Correlations in quantum thermodynamics: Heat, work, and entropy production." In: *Scientific Reports* 6 (1 2016). DOI: 10.1038/srep35568. URL: https://doi.org/10.1038/srep35568.

[164] A. E. Allahverdyan, R. Serral Gracià, and Th. M. Nieuwenhuizen. "Work extraction in the spin-boson model." In: *Phys. Rev. E* 71 (4 2005), p. 046106. DOI: 10.1103/PhysRevE.71.046106. URL: https://link.aps.org/doi/10.1103/PhysRevE.71.046106.

[165] Eitan Geva and Ronnie Kosloff. "A quantumâĂŘmechanical heat engine operating in finite time. A model consisting of spinâĂŘ1/2 systems as the working fluid." In: *The Journal of Chemical Physics* 96.4 (1992), pp. 3054–3067. DOI: 10.1063/1.461951. eprint: https://doi.org/10.1063/1.461951. URL: https://doi.org/10.1063/1.461951.

[166] Amikam Levy, Robert Alicki, and Ronnie Kosloff. "Quantum refrigerators and the third law of thermodynamics." In: *Phys. Rev. E* 85 (6 2012), p. 061126. DOI: 10.1103/PhysRevE.85.061126. URL: https://link.aps.org/doi/10.1103/PhysRevE.85.061126.

[167] Andrea Insinga, Bjarne Andresen, and Peter Salamon. "Thermodynamical analysis of a quantum heat engine based on harmonic oscillators." In: *Phys. Rev. E* 94 (1 2016), p. 012119. DOI: 10.1103/PhysRevE.94.012119. URL: https://link.aps.org/doi/10.1103/PhysRevE.94.012119.

[168] Michele Campisi, Jukka Pekola, and Rosario Fazio. "Nonequilibrium fluctuations in quantum heat engines: theory, example, and possible solid state experiments." In: *New Journal of Physics* 17.3 (2015), p. 035012. URL: http://stacks.iop.org/1367-2630/17/i=3/a=035012.

[169] Michael Drewsen and Alberto Imparato. "Quantum duets working as autonomous thermal motors." In: *Phys. Rev. E* 100 (4 2019), p. 042138. DOI: 10.1103/PhysRevE.100.042138. URL: https://link.aps.org/doi/10.1103/PhysRevE.100.042138.

[170] Michele Campisi and Rosario Fazio. "The power of a critical heat engine." In: *Nature Communications* 7 (1 2016). DOI: 10.1038/ncomms11895. URL: https://doi.org/10.1038/ncomms11895.

[171] Armen E. Allahverdyan, Ramandeep S. Johal, and Guenter Mahler. "Work extremum principle: Structure and function of quantum heat engines." In: *Phys. Rev. E* 77 (4 2008), p. 041118. DOI: 10.1103/PhysRevE.77.041118. URL: https://link.aps.org/doi/10.1103/PhysRevE.77.041118.

[172] Jukka P. Pekola. "Towards quantum thermodynamics in electronic circuits." In: *Nature Physics* 11 (2015). DOI: 10.1038/nphys3169. URL: https://doi.org/10.1038/nphys3169.

[173] Johannes Roßnagel, Samuel T. Dawkins, Karl N. Tolazzi, Obinna Abah, Eric Lutz, Ferdinand Schmidt-Kaler, and Kilian Singer. "A single-atom heat engine." In: *Science* 352.6283 (2016), pp. 325–329. ISSN: 0036-8075. DOI: 10.1126/science.aad6320. eprint: https://science.sciencemag.org/content/352/6283/325.full.pdf. URL: https://science.sciencemag.org/content/352/6283/325.

[174] John P. S. Peterson, Tiago B. Batalhão, Marcela Herrera, Alexandre M. Souza, Roberto S. Sarthour, Ivan S. Oliveira, and Roberto M. Serra. "Experimental Characterization of a Spin Quantum Heat Engine." In: *Phys. Rev. Lett.* 123 (24 2019), p. 240601. DOI: 10.1103/PhysRevLett.123.240601. URL: https://link.aps.org/doi/10.1103/PhysRevLett.123.240601.

[175] David Newman, Florian Mintert, and Ahsan Nazir. "Performance of a quantum heat engine at strong reservoir coupling." In: *Phys. Rev. E* 95 (3 2017), p. 032139. DOI: 10.1103/PhysRevE.95.032139. URL: https://link.aps.org/doi/10.1103/PhysRevE.95.032139.

[176] M. Perarnau-Llobet, H. Wilming, A. Riera, R. Gallego, and J. Eisert. "Strong Coupling Corrections in Quantum Thermodynamics." In: *Phys. Rev. Lett.* 120 (12 2018), p. 120602. DOI: 10.1103/PhysRevLett.120.120602. URL: https://link.aps.org/doi/10.1103/PhysRevLett.120.120602.

[177] R. Katz G.; Kosloff. "Quantum Thermodynamics in Strong Coupling: Heat Transport and Refrigeration." In: *Entropy* 18 (5 2016). DOI: 10.3390/e18050186. URL: https://doi.org/10.3390/e18050186.

[178] David Gelbwaser-Klimovsky and AlÃąn Aspuru-Guzik. "Strongly Coupled Quantum Heat Machines." In: *The Journal of Physical Chemistry Letters* 6 (17 2015). DOI: doi:10.1021/acs.jpclett.5b01404. URL: https://doi.org/10.1021/acs.jpclett.5b01404.

[179] Michael Wiedmann, JÃijrgen T. Stockburger, and Joachim Ankerhold. *Out-of-equilibrium operation of a quantum heat engine: The cost of thermal coupling control*. 2019. arXiv: 1903.11368 [quant-ph].

[180] Giacomo Guarnieri, Gabriel T. Landi, Stephen R. Clark, and John Goold. "Thermodynamics of precision in quantum nonequilibrium steady states." In: *Phys. Rev. Research* 1 (3 2019), p. 033021. DOI: 10.1103/PhysRevResearch.1.033021. URL: https://link.aps.org/doi/10.1103/PhysRevResearch.1.033021.

[181] Karel Proesmans, Bart Cleuren, and Christian Van den Broeck. "Power-Efficiency-Dissipation Relations in Linear Thermodynamics." In: *Phys. Rev. Lett.* 116 (22 2016), p. 220601. DOI: 10.1103/PhysRevLett.116.220601. URL: https://link.aps.org/doi/10.1103/PhysRevLett.116.220601.

[182] Sebastian Restrepo, Javier Cerrillo, Philipp Strasberg, and Gernot Schaller. "From quantum heat engines to laser cooling: Floquet theory beyond the Born–Markov approximation." In: *New Journal of Physics* 20.5 (2018), p. 053063. DOI: 10.1088/1367-2630/aac583. URL: https://doi.org/10.1088%2F1367-2630%2Faac583.

[183] Matteo Carrega, Maura Sassetti, and Ulrich Weiss. "Optimal work-to-work conversion of a nonlinear quantum Brownian duet." In: *Phys. Rev. A* 99 (6 2019), p. 062111. DOI: 10.1103/PhysRevA.99.062111. URL: https://link.aps.org/doi/10.1103/PhysRevA.99.062111.

[184] Junjie Liu and Dvira Segal. "Thermodynamic uncertainty relation in quantum thermoelectric junctions." In: *Phys. Rev. E* 99 (6 2019), p. 062141. DOI: 10.1103/PhysRevE.99.062141. URL: https://link.aps.org/doi/10.1103/PhysRevE.99.062141.

[185] K. v. Klitzing, G. Dorda, and M. Pepper. "New Method for High-Accuracy Determination of the Fine-Structure Constant Based on Quantized Hall Resistance." In: *Phys. Rev. Lett.* 45 (6 1980), pp. 494–497. DOI: 10.1103/PhysRevLett.45.494. URL: https://link.aps.org/doi/10.1103/PhysRevLett.45.494.

[186] D. J. Thouless, M. Kohmoto, M. P. Nightingale, and M. den Nijs. "Quantized Hall Conductance in a Two-Dimensional Periodic Potential." In: *Phys. Rev. Lett.* 49 (6 1982), pp. 405–408. DOI: 10.1103/PhysRevLett.49.405. URL: https://link.aps.org/doi/10.1103/PhysRevLett.49.405.

[187] C. L. Kane and E. J. Mele. "Quantum Spin Hall Effect in Graphene." In: *Phys. Rev. Lett.* 95 (22 2005), p. 226801. DOI: 10.1103/PhysRevLett.95.226801. URL: https://link.aps.org/doi/10.1103/PhysRevLett.95.226801.

[188] C. L. Kane and E. J. Mele. "Z_2 Topological Order and the Quantum Spin Hall Effect." In: *Phys. Rev. Lett.* 95 (14 2005), p. 146802. DOI: 10.1103/PhysRevLett.95.146802. URL: https://link.aps.org/doi/10.1103/PhysRevLett.95.146802.

[189] B. Andrei Bernevig, Taylor L. Hughes, and Shou-Cheng Zhang. "Quantum Spin Hall Effect and Topological Phase Transition in HgTe Quantum Wells." In: *Science* 314.5806 (2006), pp. 1757–1761. ISSN: 0036-8075. DOI: 10.1126/science.1133734. eprint: https://science.sciencemag.org/content/314/5806/1757.full.pdf. URL: https://science.sciencemag.org/content/314/5806/1757.

[190] J. E. Moore and L. Balents. "Topological invariants of time-reversal-invariant band structures." In: *Phys. Rev. B* 75 (12 2007), p. 121306. DOI: 10.1103/PhysRevB.75.121306. URL: https://link.aps.org/doi/10.1103/PhysRevB.75.121306.

[191] Liang Fu and C. L. Kane. "Time reversal polarization and a Z_2 adiabatic spin pump." In: *Phys. Rev. B* 74 (19 2006), p. 195312. DOI: 10.1103/PhysRevB.74.195312. URL: https://link.aps.org/doi/10.1103/PhysRevB.74.195312.

[192] Alexander Altland and Martin R. Zirnbauer. "Nonstandard symmetry classes in mesoscopic normal-superconducting hybrid structures." In: *Phys. Rev. B* 55 (2 1997), pp. 1142–1161. DOI: 10.1103/PhysRevB.55.1142. URL: https://link.aps.org/doi/10.1103/PhysRevB.55.1142.

[193] Andreas P. Schnyder, Shinsei Ryu, Akira Furusaki, and Andreas W. W. Ludwig. "Classification of topological insulators and superconductors in three spatial dimensions." In: *Phys. Rev. B* 78 (19 2008), p. 195125. DOI: 10.1103/PhysRevB.78.195125. URL: https://link.aps.org/doi/10.1103/PhysRevB.78.195125.

[194] Alexei Kitaev. "Periodic table for topological insulators and superconductors." In: *AIP Conference Proceedings* 1134 (1 2009). DOI: doi:10.1063/1.3149495. URL: https://aip.scitation.org/doi/abs/10.1063/1.3149495.

[195] Jorrit Kruthoff, Jan de Boer, Jasper van Wezel, Charles L. Kane, and Robert-Jan Slager. "Topological Classification of Crystalline Insulators through Band Structure Combinatorics." In: *Phys. Rev. X* 7 (4 2017), p. 041069. DOI: 10.1103/PhysRevX.7.041069. URL: https://link.aps.org/doi/10.1103/PhysRevX.7.041069.

[196] Liang Fu, C. L. Kane, and E. J. Mele. "Topological Insulators in Three Dimensions." In: *Phys. Rev. Lett.* 98 (10 2007), p. 106803. DOI: 10.1103/PhysRevLett.98.106803. URL: https://link.aps.org/doi/10.1103/PhysRevLett.98.106803.

[197] Markus König, Steffen Wiedmann, Christoph Brüne, Andreas Roth, Hartmut Buhmann, Laurens W. Molenkamp, Xiao-Liang Qi, and Shou-Cheng Zhang. "Quantum Spin Hall Insulator State in HgTe Quantum Wells." In: *Science* 318.5851 (2007), pp. 766–770. ISSN: 0036-8075. DOI: 10.1126/science.1148047. eprint: https://science.sciencemag.org/content/318/5851/766.full.pdf. URL: https://science.sciencemag.org/content/318/5851/766.

[198] D. Hsieh, D. Qian, L. Wray, Y. Xia, Y. S. Hor, R. J. Cava, and M. Z. Hasan. "A topological Dirac insulator in a quantum spin Hall phase." In: *Nature* 452 (2008). DOI: 10.1038/nature06843. URL: https://doi.org/10.1038/nature06843.

[199] Frank Schindler, Ashley M. Cook, Maia G. Vergniory, Zhijun Wang, Stuart S. P. Parkin, B. Andrei Bernevig, and Titus Neupert. "Higher-order topological insulators." In: *Science Advances* 4.6 (2018). DOI: 10.1126/sciadv.aat0346. eprint: https://advances.sciencemag.org/content/4/6/eaat0346.full.pdf. URL: https://advances.sciencemag.org/content/4/6/eaat0346.

[200] D. C. Tsui, H. L. Stormer, and A. C. Gossard. "Two-Dimensional Magnetotransport in the Extreme Quantum Limit." In: *Phys. Rev. Lett.* 48 (22 1982), pp. 1559–1562. DOI: 10.1103/PhysRevLett.48.1559. URL: https://link.aps.org/doi/10.1103/PhysRevLett.48.1559.

[201] R. B. Laughlin. "Anomalous Quantum Hall Effect: An Incompressible Quantum Fluid with Fractionally Charged Excitations." In: *Phys. Rev. Lett.* 50 (18 1983), pp. 1395–1398. DOI: 10.1103/PhysRevLett.50.1395. URL: https://link.aps.org/doi/10.1103/PhysRevLett.50.1395.

[202] V. Gurarie. "Single-particle Green's functions and interacting topological insulators." In: *Phys. Rev. B* 83 (8 2011), p. 085426. DOI: 10.1103/PhysRevB.83.085426. URL: https://link.aps.org/doi/10.1103/PhysRevB.83.085426.

[203] Andrew M. Essin and Victor Gurarie. "Bulk-boundary correspondence of topological insulators from their respective Green's functions." In: *Phys. Rev. B* 84 (12 2011), p. 125132. DOI: 10.1103/PhysRevB.84.125132. URL: https://link.aps.org/doi/10.1103/PhysRevB.84.125132.

[204] Zhong Wang and Shou-Cheng Zhang. "Simplified Topological Invariants for Interacting Insulators." In: *Phys. Rev. X* 2 (3 2012), p. 031008. DOI: 10.1103/PhysRevX.2.031008. URL: https://link.aps.org/doi/10.1103/PhysRevX.2.031008.

[205] Zhong Wang, Xiao-Liang Qi, and Shou-Cheng Zhang. "Topological invariants for interacting topological insulators with inversion symmetry." In: *Phys. Rev. B* 85 (16 2012), p. 165126. DOI: 10.1103/PhysRevB.85.165126. URL: https://link.aps.org/doi/10.1103/PhysRevB.85.165126.

[206] Giuseppe Morandi. *Quantum Hall effect. Topological problems in condensed-matter physics*. Bibliopolis, 1988. ISBN: 88-7088-210-1.

[207] Eliahu Cohen, Hugo Larocque, FrÃľdÃľric Bouchard, Farshad Nejadsattari, Yuval Gefen, and Ebrahim Karimi. "Geometric phase from AharonovâĂŞBohm to PancharatnamâĂŞBerry andÂăbeyond." In: *Nature Reviews Physics* 1 (2019). DOI: 10.1038/s42254-019-0071-1. URL: https://doi.org/10.1038/s42254-019-0071-1.

[208] Grigory E. Volovik. *The Universe in a Helium Droplet*. Oxford, 2009. ISBN: 9780199564842.

[209] L. M. Cangemi, A. S. Mishchenko, N. Nagaosa, V. Cataudella, and G. De Filippis. "Topological Quantum Transition Driven by Charge-Phonon Coupling in the Haldane Chern Insulator." In: *Phys. Rev. Lett.* 123 (4 2019), p. 046401. DOI: 10.1103/PhysRevLett.123.046401. URL: https://link.aps.org/doi/10.1103/PhysRevLett.123.046401.

[210] Christopher N. Varney, Kai Sun, Marcos Rigol, and Victor Galitski. "Interaction effects and quantum phase transitions in topological insulators." In: *Phys. Rev. B* 82 (11 2010), p. 115125. DOI: 10.1103/PhysRevB.82.115125. URL: https://link.aps.org/doi/10.1103/PhysRevB.82.115125.

[211] M Hohenadler and F F Assaad. "Correlation effects in two-dimensional topological insulators." In: *Journal of Physics: Condensed Matter* 25.14 (2013), p. 143201. DOI: 10.1088/0953-8984/25/14/143201. URL: https://doi.org/10.1088%2F0953-8984%2F25%2F14%2F143201.

[212] Maria Daghofer and Martin Hohenadler. "Phases of correlated spinless fermions on the honeycomb lattice." In: *Phys. Rev. B* 89 (3 2014), p. 035103. DOI: 10.1103/PhysRevB.89.035103. URL: https://link.aps.org/doi/10.1103/PhysRevB.89.035103.

[213] Sylvain Capponi and Andreas M. Läuchli. "Phase diagram of interacting spinless fermions on the honeycomb lattice: A comprehensive exact diagonalization study." In: *Phys. Rev. B* 92 (8 2015), p. 085146. DOI: 10.1103/PhysRevB.92.085146. URL: https://link.aps.org/doi/10.1103/PhysRevB.92.085146.

[214] Bohm-Jung Yang, Eun-Gook Moon, Hiroki Isobe, and Naoto Nagaosa. "Quantum criticality of topological phase transitions in three-dimensional interacting electronic systems." In: *Nature Physics* 10 (2014), pp. 774–778. DOI: 10.1038/nphys3060. URL: https://doi.org/10.1038/nphys3060.

[215] Igor S. Tupitsyn and Nikolay V. Prokof'ev. "Phase diagram topology of the Haldane-Hubbard-Coulomb model." In: *Phys. Rev. B* 99 (12 2019), p. 121113. DOI: 10.1103/PhysRevB.99.121113. URL: https://link.aps.org/doi/10.1103/PhysRevB.99.121113.

[216] Igor S. Tupitsyn, Andrey S. Mishchenko, Naoto Nagaosa, and Nikolay Prokof'ev. "Coulomb and electron-phonon interactions in metals." In: *Phys. Rev. B* 94 (15 2016), p. 155145. DOI: 10.1103/PhysRevB.94.155145. URL: https://link.aps.org/doi/10.1103/PhysRevB.94.155145.

[217] Mirko M. Möller, George A. Sawatzky, Marcel Franz, and Mona Berciu. "Type-II Dirac semimetal stabilized by electron-phonon coupling." In: *Nature Communications* 8 (2017). DOI: 10.1038/s41467-017-02442-y. URL: https://doi.org/10.1038/s41467-017-02442-y.

[218] Chuang Chen, Xiao Yan Xu, Zi Yang Meng, and Martin Hohenadler. "Charge-Density-Wave Transitions of Dirac Fermions Coupled to Phonons." In: *Phys. Rev. Lett.* 122 (7 2019), p. 077601. DOI: 10.1103/PhysRevLett.122.077601. URL: https://link.aps.org/doi/10.1103/PhysRevLett.122.077601.

[219] Andrea Damascelli. "Probing the Electronic Structure of Complex Systems by ARPES." In: *Physica Scripta* T109 (2004), p. 61. DOI: 10.1238/physica.topical.109a00061. URL: https://doi.org/10.1238%2Fphysica.topical.109a00061.

[220] Gerald D. Mahan. *Many-Particle Physics*. Springer US, 2000. ISBN: 978-0-306-46338-9.

[221] John Dirk Walecka Alexander L. Fetter. *Quantum theory of many-particle systems*. Mineola, N.Y. : Dover Publications, 2003. ISBN: 0486428273.

[222] L. M. Cangemi, A. S. Mishchenko, N. Nagaosa, V. Cataudella, and G. De Filippis. *Topological phase transition in quantum spin Hall insulator in the presence of charge lattice coupling*. 2019. arXiv: 1905.01383 [cond-mat.str-el].

[223] G. De Filippis, V. Cataudella, R. Citro, C. A. Perroni, A. S. Mishchenko, and N. Nagaosa. "Interplay between charge-lattice interaction and strong electron correlations in cuprates: Phonon anomaly and spectral kinks." In: *EPL (Europhysics Letters)* 91.4 (2010), p. 47007. DOI: 10.1209/0295-5075/91/47007. URL: https://doi.org/10.1209%2F0295-5075%2F91%2F47007.

[224] M V Berry. "Transitionless quantum driving." In: *Journal of Physics A: Mathematical and Theoretical* 42.36 (2009), p. 365303. URL: http://stacks.iop.org/1751-8121/42/i=36/a=365303.